UNIVERSIDADE FEDERAL DO CEARÁ
CENTRO DE CIÊNCIAS
DEPARTAMENTO DE FÍSICA
PROGRAMA DE PÓS-GRADUAÇÃO EM FÍSICA

FRANCISCO RONAN VIANA ARAÚJO

THEORETICAL PROPOSALS OF GRAPHENE-BASED ELECTRONIC DEVICES

FORTALEZA – CE
2021

FRANCISCO RONAN VIANA ARAÚJO

THEORETICAL PROPOSALS OF GRAPHENE-BASED ELECTRONIC DEVICES

Tese apresentada ao Programa de Pós-Graduação em Física da Universidade Federal do Ceará, como requisito parcial para a obtenção do título de Doutor em Física. Área de Concentração: Física da Matéria Condensada.

Orientador: João Milton Pereira Junior.
Coorientador: Diego Rabelo da Costa.

FORTALEZA – CE
2021

Dados Internacionais de Catalogação na Publicação
Universidade Federal do Ceará
Biblioteca Universitária
Gerada automaticamente pelo módulo Catalog, mediante os dados fornecidos pelo(a) autor(a)

A689t Araújo, Francisco Ronan Viana.
Theoretical proposals of graphene-based electronic devices / Francisco Ronan Viana Araújo. – 2021.
127 f. : il. color.

Tese (doutorado) – Universidade Federal do Ceará, Centro de Ciências, Programa de Pós-Graduação em Física , Fortaleza, 2021.
Orientação: Prof. Dr. João Milton Pereira Junior.
Coorientação: Prof. Dr. Diego Rabelo da Costa.

1. graphene. 2. electronic device. 3. p-n junction. 4. Y-junction. 5. quantum ring. I. Título.
CDD 530

FRANCISCO RONAN VIANA ARAÚJO

THEORETICAL PROPOSALS OF GRAPHENE-BASED ELECTRONIC DEVICES

Tese apresentada ao Programa de Pós-Graduação em Física da Universidade Federal do Ceará, como requisito parcial para a obtenção do título de Doutor em Física. Área de Concentração: Física da Matéria Condensada.

Aprovada em 09/09/2021.

BANCA EXAMINADORA:

Prof. Dr. João Milton Pereira Junior - Orientador
Universidade Federal do Ceará

Prof. Dr. Diego Rabelo da Costa - Coorientador
Universidade Federal do Ceará

Prof. Dr. Andrey Chaves
Universidade Federal do Ceará

Prof. Dr. Alexandro das Chagas de Sousa Nascimento
Instituto Federal do Piauí

Prof. Dr. André Jorge Carvalho Chaves
Instituto Tecnológico de Aeronáutica

Prof. Dr. Luan Vieira de Castro
Universidade Federal do Ceará

Ao meu filho, Ravi. À minha mãe, Rosângela.
À minha esposa, Thaís.

AGRADECIMENTOS

Encerra-se aqui a mais significativa etapa de minha formação acadêmica. Assim, gostaria de agradecer profundamente ao Milton Pereira, meu orientador, pela orientação paciente, consistente e segura durante meu mestrado e meu doutorado. Ao Diego Rabelo, meu coorientador, pelos valiosos ensinamentos, pelas produtivas conversas e, antes de qualquer coisa, pela amizade. À minha família, especialmente à Thaís Viana, minha esposa, e à Rosângela Viana, minha mãe, pelo amor e pelo apoio incondicional. Ao Alexandro Nascimento e ao Itamar Vieira, meus amigos e ex-professores, pelas importantes discussões realizadas nos últimos anos sobre Física Geral e Física da Matéria Condensada. Ao Andrey Chaves, ao André Chaves e ao Luan Vieira, pelas correções e melhorias sugeridas para a versão final desta Tese. Ao Gildário Dias, por ter despertado em mim o interesse pela Nanotecnologia. Ao Departamento de Física da Universidade Federal do Ceará (DF/UFC), por fornecer ótimas condições de estudo/pesquisa para os estudantes. Ao Instituto Federal do Piauí (IFPI), por incentivar e apoiar iniciativas de formação acadêmica objetivando melhorar o serviço público prestado à sociedade. Ao Conselho Nacional de Desenvolvimento Científico e Tecnológico (CNPq), por fomentar a pesquisa científica e tecnológica e incentivar a formação de pesquisadores brasileiros. Por fim, aos professores que fizeram (e também aos que não fizeram) parte de minha formação acadêmica.

"Se um macaco acumulasse mais bananas do que pudesse comer, enquanto a maioria dos outros macacos morresse de fome, os cientistas estudariam aquele macaco para descobrir o que diabos estaria acontecendo com ele. Quando os humanos fazem isso, nós os colocamos na capa da Forbes."

Emir Simão Sader

ABSTRACT

Graphene has been extensively investigated after its isolation in 2004 by A. K. Geim and K. S. Novoselov. Due to its remarkable electronic and transport properties, it has become a promising candidate to replace silicon in the production of field-effect transistors (heart of the electronics industry). However, turning off the current via gate potentials in graphene-based electronic devices can be a challenge due to Klein tunneling. In recent years, there has been an expressive search for theoretical and experimental proposals capable of modulating the current, avoiding the limitation imposed by Klein tunneling. In this sense, three electronic devices based on graphene nanoribbons were investigated in this Thesis, namely: (i) graphene p-n junction that acts as a Veselago lens, (ii) three-terminal ballistic junction of graphene (graphene Y-junction), and (iii) graphene quantum ring in the presence of a perpendicular magnetic field. Numerical simulations of quantum transport using a tight-binding model were performed in (i) and (ii). In (i), it was demonstrated that the application of an in-plane electric field or a perpendicular magnetic field changes the position of the output focus of the Veselago lens, reducing the conductance between the input and output terminals. In (ii), it was found that a gate potential applied to one of the graphene Y-junction terminals can properly modulate the current between the input terminal and the two output terminals. Finally, in (iii), a numerical approximation using the tight-binding model was compared to an analytical approach using the continuum model in order to show that the persistent current can be tuned through a gate potential applied to one of the graphene quantum ring arms. The electronic devices presented in this Thesis can benefit from the high mobility of charge carriers in graphene and represent viable theoretical proposals for the development of low-power field-effect transistors.

Keywords: graphene; electronic device; p-n junction; Y-junction; quantum ring.

RESUMO

O grafeno tem sido extensivamente investigado após seu isolamento em 2004 por A. K. Geim e K. S. Novoselov. Devido às suas notáveis propriedades eletrônicas e de transporte, tornou-se um candidato promissor para substituir o silício na produção de transistores de efeito de campo (coração da indústria eletrônica). No entanto, desligar a corrente via potenciais de porta em dispositivos eletrônicos baseados em grafeno pode ser um desafio devido ao tunelamento de Klein. Nos últimos anos, tem havido uma busca expressiva por propostas teóricas e experimentais capazes de modular a corrente, evitando a limitação imposta pelo tunelamento de Klein. Nesse sentido, três dispositivos eletrônicos baseados em nanofitas de grafeno foram investigados nesta Tese, a saber: (i) junção p-n de grafeno que atua como uma lente de Veselago, (ii) junção balística de três terminais de grafeno (junção Y de grafeno), e (iii) anel quântico de grafeno na presença de um campo magnético perpendicular. Simulações numéricas de transporte quântico usando um modelo *tight-binding* foram realizadas em (i) e (ii). Em (i), foi demonstrado que a aplicação de um campo elétrico no plano ou de um campo magnético perpendicular altera a posição do foco de saída da lente de Veselago, reduzindo a condutância entre os terminais de entrada e de saída. Em (ii), foi encontrado que um potencial de porta aplicado a um dos terminais da junção Y de grafeno pode modular adequadamente a corrente entre o terminal de entrada e os dois terminais de saída. Por fim, em (iii), uma aproximação numérica usando o modelo *tight-binding* foi comparada a uma abordagem analítica usando o modelo contínuo, a fim de mostrar que a corrente persistente pode ser sintonizada através de um potencial de porta aplicado a um dos braços do anel quântico de grafeno. Os dispositivos eletrônicos apresentados nesta Tese podem se beneficiar da alta mobilidade dos portadores de carga no grafeno e representam propostas teóricas viáveis para o desenvolvimento de transistores de efeito de campo de baixa potência.

Palavras-chave: grafeno; dispositivo eletrônico; junção p-n; junção Y; anel quântico.

LIST OF FIGURES

CONTENTS

1 INTRODUCTION

New and unusual biological, physical and chemical properties presented by nanostructured materials are important scientific discoveries that point to possible advances in science and technology in the near future. The area that investigates these new materials has been given the name of nanoscience or, more commonly, nanotechnology. However, the difference between nanoscience and nanotechnology is equally comparable to the difference between science and technology. Around the world, both academic and applied research institutes are creating new paths for research in nanotechnology. The main topics currently investigated are materials science, electronics, optoelectronics, and biomedical science[4].

Actually, the material most used in the production of field-effect transistors (the heart of the electronics industry) is silicon. Despite its great efficiency and versatility, its use in electronics should reach the limit in less than a decade due to problems that arise when the size scale is in the order of magnitude of the nanometer[5]. Thus, researchers and scientists are looking for other ways to develop field-effect transistors or similar, with even better performance at reduced costs. Some suggest the replacement of silicon by nanostructured materials, from graphene and phosphorene to molybdenum disulfide (MoS_2) and tungsten diselenide (WSe_2)[6].

Graphene consists of a layer of carbon atoms arranged in a honeycomb crystal structure. It is considered an essentially two-dimensional material as it is only one carbon atom thick. A few decades ago, L. D. Landau and R. E. Peierls argued that strictly two-dimensional crystals were thermodynamically unstable and should not exist[7]. In 2004, however, Russian physicists A. K. Geim and K. S. Novoselov, both from the University of Manchester (UK), and others, published an article reporting the isolation of graphene and also a series of results on some of its physical properties[8]. In addition, in 2010, A. K. Geim and K. S. Novoselov received the Nobel Prize in Physics for their "groundbreaking experiments regarding the two-dimensional material graphene". The technique used by

A. K. Geim and K. S. Novoselov to isolate graphene is quite simple. They extracted some graphene sheets from the graphite by a technique known as micromechanical cleavage[9, 10]. Graphite consists of stacked graphene sheets. Through this technique, the graphene samples produced are so good that phenomena such as ballistic electronic transport and the quantum Hall effect can be easily observed[11]. For application purposes, the most suitable technique in most cases for obtaining large samples of graphene is chemical vapor deposition (CVD)[12].

1.1 Graphene

Graphene consists of sp^2 hybridized carbon atoms chemically bonded through covalent bonds, where an s atomic orbital hybridizes with two other p atomic orbitals (p_x and p_y) to form three planar atomic orbitals with angles of 120° each other. The unhybridized p_z atomic orbital is perpendicular to this plane and is of particular importance in describing the electronic properties of graphene. The stacking of graphene sheets interacting through van der Waals forces gives rise to graphite. Other allotropic forms of carbon, obtained from graphene, are fullerenes[13], carbon nanotubes[14], and others[15, 16].

1.1.1 *Crystal structure and reciprocal lattice*

Fig. 1.1(a) schematically illustrates the crystal structure of graphene. Such structure is not a Bravais lattice, however, it can be represented by a triangular Bravais lattice with two carbon atoms at the base, formed by the superposition of two triangular Bravais sublattices, called A and B sublattices. In graphene, the distance between adjacent carbon atoms is $a = 0.142$ nm[1] and the primitive translation vectors of the real lattice can be defined as $\mathbf{a}_1 = (3a/2, \sqrt{3}a/2)$ and $\mathbf{a}_2 = (3a/2, -\sqrt{3}a/2)$. The primitive translation vectors of the reciprocal lattice are thus $\mathbf{b}_1 = [2\pi/(3a), 2\pi\sqrt{3}/(3a)]$ and $\mathbf{b}_2 = [2\pi/(3a), -2\pi\sqrt{3}/(3a)]$. In Fig. 1.1(a), the unit cell of the real lattice is highlighted in grey. Likewise, in Fig. 1.1(b), the first Brillouin zone is highlighted in yellow. A detailed description of the crystal structure, reciprocal lattice, and elementary electronic properties of graphene is performed in Chapter 2.

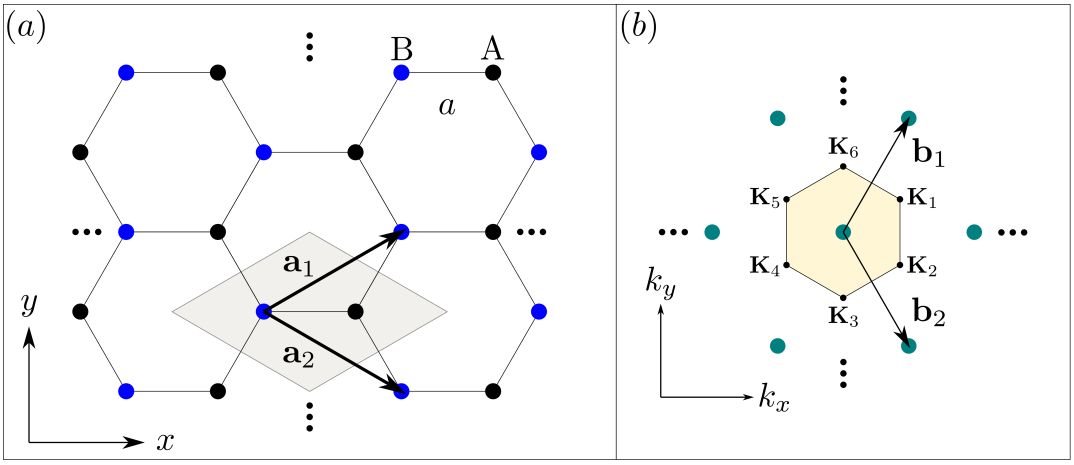

Figure 1.1: Schematic illustration of the (a) crystal structure and (b) reciprocal lattice of graphene. Panel (a) shows that the crystal structure of graphene can be represented by a triangular Bravais lattice with two carbon atoms at the base. The unit cell is highlighted in grey in panel (a), and the first Brillouin zone is highlighted in yellow in panel (b).

1.1.2 *Elementary electronic properties*

The tight-binding model provides a categorical description of the elementary electronic properties of graphene. The Hamiltonian considering that electrons can only hop to the first and second neighbors of a carbon atom has the form (taking $\hbar = 1$):

$$\mathcal{H} = -t \sum_{\langle i,j\rangle,\sigma} (a^{\dagger}_{\sigma,i} b_{\sigma,j} + \text{H.c.}) - t' \sum_{\langle\langle i,j\rangle\rangle,\sigma} (a^{\dagger}_{\sigma,i} a_{\sigma,j} + b^{\dagger}_{\sigma,i} b_{\sigma,j} + \text{H.c.}), \tag{1.1}$$

where $t = 2.8$ eV ($t' = 0.1$ eV) is the hopping parameter between carbon atoms that are first (second) neighbors[1] and $a_{\sigma,i}$ ($a^{\dagger}_{\sigma,i}$) is an operator that annihilates (creates) an electron with spin $\sigma = \uparrow$ or $\downarrow$ at site $\mathbf{R}_i$ of sublattice A, the equivalent being valid for $b_{\sigma,j}$ ($b^{\dagger}_{\sigma,j}$). H.c. means Hermitian conjugation. The energy bands, in turn, have the form:

$$\begin{aligned} E_{\pm}(\mathbf{k}) = st\sqrt{3 + 2\cos(\sqrt{3}k_y a) + 4\cos(\sqrt{3}k_y a/2)\cos(3k_x a/2)} - \\ -t'[2\cos(\sqrt{3}k_y a) + 4\cos(\sqrt{3}k_y a/2)\cos(3k_x a/2)], \end{aligned} \tag{1.2}$$

where $s = \text{sgn}[E_{\pm}(\mathbf{k})]$, that is, $s = -1$ for $E_{\pm}(\mathbf{k}) < 0$, $s = 0$ for $E_{\pm}(\mathbf{k}) = 0$, and $s = +1$ for $E_{\pm}(\mathbf{k}) > 0$. Therefore, $s = -1$ refers to the valence band and $s = +1$ refers to the conduction band. The energy bands are symmetric with respect to the zero energy plane for $t' = 0$, as shown in Fig. 1.2(a). On the other hand, for $t' \neq 0$, the energy bands become asymmetric, resulting in electron-hole symmetry breaking. There are six points where the energy bands coincide, and of these six points only two (the $\mathbf{K}$ and $\mathbf{K}'$ points, known as Dirac points) are not equivalent [see Fig. 1.2(a)].

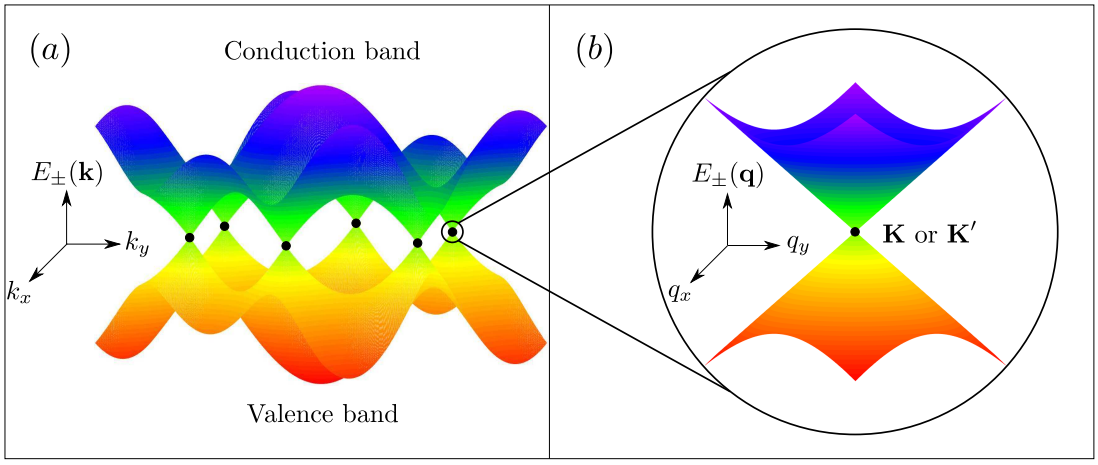

Figure 1.2: (a) energy bands for $t = 2.8$ eV and $t' = 0$. There are six points where the valence and conduction bands coincide, and of these six points only two are not equivalent. (b) conical aspect of the energy bands in the vicinity of Dirac points.

1.1.3 *Low-energy limit and continuum model*

It is noted by Eq. (1.2) and Fig. 1.2(b) that in the vicinity of each of the Dirac points there is a linearity relation between $E_{\pm}(\mathbf{k})$ and $\mathbf{k}$. This is explicit when the first-order Taylor series around $\mathbf{K}$ (or $\mathbf{K}'$) of $f(\mathbf{k}) = 2\cos(\sqrt{3}k_y a) + 4\cos(\sqrt{3}k_y a/2)\cos(3k_x a/2)$ in Eq. (1.2) is taken, resulting in $E_{\pm}(\mathbf{q}) = sv_F|\mathbf{q}|$, where $\mathbf{q} = \mathbf{k} - \mathbf{K}$, with $|\mathbf{q}| << |\mathbf{K}|$, and $v_F = 3at/2$ is the Fermi velocity of the charge carriers in graphene with low energies. For $t = 2.8$ eV and $a = 0.142$ nm, $v_F \approx c/300$ is obtained, where c is the speed of light in vacuum. Therefore, charge carriers in graphene do not have relativistic Fermi velocities. The valence band, known as the lower Dirac cone, include the occupied eigenstates, and the conduction band, known as the upper Dirac cone, include the unoccupied eigenstates. In this sense, it is convenient to use the continuum model to write the Hamiltonian (1.1) as:

$$-iv_F\sigma \cdot \nabla\Psi(\mathbf{r}) = E\Psi(\mathbf{r}), \quad \text{for} \quad \mathbf{K}, \tag{1.3}$$

$$-iv_F\sigma^* \cdot \nabla\Psi(\mathbf{r}) = E\Psi(\mathbf{r}), \quad \text{for} \quad \mathbf{K}', \tag{1.4}$$

where $\sigma = (\sigma_x, \sigma_y)$ is the Pauli vector. The respective eigenstates, in turn, in momentum space, are:

$$\Psi_{\pm,\mathbf{K}}(\mathbf{q}) = \frac{1}{\sqrt{2}} \begin{pmatrix} e^{-i\theta_\mathbf{q}/2} \\ \pm e^{+i\theta_\mathbf{q}/2} \end{pmatrix}, \tag{1.5}$$

$$\Psi_{\pm,\mathbf{K}'}(\mathbf{q}) = \frac{1}{\sqrt{2}} \begin{pmatrix} e^{+i\theta_\mathbf{q}/2} \\ \pm e^{-i\theta_\mathbf{q}/2} \end{pmatrix}, \tag{1.6}$$

where $\theta_\mathbf{q} = \arctan(q_x/q_y)$ is the angle in momentum space. Thus, there is a mapping between the continuum model that describes the charge carriers in graphene, coming from the tight-binding model, and the Dirac equation that describes relativistic massless fermions with spin 1/2. This mapping allows an analogy between the behavior of massless neutrinos and charge carriers in graphene. An example of this analogy is discussed in Ref. [17]. The authors evaluated the dispersion relation of relativistic massless fermions with spin 1/2, described by the Dirac equation, and relativistic bosons with spin 0, described by the Klein-Gordon equation, moving in two dimensions and in the presence of a one-dimensional periodic potential.

1.1.4 *Klein tunneling*

In 1929, O. Klein obtained an interesting result when analyzing the transmission of an electron through a potential barrier using the Dirac equation[18]. Unlike what happens when the Schrödinger equation is used, it was verified that the eigenstates of the electrons were not dampened by the potential barrier under certain circumstances. As seen, charge carriers in graphene can be described by the Dirac equation. Thus, several works on the Klein paradox in graphene, both theoretical[19, 20] and experimental[21], were reported.

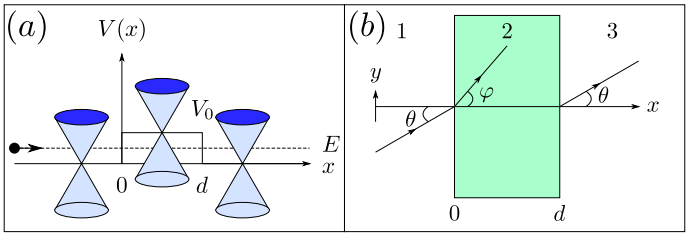

Figure 1.3: (a) incidence of an electron with energy E through a potential barrier with height V_0. (b) representation of the angles of incidence and refraction.

Considering the incidence of an electron with energy E through a potential barrier defined as $V(x) = 0$ for $x \leq 0$ and $x \geq d$, and $V(x) = V_0$ for $0 < x < d$ [schematically illustrated in Fig. 1.3(a)], the eigenstates in regions 1, 2 and 3 of Fig. 1.3(b) are, respectively:

$$\Psi_1(\mathbf{r}) = \frac{1}{\sqrt{2}} \begin{pmatrix} 1 \\ se^{i\theta} \end{pmatrix} e^{i(q_x x + q_y y)} + \frac{r}{\sqrt{2}} \begin{pmatrix} 1 \\ se^{i(\pi-\theta)} \end{pmatrix} e^{i(-q_x x + q_y y)}, \tag{1.7}$$

$$\Psi_2(\mathbf{r}) = \frac{a}{\sqrt{2}} \begin{pmatrix} 1 \\ s'e^{i\varphi} \end{pmatrix} e^{i(\kappa_x x + q_y y)} + \frac{b}{\sqrt{2}} \begin{pmatrix} 1 \\ s'e^{i(\pi-\varphi)} \end{pmatrix} e^{i(-\kappa_x x + q_y y)}, \tag{1.8}$$

$$\Psi_3(\mathbf{r}) = \frac{t}{\sqrt{2}} \begin{pmatrix} 1 \\ se^{i\theta} \end{pmatrix} e^{i(q_x x + q_y y)}, \tag{1.9}$$

where θ is the angle of incidence, φ is the angle of refraction, $s = \mathrm{sgn}(E)$, $s' = \mathrm{sgn}(E - V_0)$, $q_{x(y)}$ is the $x(y)$-component of the wavevector in regions 1 and 3, and $\kappa_{x(y)}$ is the $x(y)$-component of the wavevector in region 2. The coefficients a, b, r and t are determined by the boundary conditions at the interfaces that separate regions 1|2 and 2|3:

$$\Psi_1(0, y) = \Psi_2(0, y), \tag{1.10}$$

$$\Psi_2(d, y) = \Psi_3(d, y), \tag{1.11}$$

for the present purpose, it is sufficient to determine only the coefficient t, so that:

$$tt^* = T(\theta) = \frac{\cos^2\varphi \cos^2\theta}{\cos^2(\kappa_x d)\cos^2\theta\cos^2\varphi + \sin^2(\kappa_x d)(1 - ss'\sin\theta\sin\varphi)^2}, \tag{1.12}$$

for $\kappa_x d = N\pi$, with N an integer, the potential barrier becomes transparent, independent of θ. Furthermore, the potential barrier is always transparent for $\theta = 0$. This effect is a unique feature of massless Dirac fermions and is directly related to the Klein paradox of quantum electrodynamics. The dependence of transmission probability on the angle of incidence for $d = 110$ nm [$d = 50$ nm] is shown in Fig. 1.4(a) [1.4(b)]. Dashed blue (solid red) line refers to $V_0 = 200$ meV ($V_0 = 285$ meV). $E = 80$ meV and $\lambda_F = 50$ nm was taken. Additionally, in the limit where $|V_0| >> |E|$, the angle of refraction approaches zero, resulting in:

$$T(\theta) = \frac{\cos^2\theta}{1 - \cos^2(\kappa_x d)\sin^2\theta}. \tag{1.13}$$

It is important to mention that after tunneling the electron through the potential barrier, its eigenstate acquires a phase $\phi = V_0 d/(\hbar v_F)$, which can be used in the modeling of electronic devices based on interference phenomena[22].

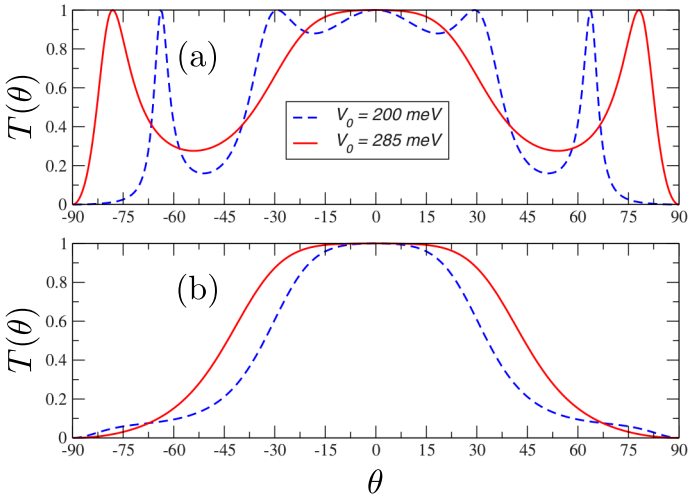

Figure 1.4: Dependence of transmission probability on the angle of incidence for (a) $d = 110$ nm and (b) $d = 50$ nm. Dashed blue (solid red) line refers to $V_0 = 200$ meV ($V_0 = 285$ meV). $E = 80$ meV and $\lambda_F = 50$ nm was taken. Adapted from Ref. [1].

1.1.5 *Veselago lens, negative refraction and p-n junction*

Negative refraction is an interesting optical effect that allows the development of perfect optical lenses that can focus light beams to extremely fine points[23]. In 1968, V. G. Veselago showed that, under conditions where the electric and magnetic responses are negative, the group and phase velocities point in opposite directions[24], which is exactly what happens with the electrons that occupy the valence band of graphene[2]. Accordingly, in 2007, V. V. Cheianov *et al.* examined the negative refraction at a graphene p-n junction[2], which can be made by two metal plates almost touching above a graphene sheet, one polarizing the sample to a positive voltage (n-type), the other polarizing the sample to a negative voltage (p-type). In general, p-n junctions are basic electronic devices and are usually produced with semiconductor materials. Due to the peculiar band structure of graphene, considered a zero gap semiconductor[1], an infinitesimal perturbation changes the Fermi level to the upper or lower band, making it a p-type conductor if the Fermi level is lowered to the valence band, or a n-type conductor if the Fermi level is raised to the conduction band. The change in Fermi level can be done through a gate potential[25], as is schematically illustrated in Fig. 1.5(a).

In the context of geometric optics, when a light beam hits an interface that separates two media with refractive indices n_1 and n_2, the Snell-Descartes law is valid, $n_1 \sin\theta_1 = n_2 \sin\theta_2$, where θ_1 (θ_2) is the angle of incidence (refraction). On the other hand,

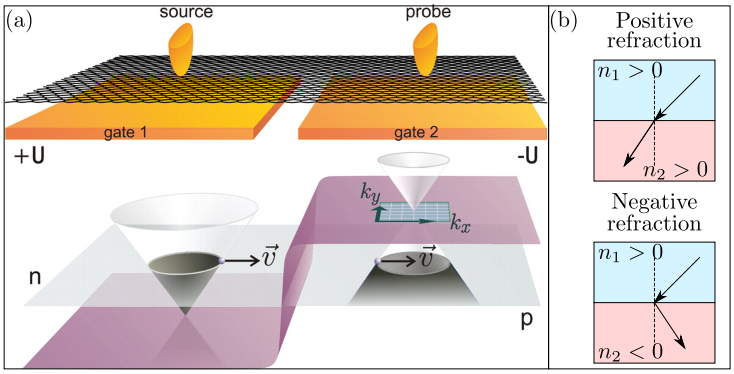

Figure 1.5: Schematic representation of a graphene p-n junction. In the upper panel (a), a graphene sheet is placed over a split gate in order to create n-type (left) and p-type (right) polarizations. Lower panel (a) shows the change in Fermi level in relation to the touching point between the valence band and the conduction band. Upper panel (b) illustrates conventional (positive) refraction, while lower panel (b) illustrates negative refraction. Panel (a) was adapted from Ref. [2].

when the Klein tunneling in graphene was investigated, the angle of incidence in region 1, with gate potential V_1, was defined as $\tan\theta_1 = q_{1y}/q_{1x}$ and the angle of refraction in region 2, with gate potential V_2, as $\tan\theta_2 = q_{2y}/q_{2x}$. Since the wavevector in the y-direction is conserved, the relation between the angles of incidence and refraction is:

$$\frac{\sin\theta_1}{\sin\theta_2} = \frac{q_2}{q_1} = \frac{E - V_2}{E - V_1}, \tag{1.14}$$

E being the energy of the electron. Therefore, for $V_1 = 0$ and $V_2 > 0$, whenever $0 < E < V_2$, the angle of refraction will be negative, just as for $V_2 = 0$ and $V_1 > 0$, whenever $0 < E < V_1$. A schematic representation of both positive and negative refraction is shown in Fig. 1.5(b).

1.1.6 *Graphene nanoribbons*

The presence of edges in graphene gives rise to so-called graphene nanoribbons and affects the band structure at the low-energy limit. Graphene nanoribbons can be synthesized through experiments such as lithographic patterning of graphene samples[26], chemical methods (solution-dispersion and sonication[27]), and carbon nanotube cutting[28]. A bottom-up approach can also synthesize linear two-dimensional graphene nanoribbons with lengths of up to 12 nm[29]. There are two basic types of edges, namely, armchair and zigzag, schematically illustrated in Figs. 1.6(a) and 1.6(b), respectively. In Fig. 1.6(a), the width W_a is defined in terms of the number of dimer lines, N_a, as $W_a = a[(N_a - 3)\sqrt{3}/2 + \sqrt{3}]$. Similarly, in Fig. 1.6(b), the width W_z is defined in terms

of the number of zigzag lines, N_z, as $W_z = a(3N_z/2 - 1)$. It is assumed that the dangling bonds at the edges are terminated by hydrogen atoms that do not contribute to the eigenstates near the Fermi level[30].

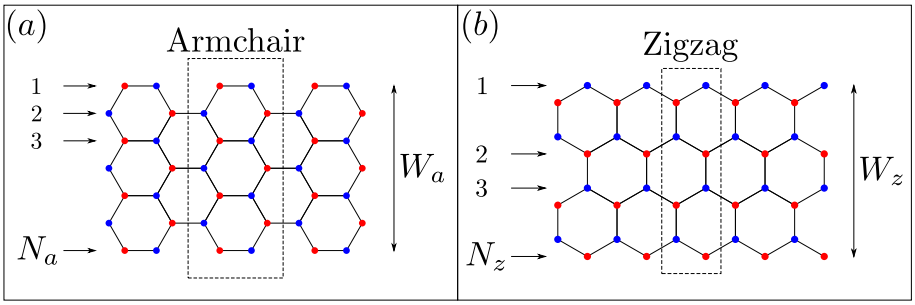

Figure 1.6: (a) armchair and (b) zigzag type edge. N_a and N_z are related, respectively, with the widths W_a and W_z. Dashed rectangles represent unit cells.

The procedure used in Subsection 1.1.2 to obtain the energy bands of graphene can be used here to obtain the energy bands of graphene nanoribbons. For the armchair case:

$$E_{\pm}(k) = st\sqrt{1 + 2\epsilon_p \cos(k/2) + \epsilon_p^2}, \tag{1.15}$$

where $\epsilon_p = 2\cos(p)$, with $p = r\pi/(N_a+1)$ $(r = 1, 2, ..., N_a)$. It is noted by Eq. (1.15) that $E_{\pm}(k) = 0$ at $k = 0$ if $N_a = 3r - 1$, resulting in metallic behavior. Otherwise, *i.e.* if $N_a \neq 3r - 1$, the behavior will be semiconductor, with the band gap decreasing with increasing width, approaching zero at the limit where N_a is very large. Furthermore, one obtains $E_{\pm}(k) = s(1 + \epsilon_p)$ at $k = 0$ by Eq. (1.15), so that the band gap will be 0 if $N_a = 3r - 1$, $2t\{1 + \cos[3r\pi/(3r + 1)]\}$ if $N_a = 3r$, or $2t\{1 + \cos[(3r + 1)\pi/(3r + 2)]\}$ if $N_a = 3r + 1$[30]. The eigenstates, in turn, are:

$$\begin{pmatrix} \Psi_{r,A} \\ \Psi_{r,B} \end{pmatrix} = N_c \begin{pmatrix} -s\sqrt{\epsilon_p + \exp(-ik/2)} \\ \sqrt{\epsilon_p + \exp(ik/2)} \end{pmatrix} \sin(rp), \tag{1.16}$$

where:

$$N_c = \frac{1}{\sqrt{|E|}} \left[N_a - \frac{\sin(N_a p)}{\sin(p)} \cos[(N_a + 1)p] \right]^{-1/2}. \tag{1.17}$$

In contrast to the armchair case, graphene nanoribbons with zigzag edges have localized edge eigenstates (implying partially flat energy bands) with energies close to the Fermi level. In this sense, it is convenient to separate the energy bands between localized and extended eigenstates. Let $k_c = 2\arccos[\pm 1/(1 + 1/N_z)]$. Thus, if $E_{\pm}(k) > 0$ and $0 \leq k \leq k_c^L$, there are N_z extended eigenstates. On the other hand, if $E_{\pm}(k) > 0$ and $k_c^L \leq k$

$\leq \pi$, there are $N_z - 1$ extended eigenstates and 1 localized eigenstate. The energy bands for extended eigenstates are:

$$E_{\pm}(k) = s\sqrt{1 + g_k^2 + 2g_k \cos(p)}, \tag{1.18}$$

where $g_k = 2\cos(k/2)$ and p is the solution of:

$$\sin(pN_z) + g_k \sin[p(N_z + 1)] = 0. \tag{1.19}$$

It is noted by Eq. (1.19) that there are N_z solutions if $0 \leq k \leq k_c^L$ or $k_c^R \leq k \leq 2\pi$ and $N_z - 1$ solutions if $k_c^L < k < k_c^R$. The extended eigenstates, in turn, are:

$$\begin{pmatrix} \Psi_{r,A} \\ \Psi_{r,B} \end{pmatrix} = N_c \begin{pmatrix} -s\sin[p(N_z + 1 - r)] \\ \sin(rp) \end{pmatrix}. \tag{1.20}$$

Likewise, the energy bands for localized eigenstates are:

$$E_{\pm}(k) = s\sqrt{1 + g_k^2 - 2|g_k| \cosh(\eta)}, \tag{1.21}$$

where η is the solution of:

$$\sinh(\eta N_z) + |g_k| \sinh[\eta(N_z + 1)] = 0. \tag{1.22}$$

The localized eigenstates, in turn, are:

$$\begin{pmatrix} \Psi_{r,A} \\ \Psi_{r,B} \end{pmatrix} = N_c \exp(i\pi r) \begin{pmatrix} \exp[i\pi(N_z + 1)] \sinh[\eta(N_z + 1 - r)] \\ \sin(r\eta) \end{pmatrix}. \tag{1.23}$$

This Subsection was based on Ref. [30], where there is a detailed description of the electronic properties of graphene nanoribbons.

1.2 Electronic transport and computational method

Numerical simulation of the behavior of charge carriers in a scattering region is of particular importance in condensed matter physics. In this sense, the KWANT appears as a significant alternative[31]. Based on the Python programming language, KWANT is a free open source package for numerical calculations on tight-binding models with a strong focus on quantum transport. Although it is also suitable for finite physical systems, its main objective is to describe infinite physical systems, which can be considered as a

finite scattering region connected to semi-infinite leads. In the context of the Landauer-Büttiker formalism, leads act as wave guides that transport plane waves into and out of the scattering region and correspond to the contacts of a quantum transport experiment[31]. The procedure used by KWANT for numerical calculations can be easily understood by means of a one-dimensional example. Generalization to larger dimensions is immediate. The one-dimensional example consists of a scattering region connected to only one lead, as schematically illustrated in Fig. 1.7.

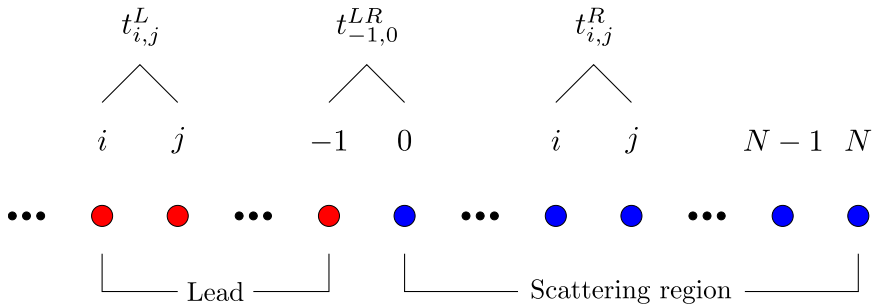

Figure 1.7: Semi-infinite linear chain. $t^L_{i,j}$ ($t^R_{i,j}$) is the hopping parameter between adjacent sites of the lead (scattering region) and $t^{LR}_{-1,0}$ is the hopping parameter between sites -1 and 0 in the interface that separates the lead and the scattering region.

Fig. 1.7 shows a scattering region (finite linear chain at $[0, N]$) connected to a lead (semi-infinite linear chain at $]-\infty, -1]$). The Hamiltonian has the form:

$$\mathcal{H} = \mathcal{H}_L + \mathcal{H}_R + \mathcal{H}_{LR}, \tag{1.24}$$

where $\mathcal{H}_L$ is the Hamiltonian of the lead, $\mathcal{H}_R$ is the Hamiltonian of the scattering region, and $\mathcal{H}_{LR}$ is the Hamiltonian of the connection between the lead and the scattering region. Considering that electrons can only hop to the first neighbors of a site, Hamiltonians $\mathcal{H}_L$, $\mathcal{H}_R$, and $\mathcal{H}_{LR}$ can be written in terms of creation and annihilation operators as:

$$\mathcal{H}_L = t^L_{i,j} \sum_{\langle i,j \rangle} L_i^\dagger L_j, \tag{1.25}$$

$$\mathcal{H}_R = t^R_{i,j} \sum_{\langle i,j \rangle} R_i^\dagger R_j, \tag{1.26}$$

$$\mathcal{H}_{LR} = t^{LR}_{i,j} \sum_{\langle i,j \rangle} (R_i^\dagger L_j + \text{H.c.}), \tag{1.27}$$

where $t^L_{i,j}$, $t^R_{i,j}$, and $t^{LR}_{i,j}$ are the hopping parameters between sites that are first neighbors, respectively, of the lead, the scattering region, and the connection between the lead and the scattering region. L_i ($L_i^\dagger$) is an operator that annihilates (creates) an eigenstate at

site i of the lead and R_i ($R_i^\dagger$) is an operator that annihilates (creates) an eigenstate at site i of the scattering region. In second quantization language, the one-particle eigenstates for the lead and for the scattering region are, respectively:

$$|\Psi_L\rangle = \sum_n a_n L_n^\dagger |0\rangle, \tag{1.28}$$

$$|\Psi_R\rangle = \sum_n b_n R_n^\dagger |0\rangle, \tag{1.29}$$

where $|0\rangle$ denotes a vacuum eigenstate. Indices of all sums are taken in the same range, *i.e.* $]-\infty, N]$, implying in $a_0 = a_1 = ... = a_N = 0$ for the coefficients related to the lead, and $b_{-\infty} = ... = b_{-2} = b_{-1} = 0$ for the coefficients related to the scattering region. Acting the Hamiltonian (1.24) in $|\Psi\rangle = |\Psi_L\rangle + |\Psi_R\rangle$, with the replacement of Eqs. (1.25), (1.26), and (1.27), the following eigenvalue equation is obtained:

$$\sum_{\langle i,j\rangle,n} [t_{i,j}^L L_i^\dagger L_j + t_{i,j}^R R_i^\dagger R_j + t_{i,j}^{LR}(R_i^\dagger L_j + L_i^\dagger R_j)](a_n L_n^\dagger + b_n R_n^\dagger)|0\rangle = \sum_n E(a_n L_n^\dagger + b_n R_n^\dagger)|0\rangle, \tag{1.30}$$

creation and annihilation operators for fermions satisfy the anticommutation rules:

$$\{c_i^\dagger, c_j^\dagger\} = \{c_i, c_j\} = 0, \quad \{c_i, c_j^\dagger\} = \delta_{ij}, \quad c = L, R, \tag{1.31}$$

thus, the left term of Eq. (1.30) can be rewritten as:

$$\sum_{\langle i\rangle,n} [t_{i,n}^L L_i^\dagger L_n a_n L_n^\dagger + t_{i,n}^R R_i^\dagger R_n b_n R_n^\dagger + t_{i,n}^{LR} R_i^\dagger L_n a_n L_n^\dagger + t_{i,n}^{LR} L_i^\dagger R_n b_n R_n^\dagger]|0\rangle, \tag{1.32}$$

let:

$$A_i = \sum_n (a_n t_{i,n}^L + b_n t_{i,n}^{LR}), \tag{1.33}$$

$$B_i = \sum_n (a_n t_{i,n}^{LR} + b_n t_{i,n}^R), \tag{1.34}$$

thus, Eq. (1.30) can be rewritten as:

$$\sum_{\langle i\rangle} (A_i L_i^\dagger + B_i R_i^\dagger)|0\rangle = \sum_{\langle i\rangle} E(a_i L_i^\dagger + b_i R_i^\dagger)|0\rangle, \tag{1.35}$$

therefore:

$$Ea_i = a_i \epsilon_i^L + \sum_{n\neq i} (a_n t_{i,n}^L + b_n t_{i,n}^{LR}), \tag{1.36}$$

$$Eb_i = b_i \epsilon_i^R + \sum_{n\neq i} (a_n t_{i,n}^{LR} + b_n t_{i,n}^R), \tag{1.37}$$

where $\epsilon_i^{L(R)} = t_{i,i}^{L(R)}$ is the on-site energy. Since only interactions between sites that are first neighbors are considered, Eqs. (1.36) and (1.37) can be rewritten as:

$$Ea_i = a_i\epsilon_i^L + a_{i+1}t_{i,i+1}^L + a_{i-1}t_{i,i-1}^L + b_{i+1}t_{i,i+1}^{LR} + b_{i-1}t_{i,i-1}^{LR}, \tag{1.38}$$

$$Eb_i = b_i\epsilon_i^R + b_{i+1}t_{i,i+1}^R + b_{i-1}t_{i,i-1}^R + a_{i+1}t_{i,i+1}^{LR} + a_{i-1}t_{i,i-1}^{LR}, \tag{1.39}$$

in matrix form, Eqs. (1.38) and (1.39) are:

$$\begin{pmatrix} H_L & V_{LR} \\ V_{LR}^\dagger & H_R \end{pmatrix} \begin{pmatrix} A \\ B \end{pmatrix} = E \begin{pmatrix} A \\ B \end{pmatrix}, \tag{1.40}$$

where $A = [... \quad a_{-3} \quad a_{-2} \quad a_{-1}]^T$ and $B = [b_0 \quad b_1 \quad ... \quad b_N]^T$. H_L, H_R, and V_{LR} are, respectively:

$$H_L = \begin{pmatrix} \ddots & \ddots & \ddots & & \\ & t_{-3,-4}^L & \epsilon_{-3}^L & t_{-3,-2}^L & \\ & & t_{-2,-3}^L & \epsilon_{-2}^L & t_{-2,-1}^L \\ & & & t_{-1,-2}^L & \epsilon_{-1}^L \end{pmatrix}, \tag{1.41}$$

$$H_R = \begin{pmatrix} \epsilon_0^R & t_{0,1}^R & & & \\ t_{1,0}^R & \epsilon_1^R & t_{1,2}^R & & \\ & & \ddots & & \\ & & t_{N-1,N-2}^R & \epsilon_{N-1}^R & t_{N-1,N}^R \\ & & & t_{N,N-1}^R & \epsilon_N^R \end{pmatrix}, \tag{1.42}$$

$$V_{LR} = \begin{pmatrix} \vdots & \vdots & \\ 0 & 0 & ... \\ t_{-1,0}^{LR} & 0 & ... \end{pmatrix}, \tag{1.43}$$

in this description, H_L represents the lead, H_R represents the scattering region, and V_{LR} represents the connection between them. For two or more dimensions, Eq. (1.40) is generalized to the following tridiagonal block matrix[31]:

$$H = \begin{pmatrix} \ddots & \ddots & \ddots & & \\ & V_L^\dagger & H_L & V_L & \\ & & V_L^\dagger & H_L & V_{LR} \\ & & & V_{LR}^\dagger & H_R \end{pmatrix}, \tag{1.44}$$

where H_R is the (typically large) Hamiltonian matrix of the scattering region, H_L is the (typically much smaller than H_R) Hamiltonian matrix of one unit cell of the lead, V_L is

the Hamiltonian matrix connecting one unit cell of the lead to the next, and V_{LR} is the hopping parameter between the scattering region and the lead.

The wave function, in turn, is defined as $\Psi = [..., \psi(2)^L, \psi(1)^L, \psi^R]$, where $\psi(i)^L$ corresponds to the solution for the i-th unit cell of the lead and ψ^R corresponds to the solution for the scattering region. Assuming a solution $\phi_n(j) = (\lambda_n)^j \chi_n$, where χ_n is the n-th eigenvector and λ_n is the n-th eigenvalue, the time-independent Schrödinger equation has the form:

$$(V_L^\dagger \lambda_n + V_L \lambda_n^{-1} + H_L)\chi_n = E\chi_n, \tag{1.45}$$

by the requirement of normalization of the wave function, $|\lambda_n| \leq 1$. Transverse modes with $|\lambda_n| < 1$ are evanescent, that is, corresponds to the solutions that approach zero at infinity, and transverse modes with $|\lambda_n| = 1$ are propagating. Thus, the eigenstate corresponding to the transverse mode n of a unit cell of the lead has the form:

$$\psi_n(i) = \phi_n(i)^{in} + \sum_m S_{mn}\phi_m(i)^{out} + \sum_p \tilde{S}_{pn}\phi_p(i)^{ev}, \tag{1.46}$$

where $\phi_n(i)^{in}$, $\phi_m(i)^{out}$, and $\phi_p(i)^{ev}$ represent, respectively, the input, output, and evanescent transverse modes. The eigenstate corresponding to the transverse mode n of the scattering region has the form $\psi_n(0) = \phi_n^R$. S_{mn} in Eq. (1.46) is called the scattering matrix and gives the transmission probability from transverse mode m to transverse mode n as $T_{mn} = |S_{mn}|^2$. From the scattering matrix, the conductance is obtained through the Landauer formula as[31]:

$$G_{ab} = \frac{e^2}{h} \sum_{n\in a, m\in b} |S_{nm}|^2. \tag{1.47}$$

The importance of the discussion on electronic transport in mesoscopic systems for ballistic conductors can be justified by the fact that it was reported that 40 nm wide graphene nanoribbons grown epitaxially on silicon carbide are single channel ballistic conductors at room temperature in a size scale greater than 10 μm[32].

1.3 Thesis organization

This Thesis is organized as follows. In Chapter 2, we will review the tight-binding model in first and second quantization and show how it can be used to calculate the energy spectrum of some crystals. In Chapter 3, we will investigate current modulation

in graphene p-n junctions using electric and magnetic fields. In Chapter 4, we will study the ballistic transport of electrons through three-terminal graphene-based devices. In Chapter 5, we will explore the effect of long-range impurity potentials on the persistent current of graphene quantum rings in the presence of an uniform perpendicular magnetic field. Finally, in Chapter 6, we will summarize our main findings and conclusions.

2 TIGHT-BINDING MODEL IN FIRST AND SECOND QUANTIZATION

In this Chapter, we review the tight-binding model in first and second quantization and show how it can be used to calculate the energy spectrum of some crystals. From an approach based on the Schrödinger equation (first quantization), we demonstrate the procedure for writing a generic Hamiltonian in the second quantization formalism. The connection between these two formalisms is generally not discussed in technical and applied works. As application examples, we use both methodologies to calculate the energy spectrum of a linear chain and a square lattice analytically, initially considering only one site per unit cell and later taking two sites per unit cell. Next, we apply the tight-binding model to graphene and compare such description with the brick lattice, showing that graphene lattice can be mapped as a square lattice with some hopping parameters being neglected. Finally, we apply the model to the τ_3-lattice, a three band system. In all cases, we present the energy spectrum and the density of states.

2.1 Introduction

Quantum mechanics is rightly seen as one of the greatest triumphs of 20th century theoretical physics. The theory explained not only several experimental results that had baffled researchers at the beginning of the last century, but it also made important predictions that were later verified and are now recognized as the microscopic basis for all chemistry and materials science. However, soon after elaborating the first mathematically consistent formalism of quantum mechanics, it was realized that one would often face apparently insurmountable difficulties to obtain results from the theory. That first becomes evident as one tries to apply the theory to the problem of the energy spectrum of atoms heavier than hydrogen, even disregarding the dynamics of the nucleus. In this case, the solution of the Schrödinger's equation is complicated since the wave function is dependent on $3N$ variables, with N being the number of electrons in the system, and the potential involves the electron-electron Coulomb interaction, apart from the coupling

with the nucleus. Therefore, in order to calculate the properties of atoms and molecules, one is forced to use analytical approximations and numerical approaches, such as density functional theory[33], which frequently lead to time-consuming numerical calculations.

Thus, it may come as a surprise that in the case of solids, simple and accurate approximations have been found, allowing the prediction of several properties of these systems. This is due to some aspects of the physics of materials that seem to conspire to allow the calculation of electronic structures in a relatively simple way. The first is that crystals are characterized by having atoms sitting in a periodic lattice, *i.e.* the lowest energy configuration consists of a repeating pattern which, in turn, creates a periodic electron-ion potential. The periodicity of the potential leads naturally to Bloch's theorem and the prediction of energy bands[34]. A second factor is the fermionic character of the electrons, which means that they must obey Pauli's exclusion principle. This principle prevents more than two electrons (allowing for spin degeneracy) from occupying the same energy levels. Consequently, as more atoms are added to the system the total number of electrons increases, and those have to occupy even higher energies, up to a certain level, known as the Fermi energy. Thus, for many properties of interest such as thermal and electronic transport in crystals, only the highest energy states are relevant, viz. states with energies close to the Fermi level. It also happens that, for electrons with total energies in that range, their kinetic energies will usually far surpass the electron-electron interaction energies. This means that for these electrons, the coupling between electrons can often be disregarded. Moreover, since the periodic lattice potential is obtained from atomic potentials, this causes the lower-energy electrons to be more strongly bound to the host atoms, resulting that the dynamics of the so-called core electrons can often be neglected in the calculations as well.

Therefore, one is left with a picture of (approximately) independent electrons moving in a periodic potential generated by the ionic cores. The wave functions of those independent electrons can be written as linear combinations of the orbitals of isolated atoms[35], an approximation that can be justified by assuming that each electron is strongly bound to a single core, with some probability of tunneling to neighboring sites in the lattice. Such approximation is thus known as a tight-binding (TB) model. An important property of such models is that they allow the inclusion of additional terms, such as electron-electron coupling, electron-phonon or spin-orbit interaction terms in a

systematic way, as corrections to the single-particle picture.

By employing such a model, a fairly comprehensive understanding of solids can be obtained. In this Chapter, we show a brief introduction of TB models applied to 1D and 2D materials. Quasi-two-dimensional systems contain a single or a few layers of crystalline atoms and have first been brought to attention due to graphene production in 2004[8]. Since then, various lamellar crystals have been produced, which have been modeled using TB models that provide a good description of the energy bands in the vicinity of the Fermi level.

This Chapter is organized as follows. In Section 2.2 (2.3), we present the first (second) quantization formalism for the TB model. In Section 2.4, we show the equivalences between first and second quantization formalisms of the TB model within the approach used. In Section 2.5, we describe a procedure that can be used to obtain the band structure of some materials, as done in Section 2.6 for five crystal lattices, namely: linear chain, square lattice, brick lattice (square lattice model of graphene), graphene and τ_3-lattice. We summarize our main findings and draw some perspectives in Section 2.7.

2.2 First quantization formalism

The TB model consists of writing the electron's wave function as a linear combination of atomic orbitals, with procedure name in abbreviated format as LCAO, taking into account the various sites of a given crystal. Thus, in the TB model, states and energies in a crystal are determined from localized atomic orbitals. We assume that the electron is strongly bound to the nucleus in these orbitals, which means that it is confined to a region of small dimensions compared to internuclear distances. It is an approach that successfully describes several materials[36–39], making it possible to obtain different electronic and transport properties[40–44]. Despite being a reasonably simple model, it can take into account complex phenomena, such as the quantum Hall effect in graphene with an AC electric field[45].

In the following Subsections, we present a procedure to determine the eigenvalues of the Hamiltonian by the first quantization formalism within the TB model.

2.2.1 *Linear combination of atomic orbitals*

Let us assume that in the vicinity of each lattice site the total Hamiltonian $\mathcal{H}$ can be approximated by the Hamiltonian of the localized atoms, $\mathcal{H}_{at}$. Additionally, it is also assumed that atomic orbitals, $\varphi_j(\mathbf{r},\mathbf{k})$, are well-localized, so that:

$$\mathcal{H}_{at}\varphi_j(\mathbf{r},\mathbf{k}) = \varepsilon_j\varphi_j(\mathbf{r},\mathbf{k}), \tag{2.1}$$

where ε_j are energy eigenvalues and $\varphi_j(\mathbf{r},\mathbf{k})$ will be negligible when $|\mathbf{r}|$ exceeds a distance of the order of the lattice parameter. One can improve the approximation by considering the case where $|\mathbf{r}|$ is comparable to the lattice parameter. For this, one can include an additional term, $\Delta U(\mathbf{r})$, to the Hamiltonian of the localized atoms containing all corrections to the atomic potential necessary to produce the periodic potential of the crystal:

$$\mathcal{H} = \mathcal{H}_{at} + \Delta U(\mathbf{r}). \tag{2.2}$$

In this case, taking an atom localized at the origin, the wave function $\varphi_j(\mathbf{r},\mathbf{k})$ will be a good approximation to a steady-state wave function for the total Hamiltonian, with energy eigenvalues ε_j[46]. Likewise, the wave functions $\varphi_j(\mathbf{r}-\mathbf{R})$ will be good approximations for the corresponding sites $\mathbf{R}$ of the Bravais lattice.

Since, by assumption, $\varphi_j(\mathbf{r},\mathbf{k})$ satisfies the Schrödinger equation for the localized atoms [Eq. (2.1)], then it must also satisfy the Schrödinger equation for the total Hamiltonian [Eq. (2.2)], whenever $\Delta U(\mathbf{r})$ is null and $\varphi_j(\mathbf{r},\mathbf{k})$ is non-null. In this situation, each level n of the localized atoms gives rise to N levels in the periodic potential of the crystal, with wave functions $\varphi_j(\mathbf{r}-\mathbf{R})$, since N is the number of unit cells. Thus, one needs to find the N linear combinations of these states that represent the Bloch function $\Phi_j(\mathbf{r},\mathbf{k})$ that describe the electrons in the crystal, *i.e.*:

$$T_{\mathbf{R}}\Phi_j(\mathbf{r},\mathbf{k}) = e^{i\mathbf{k}\cdot\mathbf{R}}\Phi_j(\mathbf{r},\mathbf{k}), \tag{2.3}$$

where $T_{\mathbf{R}}$ is the translation operation along the lattice vector $\mathbf{R}$. At this point, the main assumption of the TB method emerges, *i.e.* to assume that the Bloch function can be given in terms of the atomic orbitals:

$$\Phi_j(\mathbf{r},\mathbf{k}) = \frac{1}{\sqrt{N}}\sum_{\mathbf{R}} e^{i\mathbf{k}\cdot\mathbf{R}}\varphi_j(\mathbf{r}-\mathbf{R}), \quad j = 1,2,...,n, \tag{2.4}$$

where n is the number of atomic wave functions in the unit cell and we have n Bloch functions in the solid for a given $\mathbf{k}$. For each state j, one takes the contribution of the N corresponding localized atoms, weighted by a phase factor $e^{i\mathbf{k}\cdot\mathbf{R}}$ in the Bravais lattice, with the term $1/\sqrt{N}$ being a normalization constant[47].

Although the wave function (2.4) satisfies Bloch's theorem for a given $\mathbf{k}$, it represents only the electronic characteristics of localized atoms, requiring modifications to fully represent the electrons in the crystal. As a first approximation, we consider that $\Delta U(\mathbf{r})$ would be vanish whenever $\varphi_j(\mathbf{r},\mathbf{k})$ was non-zero. However, a more realistic assumption is that $\varphi_j(\mathbf{r},\mathbf{k})$ becomes small but not exactly null before $\Delta U(\mathbf{r})$ becomes appreciable[46]. Thus, the wave function that describes the electrons in the crystal can be similar to the Bloch function, given by:

$$\Psi_j(\mathbf{r},\mathbf{k}) = \frac{1}{\sqrt{N}}\sum_{\mathbf{R}} e^{i\mathbf{k}\cdot\mathbf{R}}\psi_j(\mathbf{r}-\mathbf{R}), \quad j = 1, 2, ..., n, \tag{2.5}$$

with $\psi_j(\mathbf{r}-\mathbf{R})$ to be determined and being not necessarily an exact atomic steady-state wave function. Considering $\Delta U(\mathbf{r})\varphi_j(\mathbf{r},\mathbf{k})$ very small, but different from zero, we can write $\psi_j(\mathbf{r}-\mathbf{R})$ as a linear combination of localized atomic wave functions:

$$\psi_j(\mathbf{r}-\mathbf{R}) = \sum_{j'} C_{jj'}\varphi_{j'}(\mathbf{r}-\mathbf{R}), \tag{2.6}$$

where $C_{jj'}$ are complex coefficients to be found. To better understand that, note from Eqs. (2.5) and (2.6) that:

$$\begin{aligned}\Psi_j(\mathbf{r},\mathbf{k}) &= \frac{1}{\sqrt{N}}\sum_{\mathbf{R}} e^{i\mathbf{k}\cdot\mathbf{R}}\sum_{j'} C_{jj'}\varphi_{j'}(\mathbf{r}-\mathbf{R}) \\ &= \sum_{j'} C_{jj'}\frac{1}{\sqrt{N}}\sum_{\mathbf{R}} e^{i\mathbf{k}\cdot\mathbf{R}}\varphi_{j'}(\mathbf{r}-\mathbf{R}),\end{aligned} \tag{2.7}$$

and using Eq. (2.4), we have[47]:

$$\Psi_j(\mathbf{r},\mathbf{k}) = \sum_{j'} C_{jj'}\Phi_{j'}(\mathbf{r},\mathbf{k}), \tag{2.8}$$

therefore, the wave function that describes the electrons in the crystal, $\Psi_j(\mathbf{r},\mathbf{k})$, is ultimately a linear combination of the atomic orbitals $\varphi_{j'}(\mathbf{r}-\mathbf{R})$.

2.2.2 *Secular equation*

The energy eigenvalues $E_i = E_i(\mathbf{k})$ of the total Hamiltonian $\mathcal{H}$ are given by:

$$E_i = \frac{\langle\Psi_i|\mathcal{H}|\Psi_i\rangle}{\langle\Psi_i|\Psi_i\rangle}. \tag{2.9}$$

Replacing Eq. (2.8) into Eq. (2.9), we obtain:

$$E_i = \frac{\sum_{j,j'} \mathcal{H}_{jj'} C_{ij}^* C_{ij'}}{\sum_{j,j'} \mathcal{S}_{jj'} C_{ij}^* C_{ij'}}, \tag{2.10}$$

where the integrals over the Bloch orbitals, $\mathcal{H}_{jj'} = \mathcal{H}_{jj'}(\mathbf{k})$ and $\mathcal{S}_{jj'} = \mathcal{S}_{jj'}(\mathbf{k})$ are called the transfer integral matrices and overlap integral matrices[47], or simply transfer[1] and overlap matrices, respectively, and are defined by:

$$\mathcal{H}_{jj'} = \langle \Phi_j | \mathcal{H} | \Phi_{j'} \rangle, \quad j, j' = 1, 2, ..., n, \tag{2.11}$$

$$\mathcal{S}_{jj'} = \langle \Phi_j | \Phi_{j'} \rangle, \quad j, j' = 1, 2, ..., n. \tag{2.12}$$

Substituting the Bloch function, Eq. (2.4), into Eq. (2.11), the transfer matrix elements become:

$$\mathcal{H}_{jj'} = \frac{1}{N} \sum_{\mathbf{R},\mathbf{R}'} e^{i\mathbf{k}\cdot(\mathbf{R}'-\mathbf{R})} t_{\mathbf{R},\mathbf{R}'}, \tag{2.13}$$

where we define:

$$t_{\mathbf{R},\mathbf{R}'} = \langle \varphi_j(\mathbf{r}-\mathbf{R}) | \mathcal{H} | \varphi_{j'}(\mathbf{r}-\mathbf{R}') \rangle, \tag{2.14}$$

as the transfer integral or hopping parameter related to the interacting energy between electrons located on different sites[49] and usually has a negative value[47], *i.e.* this energetic term is associated with the energy required for an electron to "hop" from a site at position $\mathbf{R}'$ to a given site at position $\mathbf{R}$, or vice versa. If the distance between the sites increases, then the corresponding hopping parameter is reduced in module. In general, the band structure is initially calculated by means of first principles methods and then a search is done for the hopping parameters that best fit the energy bands obtained by the TB method to those obtained by the first principles calculations[47], in a similar way as done in the Wannierization procedure of density functional theory[50].

Likewise, replacing the Bloch function, Eq. (2.4), into Eq. (2.12), the overlap matrix elements can be written as:

$$\mathcal{S}_{jj'} = \frac{1}{N} \sum_{\mathbf{R},\mathbf{R}'} e^{i\mathbf{k}\cdot(\mathbf{R}'-\mathbf{R})} s_{\mathbf{R},\mathbf{R}'}, \tag{2.15}$$

where we define:

$$s_{\mathbf{R},\mathbf{R}'} = \langle \varphi_j(\mathbf{r}-\mathbf{R}) | \varphi_{j'}(\mathbf{r}-\mathbf{R}') \rangle, \tag{2.16}$$

[1]Note that the method's name referred here as transfer matrix is also given to another method associated with scattering problems in quantum mechanics and electromagnetism (see Ref. [48]).

as the overlap integral or overlap parameter, which represents the overlap between the atomic orbitals of the $\mathbf{R}$ and $\mathbf{R}'$ sites. For instance, if one considers the overlap parameter corresponding to the atomic orbitals of the $\mathbf{R}$ and $\mathbf{R}' = \mathbf{R}$ sites, one finds $s_{\mathbf{R},\mathbf{R}'} = \delta_{jj'}$. In general, it is preferable to consider an orthonormal model, where $s_{\mathbf{R},\mathbf{R}'} = \delta_{\mathbf{R}\mathbf{R}'}\delta_{jj'}$. In this situation, the overlap matrix will be the identity matrix. In a more general case, we have $0 \leq s_{\mathbf{R},\mathbf{R}'} \leq 1$. Most of the applications of the TB method found in the literature, usually one only takes into account the contributions of nearest neighbor (NN) sites for hopping and overlap parameters. However, a more accurate description must consider also contributions of more distant neighbors.

Let us now return to the discussion of Eq. (2.10). The complex coefficients C_{ij}^* are obtained so that the energy eigenvalues E_i are minimized[47], *i.e.* by doing:

$$\frac{\partial E_i}{\partial C_{ij}^*} = \frac{\sum_{j'} \mathcal{H}_{jj'} C_{ij'}}{\sum_{j,j'} \mathcal{S}_{jj'} C_{ij}^* C_{ij'}} - \frac{\sum_{j,j'} \mathcal{H}_{jj'} C_{ij}^* C_{ij'}}{\left(\sum_{j,j'} \mathcal{S}_{jj'} C_{ij}^* C_{ij'}\right)^2} \sum_{j'} \mathcal{S}_{jj'} C_{ij'} = 0. \tag{2.17}$$

Multiplying Eq. (2.17) by $\sum_{j,j'} \mathcal{S}_{jj'} C_{ij}^* C_{ij'}$ and substituting Eq. (2.10) into Eq. (2.17), one obtains:

$$\sum_{j'} \mathcal{H}_{jj'} C_{ij'} = E_i \sum_{j'} \mathcal{S}_{jj'} C_{ij'}. \tag{2.18}$$

Defining a column vector such as:

$$C_i = \begin{bmatrix} C_{i1} \\ \vdots \\ C_{1N} \end{bmatrix}, \tag{2.19}$$

one can rewrite Eq. (2.18) as:

$$\mathcal{H} C_i = E_i \mathcal{S} C_i \Rightarrow [\mathcal{H} - E_i \mathcal{S}] C_i = 0. \tag{2.20}$$

Note that if the inverse of the matrix $[\mathcal{H} - E_i\mathcal{S}]$ exists, then we have:

$$[\mathcal{H} - E_i\mathcal{S}][\mathcal{H} - E_i\mathcal{S}]^{-1} C_i = 0 \Rightarrow C_i = 0, \tag{2.21}$$

resulting in the trivial solution. However, we are only interested in the case where the matrix inverse does not exist, that is, in the case where $[\mathcal{H} - E_i\mathcal{S}]$ is a singular matrix, therefore:

$$\det[\mathcal{H} - E\mathcal{S}] = 0. \tag{2.22}$$

This equation, an important result of the TB method, is known as the secular equation. Due to the dimensionality n of the matrix $\mathcal{H}$, its solution provides n eigenvalues E_i's with $i = 1, \ldots, n$. In the case of an orthonormal TB model, the overlap matrix is the identity matrix, so that:

$$\det[\mathcal{H} - E\mathbf{I}] = 0. \tag{2.23}$$

2.3 Hamiltonian in second quantization

The TB model in first quantization as described above is sufficient to determine the band structure of crystals of interest. However, in the technical literature, the Hamiltonian is generally presented in second quantization, that is, in terms of creation and annihilation operators. In general, it is always possible to describe fermions in terms of such operators. Unlike bosons, fermions obey the Pauli exclusion principle. Representing an operator that creates (annihilates) an electron in the s-state by $\hat{c}_s^\dagger$ ($\hat{c}_s$) and defining an unoccupied state by $|0\rangle$, the Pauli exclusion principle imposes that $\hat{c}_s^\dagger \hat{c}_s^\dagger |0\rangle = 0$ or equivalently $\hat{c}_s^\dagger |1\rangle = 0$. Other relations satisfied by operators $\hat{c}_s^\dagger$ and $\hat{c}_s$ are $\hat{c}_s^\dagger |0\rangle = |1\rangle$, $\hat{c}_s |1\rangle = |0\rangle$, and $\hat{c}_s |0\rangle = 0$. In addition, the operator $\hat{c}_s^\dagger \hat{c}_s$ provides the occupation of the s-state, that is, $\hat{c}_s^\dagger \hat{c}_s |n\rangle = n|n\rangle$, where $n = 0, 1$. The $\hat{c}_s^\dagger$ and $\hat{c}_s$ operators satisfy an anti-commutation rule: $\{\hat{c}_s, \hat{c}_s^\dagger\} = \hat{c}_s \hat{c}_s^\dagger + \hat{c}_s^\dagger \hat{c}_s = 1$. In short, all these relations can be obtained using the following expressions[51]:

$$\{\hat{a}_r, \hat{a}_s^\dagger\} = \delta_{rs}, \ \{\hat{a}_r, \hat{a}_s\} = 0, \text{ and } \{\hat{a}_r^\dagger, \hat{a}_s^\dagger\} = 0. \tag{2.24}$$

Therefore, using the operators $\hat{c}_s^\dagger$ and $\hat{c}_s$, we must begin our discussion by merely reformulating the Schrödinger equation in the language of second quantization. There are works in the literature that present the development of the second quantization formalism starting from the first quantization formalism[51, 52]. We call the general Hamiltonian the one that has not yet been reduced to the TB model, that is, the one that describes physical systems that do not necessarily obey the assumption of TB approximations discussed above. For this, one can consider the general Hamiltonian in the language of first quantization being written as:

$$H = \sum_k T(x_k) + \frac{1}{2} \sum_{k \neq l} V(x_k, x_l), \tag{2.25}$$

where $T \equiv T(x_k)$ is the kinetic energy, $V \equiv V(x_k, x_l)$ is the potential energy, and x_k and x_l denote the coordinates of the k-th and l-th particles, respectively, that are linked by

the interaction V. Using the algebra of the creation and annihilation operators, one can rewrite the general Hamiltonian (2.25) as[51]:

$$\hat{H} = \sum_{ij} \hat{c}_i^\dagger \langle i|T|j\rangle \hat{c}_j + \frac{1}{2} \sum_{ijkl} \hat{c}_i^\dagger \hat{c}_j^\dagger \langle ij|V|kl\rangle \hat{c}_l \hat{c}_k, \tag{2.26}$$

where $\hat{H}$ is an operator in the abstract occupation-number space and, therefore, it is a general Hamiltonian in the language of second quantization.

By comparing Eqs. (2.25) and (2.26), it is seen that in first quantization the kinetic and potential energies are written in terms of momentum and position operators. On the other hand, in second quantization the operators of creation and annihilation are present. The transformation of the general Hamiltonian, initially written in terms of position and momentum operators, into occupation number representation is often called the second quantization procedure and is an useful formalism to describe and analyze quantum many-body systems.

In general, a generic one-body operator:

$$J = \sum_i J(x_i), \tag{2.27}$$

written in first-quantized form, has its correspondent second-quantized operator given by[51]:

$$\hat{J} = \sum_{ij} \langle i|J|j\rangle \hat{c}_i^\dagger \hat{c}_j. \tag{2.28}$$

Thus, neglecting the electron-electron interaction, we can write the general Hamiltonian in second quantization admitting $J = \mathcal{H}$ in Eq. (2.28), as:

$$\hat{\mathcal{H}} = \sum_{ij} \langle i|\mathcal{H}|j\rangle \hat{c}_i^\dagger \hat{c}_j, \tag{2.29}$$

where i and j are generic wave functions. At this point, note that if the term $\langle i|\mathcal{H}|j\rangle$ is associated with the hopping parameter t_{ij} [see Eq. (2.14)], with i and j representing atomic orbitals, then the general Hamiltonian (2.29) undergoes the TB approximation. Thus, the TB Hamiltonian in second quantization is given by:

$$\hat{\mathcal{H}} = \sum_{ij} t_{ij} \hat{c}_i^\dagger \hat{c}_j. \tag{2.30}$$

In principle, the sum runs over all orbitals of all atomic sites that make up the crystallographic lattice. However, the number of neighbors, and consequently the number of

hopping parameters, can be controlled, being the TB model more accurate as more non-vanishing hopping energies are taken into account. For example, the TB Hamiltonian that includes nearest-neighbor (NN) and next-nearest-neighbor (NNN) sites, with one orbital per site, can generally be written as:

$$\hat{\mathcal{H}} = \sum_i E_i \hat{c}_i^\dagger \hat{c}_i + \sum_{\langle ij \rangle} t \hat{c}_i^\dagger \hat{c}_j + \sum_{\langle\langle ij \rangle\rangle} t' \hat{c}_i^\dagger \hat{c}_j, \tag{2.31}$$

where $E_i \equiv \langle i|\hat{\mathcal{H}}|i\rangle$ is the energy of placing an electron at the lattice site i, called on-site energy[49]. t and t' are the hopping parameters of the NN-sites ($\langle ij \rangle$) and NNN-sites ($\langle\langle ij \rangle\rangle$), respectively, *i.e.* they are energy terms $\langle i|\hat{\mathcal{H}}|j\rangle$ for $i \neq j$ regarding site connections with distances $|\mathbf{r}_i - \mathbf{r}_j| > |\mathbf{R}|$ greater than the one or more lattice parameters for NN and NNN case, respectively. In summary, TB models that admit one orbital per site, one has that: (i) if $i = j$, then $t_{ii} = E_i$, *i.e.* the on-site energy, and (ii) if $i \neq j$, then i and j can denote either non-equivalent sites in the unit cell, or equivalent sites separated by lattices vectors.

2.4 Tight-binding model in first and second quantization

In the previous Sections, we presented the formulations for the TB model in first and second quantization. In this Section, we shall show the equivalence between these two frameworks within the approach used.

2.4.1 *From the second to the first quantization*

Let us now demonstrate that the Hamiltonian in second quantization [see Eq. (2.30)] leads to the transfer integral matrix [Eq. (2.11)]. Aiming to this, consider that the creation and annihilation operators at site i are $\hat{c}_i^\dagger$ and $\hat{c}_i$, respectively. Let us first Fourier transform these operators, leading them to the momentum space:

$$\hat{c}_i = \frac{1}{\sqrt{N}} \sum_{\mathbf{k}} e^{i\mathbf{k}\cdot\mathbf{r}_i} \hat{c}_{\mathbf{k}}^i, \tag{2.32}$$

$$\hat{c}_i^\dagger = \frac{1}{\sqrt{N}} \sum_{\mathbf{k}} e^{-i\mathbf{k}\cdot\mathbf{r}_i} \hat{c}_{\mathbf{k}}^{i\dagger}. \tag{2.33}$$

The next step is to replace Eqs. (2.32) and (2.33) into Eq. (2.30) for the crystallographic lattice. The resulting equation is simplified by the following identity:

$$\delta_{\mathbf{k}\mathbf{k}'} = \frac{1}{N} \sum_i e^{\pm i(\mathbf{k}-\mathbf{k}')\cdot\mathbf{r}_i}. \tag{2.34}$$

Following these steps, and defining the pseudo-spinor in the Nambu representation, such as:

$$|\Psi_{\mathbf{k}}\rangle = (\hat{c}^1_{\mathbf{k}} \quad \hat{c}^2_{\mathbf{k}} \quad ... \quad \hat{c}^n_{\mathbf{k}})^T, \tag{2.35}$$

one gets the general demonstration as shown below:

$$\begin{aligned}
\hat{\mathcal{H}} &= \sum_{ij} t_{ij}\hat{c}^\dagger_i\hat{c}_j \\
&= \frac{1}{N}\sum_{ij}\sum_{\mathbf{k}} t_{ij}e^{-i\mathbf{k}\cdot\mathbf{r}_i}\hat{c}^{i\dagger}_{\mathbf{k}}\sum_{\mathbf{k}'} e^{i\mathbf{k}'\cdot\mathbf{r}_j}\hat{c}^j_{\mathbf{k}'} \\
&= \frac{1}{N}\sum_{ij}\sum_{\mathbf{k}\mathbf{k}'} t_{ij}e^{i\mathbf{k}'\cdot(\mathbf{r}_j-\mathbf{r}_i)}e^{-i(\mathbf{k}-\mathbf{k}')\cdot\mathbf{r}_i}\hat{c}^{i\dagger}_{\mathbf{k}}\hat{c}^j_{\mathbf{k}'} \\
&= \frac{1}{N}\sum_{i}\sum_{\mathbf{k}\mathbf{k}'} \mathcal{H}_{ij}(\mathbf{k}')e^{-i(\mathbf{k}-\mathbf{k}')\cdot\mathbf{r}_i}\hat{c}^{i\dagger}_{\mathbf{k}}\hat{c}^j_{\mathbf{k}'} \\
&= \sum_{\mathbf{k}\mathbf{k}'} \delta_{\mathbf{k}\mathbf{k}'}\mathcal{H}_{ij}(\mathbf{k}')\hat{c}^{i\dagger}_{\mathbf{k}}\hat{c}^j_{\mathbf{k}'} \\
&= \sum_{\mathbf{k}} \hat{c}^{i\dagger}_{\mathbf{k}}\mathcal{H}_{ij}(\mathbf{k})\hat{c}^j_{\mathbf{k}} \\
&= \sum_{\mathbf{k}} \langle\hat{\Psi}_{\mathbf{k}}|\mathcal{H}|\hat{\Psi}_{\mathbf{k}}\rangle,
\end{aligned} \tag{2.36}$$

being used Eq. (2.13) in the above development.

As an example of the path from second to first quantization, consider a lattice with two non-equivalent sites in the unit cell: A and B. The creation and annihilation operators at site localized by $\mathbf{r}_i$ of the A (B) sublattice are respectively $\hat{a}^\dagger_i$ ($\hat{b}^\dagger_i$) and $\hat{a}_i$ ($\hat{b}_i$). Thus, according to the steps indicated before, assuming a null on-site energy and taking non-null hoppings just between non-equivalent sites, one has the following direct

demonstration:

$$
\begin{aligned}
\hat{\mathcal{H}} &= \sum_{ij} t_{ij}\hat{c}_i^\dagger \hat{c}_j \\
&= \frac{1}{N}\sum_{ij}\sum_{\mathbf{k}'} t_{ij}e^{-i\mathbf{k}'\cdot\mathbf{r}_j}\hat{b}_{\mathbf{k}'}^\dagger \sum_{\mathbf{k}} e^{i\mathbf{k}\cdot\mathbf{r}_i}\hat{a}_{\mathbf{k}} + \frac{1}{N}\sum_{ij}\sum_{\mathbf{k}} t_{ij}e^{-i\mathbf{k}\cdot\mathbf{r}_i}\hat{a}_{\mathbf{k}}^\dagger \sum_{\mathbf{k}'} e^{i\mathbf{k}'\cdot\mathbf{r}_j}\hat{b}_{\mathbf{k}'} \\
&= \frac{1}{N}\sum_{ij}\sum_{\mathbf{k}\mathbf{k}'} t_{ij}e^{-i\mathbf{k}'\cdot(\mathbf{r}_j-\mathbf{r}_i)}e^{-i(\mathbf{k}'-\mathbf{k})\cdot\mathbf{r}_i}\hat{b}_{\mathbf{k}'}^\dagger\hat{a}_{\mathbf{k}} + \frac{1}{N}\sum_{ij}\sum_{\mathbf{k}\mathbf{k}'} t_{ij}e^{i\mathbf{k}'\cdot(\mathbf{r}_j-\mathbf{r}_i)}e^{-i(\mathbf{k}-\mathbf{k}')\cdot\mathbf{r}_i}\hat{a}_{\mathbf{k}}^\dagger\hat{b}_{\mathbf{k}'} \\
&= \frac{1}{N}\sum_{i}\sum_{\mathbf{k}\mathbf{k}'} \mathcal{H}_{AB}^*(\mathbf{k}')e^{-i(\mathbf{k}'-\mathbf{k})\cdot\mathbf{r}_i}\hat{b}_{\mathbf{k}'}^\dagger\hat{a}_{\mathbf{k}} + \frac{1}{N}\sum_{i}\sum_{\mathbf{k}\mathbf{k}'} \mathcal{H}_{AB}(\mathbf{k}')e^{-i(\mathbf{k}-\mathbf{k}')\cdot\mathbf{r}_i}\hat{a}_{\mathbf{k}}^\dagger\hat{b}_{\mathbf{k}'} \\
&= \sum_{\mathbf{k}\mathbf{k}'}\delta_{\mathbf{k}\mathbf{k}'}\left[\mathcal{H}_{AB}^*(\mathbf{k}')\hat{b}_{\mathbf{k}'}^\dagger\hat{a}_{\mathbf{k}} + \mathcal{H}_{AB}(\mathbf{k}')\hat{a}_{\mathbf{k}}^\dagger\hat{b}_{\mathbf{k}'}\right] \\
&= \sum_{\mathbf{k}}\left[\mathcal{H}_{AB}^*(\mathbf{k})\hat{b}_{\mathbf{k}}^\dagger\hat{a}_{\mathbf{k}} + \mathcal{H}_{AB}(\mathbf{k})\hat{a}_{\mathbf{k}}^\dagger\hat{b}_{\mathbf{k}}\right] \\
&= \sum_{\mathbf{k}}\begin{bmatrix}\hat{a}_{\mathbf{k}}^\dagger & \hat{b}_{\mathbf{k}}^\dagger\end{bmatrix}\begin{bmatrix}0 & \mathcal{H}_{AB}(\mathbf{k}) \\ \mathcal{H}_{AB}^*(\mathbf{k}) & 0\end{bmatrix}\begin{bmatrix}\hat{a}_{\mathbf{k}} \\ \hat{b}_{\mathbf{k}}\end{bmatrix} \\
&= \sum_{\mathbf{k}}\langle\hat{\Psi}_{\mathbf{k}}|\mathcal{H}|\hat{\Psi}_{\mathbf{k}}\rangle,
\end{aligned}
\tag{2.37}
$$

where $\mathcal{H}$ is the TB Hamiltonian in first quantization (transfer integral matrix) and $\hat{\mathcal{H}}$ is the corresponding TB Hamiltonian in second quantization.

In comparison with the LCAO, the overlap matrix in the second quantization language is supposed to always be equal the identity matrix. This restriction does not greatly reduce the generality of the method, because the TB model is generally used when in fact there is no overlap between the atomic functions of the sites. It is so true that the complete set of Bloch functions can be written as linear combinations of the the Wannier functions, which are orthogonal at different sites (or with different band indices) unlike TB atomic functions of LCAO. The Wannier functions form a complete orthogonal set, such that offer an alternative basis for an exact description of the independent electron levels in a crystal potential[46].

2.4.2 *From the first to the second quantization*

Starting from the resulting expression in Eq. (2.36) within the first quantization language, we are able to obtain the representation of the Hamiltonian in second quantization simply following the opposite path of this derivation. Therefore, after finding the transfer integral matrix by the first quantization TB model, one acts $\langle\Psi_{\mathbf{k}}|$ and $|\Psi_{\mathbf{k}}\rangle$

to the left and to the right of $\mathcal{H}$, respectively. Once done, we add a sum in $\mathbf{k}'$ with the Kronecker delta $\delta_{\mathbf{k}\mathbf{k}'}$ [see Eq. (2.34)]. This step does not change the Hamiltonian and ensures that we can identify the Fourier transforms of creation and annihilation operators [see Eqs. (2.32)-(2.33)]. In summary, these steps lead to:

$$\begin{aligned}
\hat{\mathcal{H}} &= \sum_{\mathbf{k}} \langle \hat{\Psi}_{\mathbf{k}} | \mathcal{H} | \hat{\Psi}_{\mathbf{k}} \rangle \\
&= \sum_{\mathbf{k}} \hat{c}^{i\dagger}_{\mathbf{k}} \mathcal{H}_{ij}(\mathbf{k}) \hat{c}^{j}_{\mathbf{k}} \\
&= \sum_{\mathbf{k}\mathbf{k}'} \delta_{\mathbf{k}\mathbf{k}'} \hat{c}^{i\dagger}_{\mathbf{k}} \mathcal{H}_{ij}(\mathbf{k}') \hat{c}^{j}_{\mathbf{k}'} \\
&= \sum_{\mathbf{k}\mathbf{k}'} \frac{1}{N} \sum_{i} e^{-i(\mathbf{k}-\mathbf{k}')\cdot\mathbf{r}_i} \hat{c}^{i\dagger}_{\mathbf{k}} \mathcal{H}_{ij}(\mathbf{k}') \hat{c}^{j}_{\mathbf{k}'} \\
&= \sum_{ij} \sum_{\mathbf{k}\mathbf{k}'} \frac{1}{N} e^{-i(\mathbf{k}-\mathbf{k}')\cdot\mathbf{r}_i} \hat{c}^{i\dagger}_{\mathbf{k}} t_{ij} e^{i\mathbf{k}'\cdot(\mathbf{r}_j-\mathbf{r}_i)} \hat{c}^{j}_{\mathbf{k}'} \\
&= \sum_{ij} t_{ij} \frac{1}{\sqrt{N}} \sum_{\mathbf{k}} e^{-i\mathbf{k}\cdot\mathbf{r}_i} \hat{c}^{i\dagger}_{\mathbf{k}} \frac{1}{\sqrt{N}} \sum_{\mathbf{k}'} e^{i\mathbf{k}'\cdot\mathbf{r}_j} \hat{c}^{j}_{\mathbf{k}'} \\
&= \sum_{ij} t_{ij} \hat{c}^{\dagger}_{i} \hat{c}_{j}, \qquad (2.38)
\end{aligned}$$

where $\mathcal{H}_{ij}$ are the transfer matrix elements, as represented in Eq. (2.11).

In Section 2.6 we compute the energy levels with the both formalisms for different one- and two-dimensional lattices with: one, two and three non-equivalent sites within the unit cell. Before that, in Section 2.5 we systematize the steps to obtain the energy spectrum starting from a real lattice.

2.5 Band structure calculation

In the previous Sections, we described the basic concepts of the TB method in first and second quantization. Let us now present the steps for applying the method to the calculation of band structures of crystals.

2.5.1 *Analysis of the crystal structure and the Bravais lattice*

One starts by identifying the lattice structure of the system. That may not be necessarily the actual crystal structure of the material, since depending on the level of precision and the energy range which one wants to describe, one can restrict the relevant orbitals to regard in the model. It allows in certain circumstances to neglect the hopping between some atomic sites, specially NNN connections. Then, an association of the

structure with a specific Bravais lattice is made (or with two or more Bravais sublattices). Taking the crystal structure and its unit cell containing information about the primitive vectors $\mathbf{a}_1$, $\mathbf{a}_2$, and $\mathbf{a}_3$, the coordinates of the atomic sites that form the unit cell base are then defined.

2.5.2 *Analysis of the reciprocal space and the first Brillouin zone*

The energy eigenvalues of the total Hamiltonian are periodic functions in the reciprocal space, which can be very neatly described within the first Brillouin zone, which is the Wigner-Seitz cell in the reciprocal space. Thus, the reciprocal lattice and the first Brillouin zone are built from the Bravais lattice determined in the previous item. The reciprocal lattice, defined by the primitive vectors $\mathbf{b}_1$, $\mathbf{b}_2$, and $\mathbf{b}_3$, is easily obtained from the primitive vectors of the Bravais lattice ($\mathbf{a}_1$, $\mathbf{a}_2$, and $\mathbf{a}_3$) by the relations:

$$\mathbf{b}_1 = 2\pi \frac{\mathbf{a}_2 \times \mathbf{a}_3}{\mathbf{a}_1 \cdot \mathbf{a}_2 \times \mathbf{a}_3}, \tag{2.39}$$

$$\mathbf{b}_2 = 2\pi \frac{\mathbf{a}_3 \times \mathbf{a}_1}{\mathbf{a}_1 \cdot \mathbf{a}_2 \times \mathbf{a}_3}, \tag{2.40}$$

$$\mathbf{b}_3 = 2\pi \frac{\mathbf{a}_1 \times \mathbf{a}_2}{\mathbf{a}_1 \cdot \mathbf{a}_2 \times \mathbf{a}_3}, \tag{2.41}$$

where each of the vectors defined by Eqs. (2.39)-(2.41) is perpendicular to two axes of the Bravais lattice, obeying therefore the following property: $\mathbf{b}_i \cdot \mathbf{a}_j = 2\pi\delta_{ij}$, being δ_{ij} the Kronecker delta[53].

2.5.3 *Determination of transfer and overlap matrices*

At this point, the calculation of the transfer integral matrix elements is done using the first or second quantization formalism. On the other hand, the overlap matrix elements are usually computed via first quantization, since in the second quantization the overlap matrix is always the identity matrix. The model used must be the one that provides the energy bands that best fit the results provided by the first principle calculations, without neglecting the essence of the approximation, which is the assumption of TB model itself.

Throughout the Chapter, we only consider interactions between NN sites. Due to the terms $\sum_{\mathbf{k}} \hat{c}_{\mathbf{k}}^{i\dagger} \mathcal{H}_{ij}(\mathbf{k}) \hat{c}_{\mathbf{k}}^{j}$ in Eqs. (2.36) and (2.38), each $\mathcal{H}_{ij}$ element is calculated admitting that the electron is annihilated (created) at sites of j (i) type. In addition, the

system coordinate origin for the $\mathcal{H}_{ij}$ computing is on a site i and one takes j to run over the NN sites assumed in the TB model for each investigated case.

2.5.4 *Energy eigenvalues*

Using the transfer integral and overlap matrices, the energy eigenvalues are obtained from the secular equation, Eq. (2.22).

2.5.5 *Density of states*

The evaluation of the density of states (DOS) is then performed by a superposition of individual energy states which we broaden using a Gaussian function:

$$f(E) = e^{-(E-E_0)^2/\gamma^2}, \tag{2.42}$$

with a broadening factor γ smaller than the energy levels separations. $\gamma = 0.05$ eV was assumed for all figures from here onward, unless otherwise stated[54].

2.6 Application examples

Let us now use the procedure described in the previous Sections to determine the energy bands of five crystal lattices, namely: [Figs. 2.1(a) and 2.1(b)] linear chain, [Figs. 2.1(c) and 2.1(d)] square lattice, [Fig. 2.1(e)] graphene, [Fig. 2.1(f)] brick lattice and [Fig. 2.1(g)] τ_3-lattice. The band structure of each crystal lattice is obtained by means of the TB method in first and second quantization. We consider only interactions between NN sites taking only one atomic orbital per site in all the following calculations. For linear chain and square lattices, two different situations are analyzed: the case of one and two sites per unit cell.

2.6.1 *Linear chain in first quantization*

Let us start with the simplest case, that is, the linear chain containing only one site per unit cell, as shown in Fig. 2.1(a). The primitive vectors of the real lattice and the reciprocal lattice are, respectively, $\mathbf{a}_1 = (a, 0, 0)$ and $\mathbf{b}_1 = (2\pi/a, 0, 0)$. The first Brillouin zone is specified by $-\pi/a \leq k \leq +\pi/a$, as seen in Fig. 2.2(a). The Bloch function is then written as:

$$\Phi_j(\mathbf{r}, \mathbf{k}) = \frac{1}{\sqrt{N}} \sum_{\mathbf{R}} e^{i\mathbf{k}\cdot\mathbf{R}} \varphi_j(\mathbf{r} - \mathbf{R}), \tag{2.43}$$

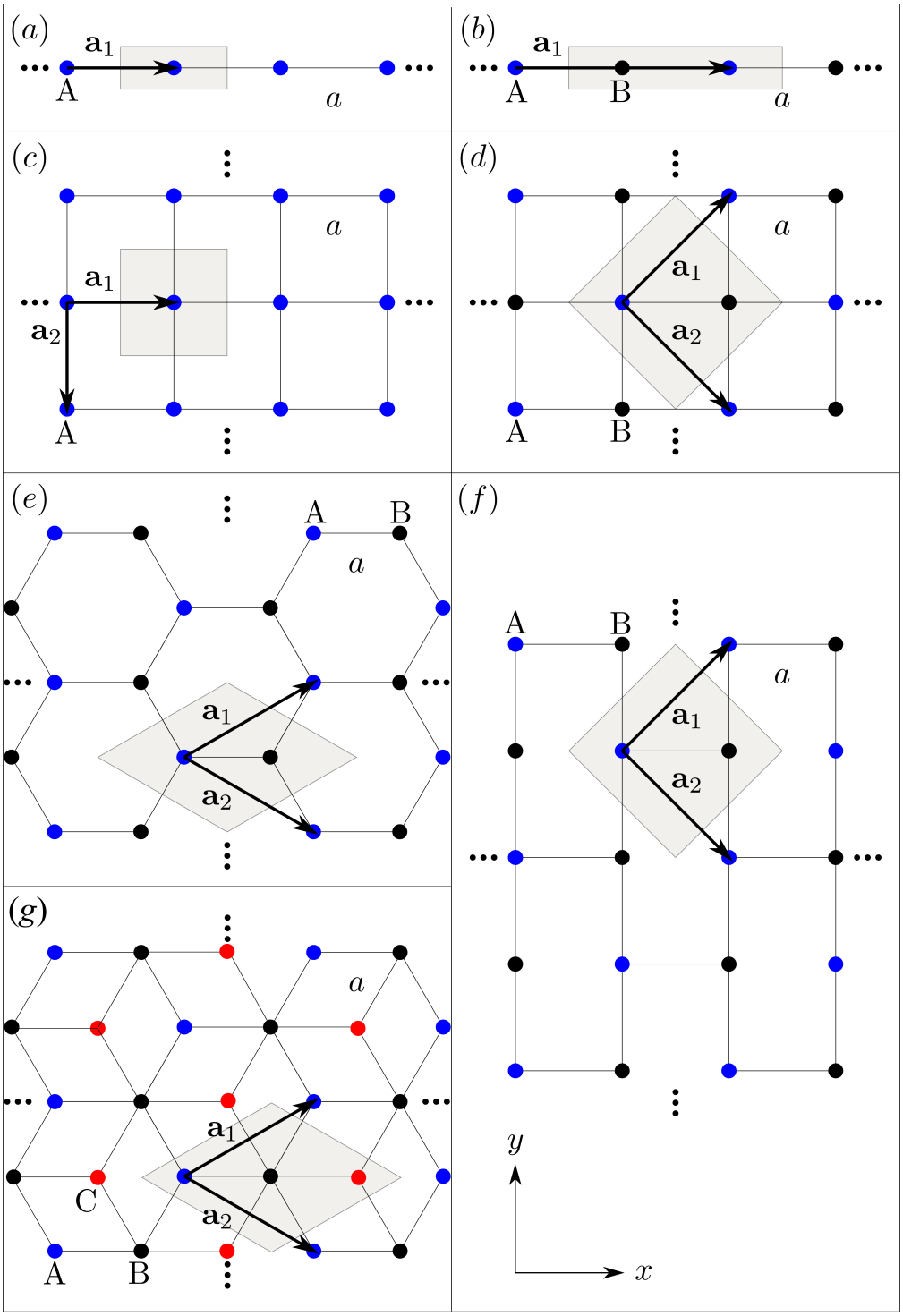

Figure 2.1: Crystal structures studied in this Chapter: linear chain with (a) one and (b) two sites in the unit cell, square lattice with (c) one and (d) two sites in the unit cell, (e) graphene, known as honeycomb lattice, (f) brick lattice, a square lattice with some neglected hopping parameters being topologically equivalent to graphene, and (g) τ_3-lattice, whose difference from graphene lies in the fact that it has an atom in the center of each hexagon. In all panels the lattice parameter is a, the primitive vectors are denoted by $\mathbf{a}_p$ $(p = 1, 2)$, and the unit cell is highlighted in gray.

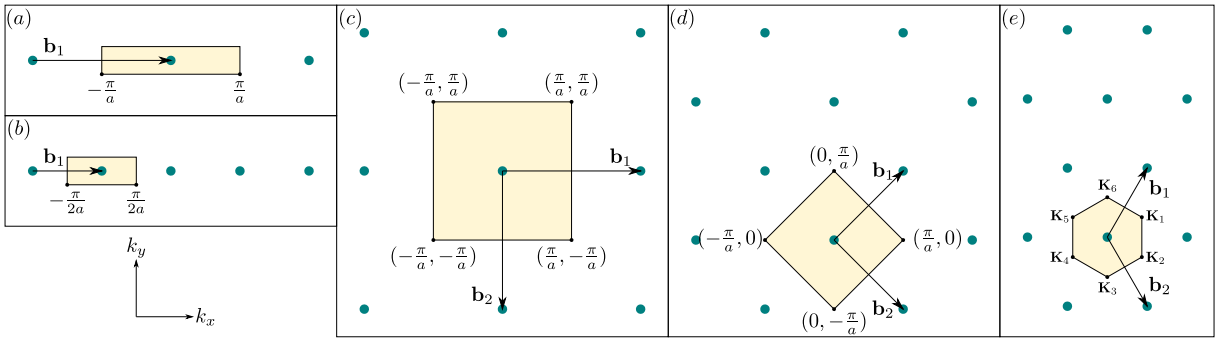

Figure 2.2: Reciprocal lattices of the investigated crystal structures of Fig. 2.1: (a) and (b) linear chain with one and two sites in the unit cell, respectively, (c) square lattice with one site in the unit cell, (d) square lattice with two sites in the unit cell and brick lattice, and (e) graphene and τ_3-lattice. Yellow shaded region highlights the first Brillouin zone and the primitive vectors are denoted by $\mathbf{b}_p$ ($p = 1, 2$). For graphene and τ_3-lattice, it is a hexagon with vertices $\mathbf{K}_1 = [2\pi/(3a), 2\pi/(3\sqrt{3}a)]$, $\mathbf{K}_2 = [2\pi/(3a), -2\pi/(3\sqrt{3}a)]$, $\mathbf{K}_3 = [0, -4\pi/(3\sqrt{3}a)]$, $\mathbf{K}_4 = [-2\pi/(3a), -2\pi/(3\sqrt{3}a)]$, $\mathbf{K}_5 = [-2\pi/(3a), 2\pi/(3\sqrt{3}a)]$, and $\mathbf{K}_6 = [0, 4\pi/(3\sqrt{3}a)]$. Of these six points, only two are not equivalent, which are called Dirac points in the graphene spectrum and are triply degenerate points in the τ_3-lattice spectrum.

so that the transfer integral matrix is:

$$\mathcal{H} = \frac{1}{N}\left(N\epsilon_0 + Nt\sum_{n=1}^{2} e^{i\mathbf{k}\cdot\mathbf{d}_n}\right) = \epsilon_0 + 2t\cos(ka), \tag{2.44}$$

where $\mathbf{d}_n$ are the NN sites: $\mathbf{d}_1 = (a, 0)$ and $\mathbf{d}_2 = (-a, 0)$. Due to the translation symmetry of this Bravais lattice, instead of taking all N sites in the summation of Eq. (2.44), one takes only one site and multiply it by N. Likewise, the overlap matrix is given by:

$$\mathcal{S} = \frac{1}{N}\left(N + Ns\sum_{n=1}^{2} e^{i\mathbf{k}\cdot\mathbf{d}_n}\right) = 1 + 2s\cos(ka). \tag{2.45}$$

Thus, the solution of Eq. (2.22) for the linear chain containing only one site in the unit cell is immediate and reads:

$$E(\mathbf{k}) = \frac{\epsilon_0 + 2t\cos(ka)}{1 + 2s\cos(ka)}. \tag{2.46}$$

Fig. 2.3(a) depicts the energy spectrum of a linear chain with one site per unit cell. Solid and dashed lines correspond to $s = 0$ and $s \neq 0$ cases, respectively. The plot is shown in an interval comprising of a unit cell at positive values of k, $0 \leq k \leq 2\pi/a$, to facilitate comparison with the other investigated cases here, whose energy spectra are plotted along of the high symmetry points in the region of positive values of k. Notice

that the nonzero overlap parameter (*i.e.* $s \neq 0$) causes a symmetry breaking with respect to $E = 0$. The region below (above) the zero level, $E = 0$, is compressed (extended) in relation to the energy axis, having its minimum (maximum) value in a smaller (larger) modulus than the case without overlap.

With two non-equivalent sites, A and B, per unit cell in the linear chain, as shown in Fig. 2.1(b), the primitive vectors of the real and reciprocal lattices are, respectively, $\mathbf{a}_1 = (2a, 0, 0)$ and $\mathbf{b}_1 = (\pi/a, 0, 0)$. Therefore, the first Brillouin zone, shown in Fig. 2.2(b), is specified by $-\pi/(2a) \leq k \leq +\pi/(2a)$, and the Bloch function, now consisting of A and B sites, is written as:

$$\Phi_j(\mathbf{r}, \mathbf{k}) = \frac{1}{\sqrt{N}} \sum_{\mathbf{R}_\alpha} e^{i\mathbf{k}\cdot\mathbf{R}_\alpha} \varphi_j(\mathbf{r} - \mathbf{R}_\alpha), \ \alpha = (A, B). \tag{2.47}$$

Once there are two atomic orbitals in the unit cell, the transfer integral and overlap matrices, $\mathcal{H}$ and $\mathcal{S}$, are both 2×2 matrices and given by:

$$\mathcal{H} = \begin{bmatrix} \mathcal{H}_{AA} & \mathcal{H}_{AB} \\ \mathcal{H}_{BA} & \mathcal{H}_{BB} \end{bmatrix}, \ \mathcal{S} = \begin{bmatrix} \mathcal{S}_{AA} & \mathcal{S}_{AB} \\ \mathcal{S}_{BA} & \mathcal{S}_{BB} \end{bmatrix}. \tag{2.48}$$

In this case, the NN sites are $\mathbf{d}_1 = (a, 0)$ and $\mathbf{d}_2 = (-a, 0)$. Thus, $\mathcal{H}_{AA} = \epsilon_A$, $\mathcal{H}_{BB} = \epsilon_B$, and $\mathcal{H}_{AB} = \mathcal{H}_{BA} = 2t\cos(ka)$. Likewise, we have $\mathcal{S}_{AA} = \mathcal{S}_{BB} = 1$ and $\mathcal{S}_{AB} = \mathcal{S}_{BA} = 2s\cos(ka)$. Thus, the secular equation is given by:

$$\det \begin{bmatrix} \epsilon_A - E_\pm(\mathbf{k}) & 2[t - sE_\pm(\mathbf{k})]\cos(ka) \\ 2[t - sE_\pm(\mathbf{k})]\cos(ka) & \epsilon_B - E_\pm(\mathbf{k}) \end{bmatrix} = 0. \tag{2.49}$$

If sites A and B are the same constituents, one has $\epsilon_A = \epsilon_B = \epsilon_0$, so that the resulting solution is:

$$E_\pm(\mathbf{k}) = \frac{\epsilon_0 \pm 2t\cos(ka)}{1 \pm 2s\cos(ka)}, \tag{2.50}$$

where $E_+(\mathbf{k})$ and $E_-(\mathbf{k})$ are degenerate at $ka = \pm\pi/2$ and are called bonding and anti-bonding energy bands[47], respectively. Fig. 2.3(b) shows the linear chain dispersion relation with two site per unit cell, where solid and dashed lines corresponding to null ($s = 0$) and non-null ($s \neq 0$) overlap cases, and the k interval ($0 \leq k \leq 2\pi/a$) is taken the same as in Fig. 2.3(a) to better comparison. Similarly to the case of one site per unit cell [Fig. 2.3(a)], the overlap breaks the energy symmetry with respect to $E = 0$ axis. Due to the existence of two non-equivalent sites, one obtains two energy bands E_+ (red lines) and E_- (blue lines), instead of only one as in the case of a single site, that are symmetrical in energy and momentum and which intersect each other at the zero energy level.

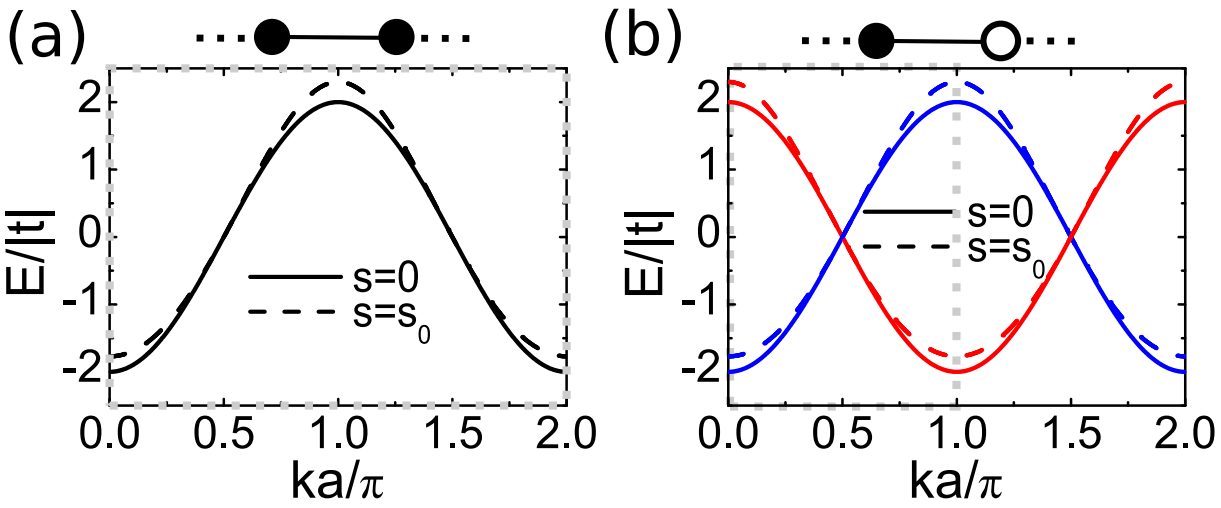

Figure 2.3: Energy spectrum of a linear chain with (a) one and (b) two sites per unit cell. Solid and dashed lines correspond to the cases with zero overlap ($s = 0$) and non-null overlap ($s \neq 0$), respectively. Blue and red lines in panel (b) denote the energy bands E_+ and E_-, respectively. Inspired by graphene case, for comparison purposes, we adopted $s_0 = 0.065$ and $t = -2.74$ eV[3]. The first Brillouin zone is highlighted by gray dashed line.

2.6.2 *Linear chain in second quantization*

In second quantization, the Hamiltonian for a linear chain with one site per unit cell can be written as:

$$\hat{\mathcal{H}} = \sum_i \epsilon_0 \hat{c}_i^\dagger \hat{c}_i + \sum_i t \left(\hat{c}_i^\dagger c_{i+1} + \hat{c}_{i+1}^\dagger c_i \right), \tag{2.51}$$

where the creation and annihilation operators act upon a basis of orthogonal states[55], $\epsilon_0 = t_{i,i}$ represents the energy of an electron at site i, and $t = t_{i,i+1}$ denotes the hopping energy associated with the sites i to $i+1$. $\hat{c}_i$ and $\hat{c}_i^\dagger$ can be expressed in the momentum space as:

$$\hat{c}_i = \frac{1}{\sqrt{N}} \sum_{\mathbf{k}} e^{i\mathbf{k}\cdot\mathbf{r}_i} \hat{c}_{\mathbf{k}}, \quad \hat{c}_i^\dagger = \frac{1}{\sqrt{N}} \sum_{\mathbf{k}} e^{-i\mathbf{k}\cdot\mathbf{r}_i} \hat{c}_{\mathbf{k}}^\dagger, \tag{2.52}$$

resulting, by replacing into Eq. (2.51), in:

$$\begin{aligned} \hat{\mathcal{H}} &= \sum_{\mathbf{k}} \hat{c}_{\mathbf{k}}^\dagger \frac{1}{N} \left(N\epsilon_0 + Nt \sum_{n=1}^{2} e^{i\mathbf{k}\cdot\mathbf{d}_n} \right) \hat{c}_{\mathbf{k}} \\ &= \sum_{\mathbf{k}} [\hat{c}_{\mathbf{k}}^\dagger \epsilon_0 \hat{c}_{\mathbf{k}} + \hat{c}_{\mathbf{k}}^\dagger t f(\mathbf{k}) \hat{c}_{\mathbf{k}}], \end{aligned} \tag{2.53}$$

where $f(\mathbf{k}) = \sum_{n=1}^{2} e^{i\mathbf{k}\cdot\mathbf{d}_n}$ is called the geometric structure factor[46]. Eq. (2.53) can be rewritten as:

$$\hat{\mathcal{H}} = \sum_{\mathbf{k}} \hat{c}_{\mathbf{k}}^\dagger [\epsilon_0 + t f(\mathbf{k})] \hat{c}_{\mathbf{k}} = \sum_{\mathbf{k}} \hat{c}_{\mathbf{k}}^\dagger \mathcal{H} \hat{c}_{\mathbf{k}}. \tag{2.54}$$

$\mathcal{H}$, in turn, is the transfer integral matrix [see Eq. (2.44)] and directly gives us the dispersion relation [see Fig. 2.3(a)]:

$$E(\mathbf{k}) = \epsilon_0 + 2t\cos(ka). \tag{2.55}$$

For the linear chain with two sites in the unit cell, the Hamiltonian reads:

$$\hat{\mathcal{H}} = \sum_i \epsilon_A a_i^\dagger a_i + \sum_j \epsilon_B b_j^\dagger b_j + \sum_{i,j} t\left(a_i^\dagger b_j + b_j^\dagger a_i\right), \tag{2.56}$$

where $\epsilon_{A(B)}$ represents the on-site energy of an electron at sublattice A (B) [see Fig. 2.1(b)], and t is the NN hopping parameter connecting the sublattices A and B. Using Eqs. (2.32)-(2.33) and taking $\epsilon_A = \epsilon_B = \epsilon_0$, the Hamiltonian (2.56) can be simplified to:

$$\hat{\mathcal{H}} = \sum_{\mathbf{k}} [a_{\mathbf{k}}^\dagger \epsilon_0 a_{\mathbf{k}} + b_{\mathbf{k}}^\dagger \epsilon_0 b_{\mathbf{k}} + a_{\mathbf{k}}^\dagger t f(\mathbf{k}) b_{\mathbf{k}} + b_{\mathbf{k}}^\dagger t f(\mathbf{k})^* a_{\mathbf{k}}], \tag{2.57}$$

which can be rewritten as:

$$\hat{\mathcal{H}} = \sum_{\mathbf{k}} \begin{bmatrix} a_{\mathbf{k}}^\dagger & b_{\mathbf{k}}^\dagger \end{bmatrix} \begin{bmatrix} \epsilon_0 & tf(\mathbf{k}) \\ tf(\mathbf{k})^* & \epsilon_0 \end{bmatrix} \begin{bmatrix} a_{\mathbf{k}} \\ b_{\mathbf{k}} \end{bmatrix} = \sum_{\mathbf{k}} \langle \Psi_{\mathbf{k}} | \mathcal{H} | \Psi_{\mathbf{k}} \rangle. \tag{2.58}$$

Diagonalizing the matrix form of the Hamiltonian of Eq. (2.58), we obtain the energy bands [see Fig. 2.3(b)], given by:

$$E_\pm(\mathbf{k}) = \epsilon_0 \pm 2t\cos(ka). \tag{2.59}$$

2.6.3 *Square lattice in first quantization*

Now, we present a similar calculation of how to obtain the energy bands for the square lattice with one and two atoms per unit cell. The former can be obtained by expanding the linear chain in two dimensions, as shown in Fig. 2.1(c). Its primitive vectors of the real and reciprocal lattices are $\mathbf{a}_1 = (a, 0, 0)$ and $\mathbf{a}_2 = (0, -a, 0)$, and $\mathbf{b}_1 = (2\pi/a, 0, 0)$ and $\mathbf{b}_2 = (0, -2\pi/a, 0)$, respectively. The first Brillouin zone, in turn, is specified by $-\pi/a \leq k_x \leq +\pi/a$ and $-\pi/a \leq k_y \leq +\pi/a$, as depicted in Fig. 2.2(c). The distances between NN sites are: $\mathbf{d}_1 = (a, 0)$, $\mathbf{d}_2 = (-a, 0)$, $\mathbf{d}_3 = (0, a)$, $\mathbf{d}_4 = (0, -a)$. Thus, the transfer integral matrix can be calculated as:

$$\begin{aligned} \mathcal{H} &= \frac{1}{N}\left(N\epsilon_0 + Nt\sum_{n=1}^{4} e^{i\mathbf{k}\cdot\mathbf{d}_n}\right) \\ &= \epsilon_0 + 2t[\cos(k_x a) + \cos(k_y a)], \end{aligned} \tag{2.60}$$

and likewise, the overlap matrix is written as:

$$\begin{aligned}\mathcal{S} &= \frac{1}{N}\left(N + Ns\sum_{n=1}^{4} e^{i\mathbf{k}\cdot\mathbf{d}_n}\right) \\ &= 1 + 2s[\cos(k_x a) + \cos(k_y a)]. \end{aligned} \tag{2.61}$$

Using $\mathcal{H}$ and $\mathcal{S}$ of Eqs. (2.60) and (2.61) into the secular equation (2.22), one obtains the energy band for the square lattice containing only one site in the unit cell, such as:

$$E(\mathbf{k}) = \frac{\epsilon_0 + 2t[\cos(k_x a) + \cos(k_y a)]}{1 + 2s[\cos(k_x a) + \cos(k_y a)]}. \tag{2.62}$$

Fig. 2.4(a) shows the energy spectrum by taking the overlap parameter $s = 0$ (solid line) and $s \neq 0$ (dashed line), along the high symmetry points $\mathbf{\Gamma} = (0, 0)$, $\mathbf{X} = (\pi/a, 0)$, and $\mathbf{M} = (\pi/a, \pi/a)$ as labeled in right contour plot panel, and the DOS for the square lattice with one site per unit cell. Right panels in Fig. 2.4(a) present contour plots of the bands for $s = 0$ and $s \neq 0$ cases, exhibiting an energy shift to high energy values, especially on the borders of the $\mathbf{\Gamma} - \mathbf{X}$ and $\mathbf{M} - \mathbf{\Gamma}$ directions, as also clearly seen in the left panel. Notice a symmetry breaking in the energy band and, consequently, in the DOS, with respect to zero energy when one regards a nonzero overlap contribution, similarly to the one observed in Fig. 2.3 for a non-null overlap energy in the linear chain. This electron-hole symmetry breaking caused by the overlap energy effect leads to a DOS imbalance around the large peak in $E = 0$.

Let us now consider the case of two, A and B, non-equivalent sites per unit cell for the square lattice, as illustrated in Fig. 2.1(d). The primitive real and reciprocal vectors are $\mathbf{a}_1 = (a, a, 0)$ and $\mathbf{a}_2 = (a, -a, 0)$, and $\mathbf{b}_1 = (\pi/a, \pi/a, 0)$ and $\mathbf{b}_2 = (\pi/a, -\pi/a, 0)$, respectively, and the distances between the NN atomic sites are the same as the previous case: $\mathbf{d}_1 = (a, 0)$, $\mathbf{d}_2 = (-a, 0)$, $\mathbf{d}_3 = (0, a)$, $\mathbf{d}_4 = (0, -a)$. The first Brillouin zone is defined in the following k-interval: $k_{x,y} \in [-\pi/a, \pi/a]$, as seen in Fig. 2.2(d). Thus, taking $\epsilon_A = \epsilon_B = \epsilon_0$, the resulting secular equation (2.22) is:

$$\det \begin{bmatrix} \Pi & \Delta \\ \Delta & \Pi \end{bmatrix} = 0, \tag{2.63}$$

where $\Delta = 2[t - sE_{\pm}(\mathbf{k})][\cos(k_x a) + \cos(k_y a)]$ and $\Pi = \epsilon_0 - E_{\pm}(\mathbf{k})$, leading to the following solution:

$$E_{\pm}(\mathbf{k}) = \frac{\epsilon_0 \pm 2t[\cos(k_x a) + \cos(k_y a)]}{1 \pm 2s[\cos(k_x a) + \cos(k_y a)]}. \tag{2.64}$$

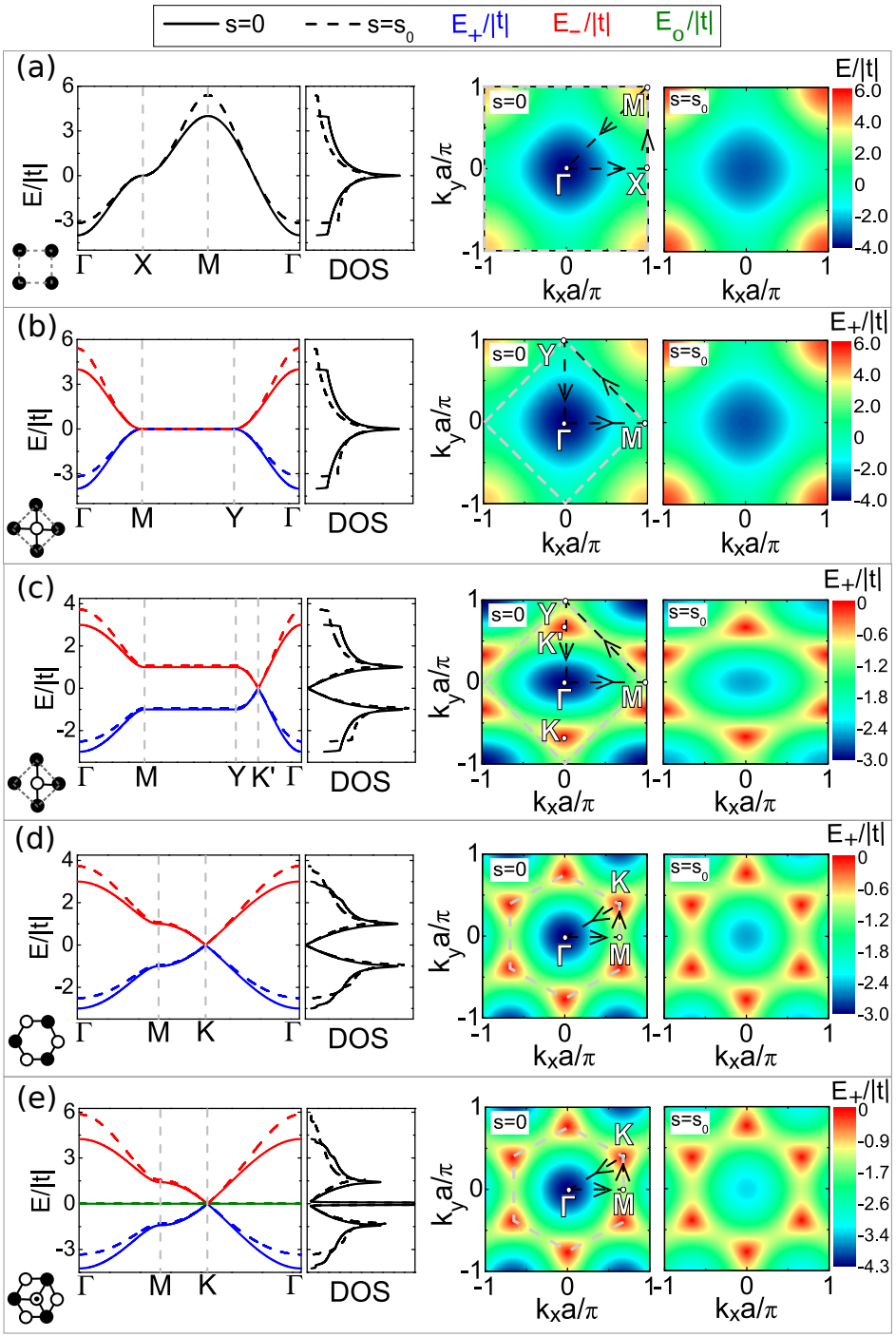

Figure 2.4: Energy spectrum and DOS for: square lattice with (a) one and (b) two atoms per unit cell, (c) brick lattice, (d) graphene, and (e) τ_3-lattice. Solid and dashed lines correspond to the cases with zero overlap ($s = 0$) and non-null overlap ($s \neq 0$), respectively. Blue, red, and green lines denote the energy bands E_+, E_-, and E_0, respectively. Inspired by graphene case, for comparison purposes, we adopted $s_0 = 0.065$ and $t = -2.74$ eV[3]. Right panels correspond to the contour plots of the conduction bands for $s = 0$ and $s \neq 0$, emphasizing the first Brillouin zone, highlighted by gray dashed line, the high symmetry points, and the paths taken for the energy plots in k-space.

Since the lattice has two atoms per unit cell, similarly to a two-level system, one obtains two bands E_+ and E_-, where $+$ and $-$ signs in Eq. (2.64) denote to electron and hole bands. The energy spectrum and DOS are shown in Figs. 2.4(b), where red and blue solid (dashed) lines correspond to $s = 0$ ($s \neq 0$) case for E_+ and E_- bands, respectively. The k-space direction is along the high symmetry points $\mathbf{\Gamma} = (0, 0)$, $\mathbf{M} = (\pi/a, 0)$, $\mathbf{Y} = (0, \pi/a)$, as indicated on the corresponding contour plot panel by the triangle along $\mathbf{\Gamma} - \mathbf{M} - \mathbf{Y} - \mathbf{\Gamma}$. As already discussed for the linear chain and square lattice with one site per unit cell, $s \neq 0$ parameter shifts non-equivalently the energy spectrum along the whole Brillouin zone breaking the electron-hole symmetry and causes an unbalance in the area under the DOS curve for positive and negative energy values. By the chosen k-space direction, the $\mathbf{M} - \mathbf{\Gamma}$-path has a flat band with both conduction and valence bands touching themselves at $E = 0$. In order to analyze the emergence of the second band in comparison to the square lattice case with one atom per unit cell, we depict in Fig. 2.5(a) the energy spectrum along the high symmetry points of square lattice with one site [see inset triangles in Figs. 2.4(a) and 2.5(a)]. It can be seen that the consideration of two non-equivalent sites brings up a second band (red line, E_-) obeying the electron-hole symmetry with respect to the one site already existing band, *i.e.* $E_+ = -E_-$.

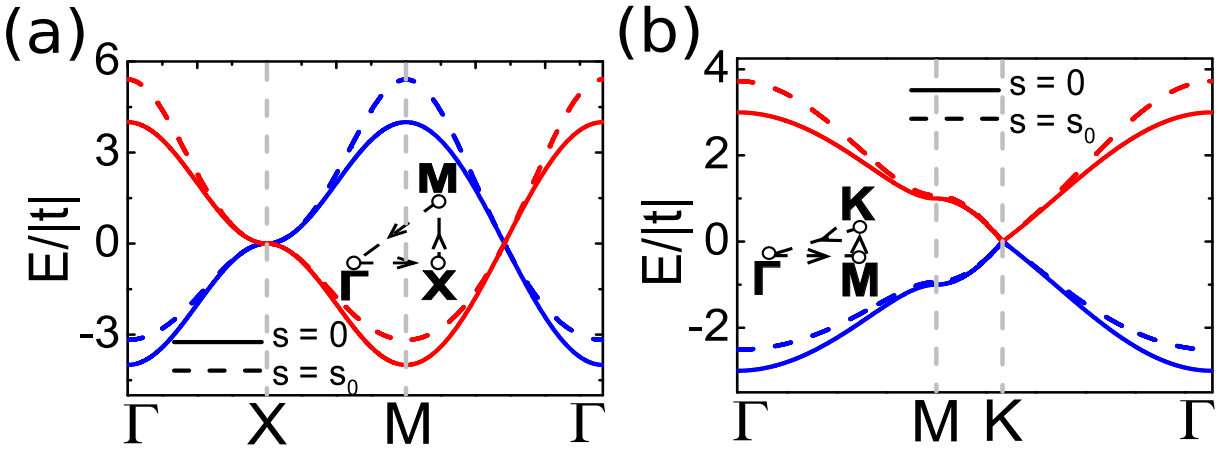

Figure 2.5: Energy spectrum of (a) the square lattice with two sites per unit cell, and (b) the brick lattice. The assumed k-space paths in (a) and (b) are illustrated in the inset of each panel, being similar to the ones for the square lattice with one site per unit cell and graphene, respectively, as shown in Figs. 2.4(a) and 2.4(e). It was adopted the same parameters as in Fig. 2.4.

2.6.4 *Square lattice in second quantization*

The Hamiltonian in second quantization for the square lattice with one site per unit cell can be written as:

$$\hat{\mathcal{H}} = \sum_i \epsilon_0 \hat{c}_i^\dagger \hat{c}_i + \sum_{i,j} t \hat{c}_i^\dagger \hat{c}_j. \tag{2.65}$$

For square lattice regarding only NN sites, each site i is connected to four other sites j [see Fig. 2.1(c)] with hopping energy t. The first term in Eq. (2.65) is associated with the on-site. Using Eqs. (2.32)-(2.33), the Hamiltonian (2.65) can be simplified to:

$$\hat{\mathcal{H}} = \sum_{\mathbf{k}} [\hat{c}_{\mathbf{k}}^\dagger \epsilon_0 \hat{c}_{\mathbf{k}} + \hat{c}_{\mathbf{k}}^\dagger t f(\mathbf{k}) \hat{c}_{\mathbf{k}}], \tag{2.66}$$

with the geometric structure factor being $f(\mathbf{k}) = \sum_{n=1}^{4} e^{i\mathbf{k}\cdot\mathbf{d}_n}$. Eq. (2.66) can be rewritten as:

$$\hat{\mathcal{H}} = \sum_{\mathbf{k}} \hat{c}_{\mathbf{k}}^\dagger \mathcal{H} \hat{c}_{\mathbf{k}}, \tag{2.67}$$

where it directly gives us the dispersion relation [see Fig. 2.4(a)]:

$$E(\mathbf{k}) = \epsilon_0 + 2t[\cos(k_x a) + \cos(k_y a)]. \tag{2.68}$$

In the same way, for two-site square lattice, the Hamiltonian in second quantization formalism reads:

$$\hat{\mathcal{H}} = \sum_i \epsilon_A a_i^\dagger a_i + \sum_j \epsilon_B b_j^\dagger b_j + \sum_{i,j} t \left(a_i^\dagger b_j + b_j^\dagger a_i \right), \tag{2.69}$$

where $\epsilon_{A,B}$ and t have the same definitions as in Eq. (2.56). Again, using Eqs. (2.32)-(2.33) and taking $\epsilon_A = \epsilon_B = \epsilon_0$, the Hamiltonian (2.69) can be simplified to:

$$\hat{\mathcal{H}} = \sum_{\mathbf{k}} \langle \Psi_{\mathbf{k}} | \mathcal{H} | \Psi_{\mathbf{k}} \rangle. \tag{2.70}$$

Diagonalizing Eq. (2.70), one gets the energy bands $\mathcal{H}$ as depicted in Figs. 2.4(b) and 2.5(a) and given by:

$$E_\pm(\mathbf{k}) = \epsilon_0 \pm 2t[\cos(k_x a) + \cos(k_y a)]. \tag{2.71}$$

2.6.5 *Brick lattice in first quantization*

Let us now describe a square lattice topologically similar to graphene that is defined with some hopping parameters being neglected, called brick lattice[56, 57]. As

we shall present, the energy spectra of both graphene and brick lattices are similar due to the equivalent topological lattice mapping between them within the TB model with interactions only between NN sites. Models for more general honeycomb crystal structures were investigated in Refs. [58] and [59]. To illustrate more examples of such similar lattice mapping, a square lattice model topologically equivalent to phosphorene (a puckered monolayer black phosphorus lattice with a highly anisotropic band structure) was investigated in Ref. [60], where different NN hopping values were assumed to simulate the phosphorene lattice anisotropy. Notice by assuming three non-vanishing NN hopping parameters in Fig. 2.1(d), that the brick lattice shown in Fig. 2.1(f) is topologically equivalent to the crystal structure of graphene shown in Fig. 2.1(e). Therefore, the theoretical development described in Subsection 2.6.3 for two-sites square lattice can be also adopted here. In this sense, the NN-sites with non-null hopping are: $\mathbf{d}_1 = (a, 0)$, $\mathbf{d}_2 = (0, a)$, $\mathbf{d}_3 = (0, -a)$. Thus, the transfer integral matrix elements are $\mathcal{H}_{AA} = \epsilon_A$, $\mathcal{H}_{BB} = \epsilon_B$, and:

$$\begin{aligned} \mathcal{H}_{AB} &= \frac{1}{N}\left(Nt\sum_{n=1}^{3} e^{i\mathbf{k}\cdot\mathbf{d}_n}\right) \\ &= t\left[e^{ik_x a} + 2\cos(k_y a)\right] \\ &= \mathcal{H}^*_{BA}, \end{aligned} \tag{2.72}$$

and the overlap matrix elements are $\mathcal{S}_{AA} = 1$, $\mathcal{S}_{BB} = 1$, and:

$$\begin{aligned} \mathcal{S}_{AB} &= \frac{1}{N}\left(Ns\sum_{n=1}^{3} e^{i\mathbf{k}\cdot\mathbf{d}_n}\right) \\ &= s\left[e^{ik_x a} + 2\cos(k_y a)\right] \\ &= \mathcal{S}^*_{BA}. \end{aligned} \tag{2.73}$$

Diagonalizing the secular equation (2.22) for the brick lattice by using Eqs. (2.72) and (2.73) and taking $\epsilon_A = \epsilon_B = \epsilon_0$, it results:

$$E_{\pm}(\mathbf{k}) = \frac{\epsilon_0 \pm |\mathcal{H}_{AB}|}{1 \pm |\mathcal{S}_{AB}|}, \tag{2.74}$$

where:

$$\begin{aligned} \frac{|\mathcal{H}_{AB}|}{t} &= \sqrt{3 + 2\cos(2k_y a) + 4\cos(k_y a)\cos(k_x a)} \\ &= \frac{|\mathcal{S}_{AB}|}{s}. \end{aligned} \tag{2.75}$$

Figs. 2.4(c) and 2.5(b) present the energy spectrum of brick lattice along the high symmetry points of square lattice with two sites per unit cell [as in Fig. 2.4(b)],

adding $\mathbf{K}' = [0, 2\pi/(3a)]$, *i.e.* it is shown along the $\mathbf{\Gamma} - \mathbf{M} - \mathbf{Y} - \mathbf{K}' - \mathbf{\Gamma}$-path, and displayed along high symmetry points $\mathbf{\Gamma} = (0, 0)$, $\mathbf{M} = (\pi/a, 0)$, and $\mathbf{K} = [\pi/a, \pi/(3a)]$, *i.e.* it is plotted along the $\mathbf{\Gamma}-\mathbf{M}-\mathbf{K}-\mathbf{\Gamma}$-path, which allows us to highlight the similarities with the two-site square lattice energy spectrum [Fig. 2.4(b)] and the graphene energy spectrum [Fig. 2.4(d)], respectively, as for instance, a non-dispersive behavior between $\mathbf{M}$ and $\mathbf{Y}$ points in a similar way to the square lattice case. Right panels in Fig. 2.4(c) show the contour plots of the conduction band for overlap parameter $s = 0$ and $s \neq 0$. Dashed gray and black lines denote the first Brillouin zone and k-space direction adopted to the 2D plot in the left panel of Fig. 2.4(c), respectively. Comparing the energy levels and DOS of brick lattice [Fig. 2.4(c)] and graphene [Fig. 2.4(d)], it is clear to note the existence of the two Dirac cones within the first Brillouin zone, two peaks in DOS associated with the van Hove singularities, and a null DOS value at $E = 0$. The main difference is that the energy spectrum of brick lattice is strained in comparison to the graphene spectrum, such that the positions of the high symmetry points in k-space for brick lattice are not the same as the graphene ones, leading for instance a short distance between $\mathbf{M} - \mathbf{K}$ points on brick lattice than in graphene, but in general the qualitative shape of both spectra are equivalent. Analyzing the role of the nonzero overlap parameter into the energy spectrum and DOS shown in Figs. 2.4(c) and 2.5(b), one can verify, similarly to the previous discussed lattice cases here, that $s \neq 0$ leads to a electron-hole symmetry breaking and an unbalance between the amount of positive and negative energy states.

2.6.6 *Brick lattice in second quantization*

The second quantization Hamiltonian for the crystallographic structure of brick lattice can be read as:

$$\hat{\mathcal{H}} = \sum_i \epsilon_A a_i^\dagger a_i + \sum_j \epsilon_B b_j^\dagger b_j + \sum_{i,j} t \left(a_i^\dagger b_j + b_j^\dagger a_i \right), \tag{2.76}$$

where $\epsilon_{A(B)}$ and t are the on-site energy at $A(B)$ sublattice and the NN hopping energy, respectively, as similarly defined in Eq. (2.56). To obtain the energy bands of this crystal structure, one can apply the discrete Fourier transforms (2.32)-(2.33) to write Eq. (2.76) in k-space, such as:

$$\hat{\mathcal{H}} = \sum_{\mathbf{k}} [\epsilon_0 \left(a_{\mathbf{k}}^\dagger a_{\mathbf{k}} + b_{\mathbf{k}}^\dagger b_{\mathbf{k}} \right) + t \left(a_{\mathbf{k}}^\dagger f(\mathbf{k}) b_{\mathbf{k}} + b_{\mathbf{k}}^\dagger f(\mathbf{k})^* a_{\mathbf{k}} \right)], \tag{2.77}$$

where we assumed $\epsilon_A = \epsilon_B = \epsilon_0$. $f(\mathbf{k})$ is the geometric structure factor given by:

$$f(\mathbf{k}) = \left[e^{ik_x a} + 2\cos(k_y a)\right]. \tag{2.78}$$

Thus, Eq. (2.77) can be rewritten as:

$$\hat{\mathcal{H}} = \sum_{\mathbf{k}} \langle \Psi_{\mathbf{k}} | \mathcal{H} | \Psi_{\mathbf{k}} \rangle, \tag{2.79}$$

and the energy bands is obtained by diagonalizing $\mathcal{H}$ in Eq. (2.79), resulting the following expression:

$$E_{\pm}(\mathbf{k}) = \epsilon_0 \pm t\sqrt{3 + 2\cos(2k_y a) + 4\cos(k_y a)\cos(k_x a)}, \tag{2.80}$$

with the energy spectrum being depicted in Figs. 2.4(c) and 2.5(b).

2.6.7 *Graphene in first quantization*

After discussed in Subsection 2.6.5 the brick lattice, a topological equivalent lattice to graphene, let us now calculate the energy bands of the honeycomb lattice structure describing a monolayer graphite, *i.e.* a 2D crystal named graphene, by means the first and second quantization formalism. The honeycomb structure of graphene is not a Bravais lattice. However, it can be described as two interpenetrating triangular Bravais sublattices, namely: A and B sublattices, as seen in Fig. 2.1(e), *i.e.* it has two sites (A and B) per unit cell. Each carbon atom of sublattice A (B) has three NN carbon atoms of sublattice B (A). The NNN sites of a carbon atom of a given sublattice, in turn, are six carbon atoms of the same sublattice. The hopping parameter between NN sites is approximately an order of magnitude greater than that between NNN sites[1]. In that sense, we can safely neglect the interactions beyond NNN sites. The primitive vectors of graphene real lattice are $\mathbf{a}_1 = (3a/2, \sqrt{3}a/2)$ and $\mathbf{a}_2 = (3a/2, -\sqrt{3}a/2)$, so that the primitive vectors of the reciprocal lattice, shown in Fig. 2.2(e), are $\mathbf{b}_1 = [2\pi/(3a), 2\pi\sqrt{3}/(3a)]$ and $\mathbf{b}_2 = [2\pi/(3a), -2\pi\sqrt{3}/(3a)]$. The first Brillouin zone [highlighted by the yellow region in Fig. 2.2(e)] is a hexagon limited by $\mathbf{K}_1 = [2\pi/(3a), 2\pi/(3\sqrt{3}a)]$, $\mathbf{K}_2 = [2\pi/(3a), -2\pi/(3\sqrt{3}a)]$, $\mathbf{K}_3 = [0, -4\pi/(3\sqrt{3}a)]$, $\mathbf{K}_4 = [-2\pi/(3a), -2\pi/(3\sqrt{3}a)]$, $\mathbf{K}_5 = [-2\pi/(3a), 2\pi/(3\sqrt{3}a)]$, and $\mathbf{K}_6 = [0, 4\pi/(3\sqrt{3}a)]$. Of these six points, only two are not equivalent, and are called Dirac points. Thus, the Bloch function consisting of A and B sites is written as:

$$\Phi_j(\mathbf{r}, \mathbf{k}) = \frac{1}{\sqrt{N}} \sum_{\mathbf{R}_\alpha} e^{i\mathbf{k}\cdot\mathbf{R}_\alpha} \varphi_j(\mathbf{r} - \mathbf{R}_\alpha), \ \alpha = (A, B). \tag{2.81}$$

The transfer integral and overlap matrices are given by:

$$\mathcal{H} = \begin{pmatrix} \mathcal{H}_{AA} & \mathcal{H}_{AB} \\ \mathcal{H}_{BA} & \mathcal{H}_{BB} \end{pmatrix}, \text{ and } \mathcal{S} = \begin{pmatrix} \mathcal{S}_{AA} & \mathcal{S}_{AB} \\ \mathcal{S}_{BA} & \mathcal{S}_{BB} \end{pmatrix}, \tag{2.82}$$

with the $\mathcal{H}$ elements being $\mathcal{H}_{AA} = \epsilon_A$, $\mathcal{H}_{BB} = \epsilon_B$, and:

$$\begin{aligned} \mathcal{H}_{AB} &= \frac{1}{N}\left(Nt\sum_{n=1}^{3} e^{i\mathbf{k}\cdot\mathbf{d}_n}\right) \\ &= t\left[e^{ik_x a} + 2e^{-ik_x a/2}\cos(k_y a\sqrt{3}/2)\right] \\ &= \mathcal{H}^*_{BA}, \end{aligned} \tag{2.83}$$

with NN sites localized by the vectors $\mathbf{d}_1 = (a, 0)$, $\mathbf{d}_2 = (-a/2, a\sqrt{3}/2)$ and $\mathbf{d}_3 = (-a/2, -a\sqrt{3}/2)$. Likewise, the overlap matrix elements are $\mathcal{S}_{AA} = 1$, $\mathcal{S}_{BB} = 1$, and:

$$\begin{aligned} \mathcal{S}_{AB} &= \frac{1}{N}\left(Ns\sum_{n=1}^{3} e^{i\mathbf{k}\cdot\mathbf{d}_n}\right) \\ &= s\left[e^{ik_x a} + 2e^{-ik_x a/2}\cos(k_y a\sqrt{3}/2)\right] \\ &= \mathcal{S}^*_{BA}. \end{aligned} \tag{2.84}$$

Since A and B sites are identical carbon atoms, then $\epsilon_A = \epsilon_B = \epsilon_0$, and the secular equation (2.22) for graphene can be written as:

$$\det\begin{bmatrix} \epsilon_0 - E_\pm(\mathbf{k}) & \mathcal{H}_{AB} - E_\pm(\mathbf{k})\mathcal{S}_{AB} \\ \mathcal{H}^*_{AB} - E_\pm(\mathbf{k})\mathcal{S}^*_{AB} & \epsilon_0 - E_\pm(\mathbf{k}) \end{bmatrix} = 0, \tag{2.85}$$

resulting in the following dispersion relation:

$$E_\pm(\mathbf{k}) = \frac{\epsilon_0 \pm |\mathcal{H}_{AB}|}{1 \pm |\mathcal{S}_{AB}|}, \tag{2.86}$$

where:

$$\sqrt{3 + 2\cos\left(\sqrt{3}k_y a\right) + 4\cos\left(\frac{\sqrt{3}k_y a}{2}\right)\cos\left(\frac{3k_x a}{2}\right)} = \frac{|\mathcal{H}_{AB}|}{t} = \frac{|\mathcal{S}_{AB}|}{s}, \tag{2.87}$$

where $E_-(\mathbf{k})$ and $E_+(\mathbf{k})$ refer to the valence and conduction bands of graphene, respectively. By comparing Eqs. (2.74)-(2.75) with Eqs. (2.86)-(2.87), one realizes the strong similarity between the obtained dispersion relations for brick lattice and graphene, respectively, such that these lattices can be mapped one in the other by the following k-space transformation: $\left(k_x^{\mathrm{b}}, k_y^{\mathrm{b}}\right) \longrightarrow \left(3k_x^{\mathrm{g}}/2, \sqrt{3}k_y^{\mathrm{g}}/2\right)$, with the superscripts g and b referring to

brick and graphene lattices. Consequently, the position of the high symmetry points in the reciprocal space is changed by a factor of $\sqrt{3}/2$ and $3/2$ along the y and x directions, respectively, with respect to the graphene case, as discussed in Subsection 2.6.5, and the energy spectrum of the brick lattice looks anisotropic whereas the graphene bands are isotropic [see contour plots shown in Figs. 2.4(c) and 2.4(d)]. The graphene energy spectrum is shown in Fig. 2.4(d) along the $\mathbf{\Gamma}-\mathbf{M}-\mathbf{K}-\mathbf{\Gamma}$-path, as illustrated by the dashed black line in the inset of the contour plot on the right panel of Fig. 2.4(d). Note that there are six points where conduction and valence bands touch (see red spots in the contour plot), of these six points only two are non-equivalent, which are called as Dirac points ($\mathbf{K}$ and $\mathbf{K}'$). This gapless band structure feature of graphene leads to its characterization as a semimetal. Low-energy charge carriers in graphene behave like massless Dirac fermions near the Fermi level[61], where the energy-wavevector dispersion relationship is linear, *i.e.* $E(k) \propto k$. That is demonstrated by expanding the TB Hamiltonian around the Dirac points[1], obtaining a continuum Hamiltonian within the long-wavelength approximation. As before, the nonzero overlap parameter causes electron-hole symmetry breaking on energy spectrum and an energy unbalance in the DOS with respect to zero energy.

2.6.8 *Graphene in second quantization*

The procedure below is very similar to the one described in Subsection 2.6.6 for brick lattice, due to the topological equivalence between the graphene and brick lattices. The Hamiltonian of graphene in second quantization is the same as Eq. (2.76), such as:

$$\hat{\mathcal{H}} = \sum_i \epsilon_A a_i^\dagger a_i + \sum_j \epsilon_B b_j^\dagger b_j + \sum_{i,j} t\left(a_i^\dagger b_j + b_j^\dagger a_i\right), \tag{2.88}$$

where ϵ_A, ϵ_B and t have the same definitions as Eq. (2.56), refering to the on-site energies in the sublattices A and B, and the NN hopping energy between $A-B$ sublattices, respectively. To obtain the energy bands of graphene, we can apply the discrete Fourier transforms (2.32)-(2.33) to rewrite $\hat{\mathcal{H}}$ of Eq. (2.88) as:

$$\hat{\mathcal{H}} = \sum_{\mathbf{k}} [a_{\mathbf{k}}^\dagger \epsilon_0 a_{\mathbf{k}} + b_{\mathbf{k}}^\dagger \epsilon_0 b_{\mathbf{k}} + a_{\mathbf{k}}^\dagger t f(\mathbf{k}) b_{\mathbf{k}} + b_{\mathbf{k}}^\dagger t f(\mathbf{k})^* a_{\mathbf{k}}], \tag{2.89}$$

where it was taken $\epsilon_A = \epsilon_B = \epsilon_0$. The geometric structure factor $f(\mathbf{k}) = \sum_{n=1}^{3} e^{i\mathbf{k}\cdot\mathbf{d}_n}$ can be explicitly written as:

$$f(\mathbf{k}) = \left[e^{ik_x a} + 2e^{-ik_x a/2}\cos(k_y a\sqrt{3}/2)\right]. \tag{2.90}$$

In matrix format, Eq. (2.89) reads as:

$$\begin{aligned}\hat{\mathcal{H}} &= \sum_{\mathbf{k}} \begin{bmatrix} a_{\mathbf{k}}^{\dagger} & b_{\mathbf{k}}^{\dagger} \end{bmatrix} \begin{bmatrix} \epsilon_0 & tf(\mathbf{k}) \\ tf(\mathbf{k})^* & \epsilon_0 \end{bmatrix} \begin{bmatrix} a_{\mathbf{k}} \\ b_{\mathbf{k}} \end{bmatrix} \\ &= \sum_{\mathbf{k}} \langle \Psi_{\mathbf{k}} | \mathcal{H} | \Psi_{\mathbf{k}} \rangle. \end{aligned} \tag{2.91}$$

Note that the wavefunction $|\Psi\rangle = [\Psi_A \quad \Psi_B]^T$ is a two-component pseudospinor, *i.e.* a 1 $\times$ 2 column matrix, where $\Psi_{A(B)}$ are the envelop functions associated with the electron probabilities in $A(B)$ sublattices. Diagonalizing $\mathcal{H}$ in Eq. (2.91), one obtains the graphene dispersion relation:

$$E_{\pm}(\mathbf{k}) = \epsilon_0 \pm t\sqrt{3 + 2\cos\left(\sqrt{3}k_y a\right) + 4\cos\left(\frac{\sqrt{3}k_y a}{2}\right)\cos\left(\frac{3k_x a}{2}\right)}, \tag{2.92}$$

depicted in Fig. 2.4(d) and discussed in the previous Subsection 2.6.7.

2.6.9 *τ_3-lattice in first quantization*

Starting from the honeycomb lattice with two sites (A and B) per unit cell, the τ_3-lattice or dice lattice[62] is obtained by connecting additional (C) sites at the center of each hexagon to the B sites [see Fig. 2.1(g)]. The τ_3-lattice is thus a triangular Bravais lattice with three sites per unit cell, *i.e.* it can be described as three interpenetrating triangular Bravais sublattices, namely: A, B and C sublattices. Each site of A (B) sublattice has three NN sites of B (A) sublattice, and each site of B (C) sublattice has three NN sites of C (B) sublattice. The hopping between A and C sites is disregarded because they are not connected. The primitive vectors of the real lattice are the same as the ones for graphene: $\mathbf{a}_1 = (3a/2, \sqrt{3}a/2)$ and $\mathbf{a}_2 = (3a/2, -\sqrt{3}a/2)$, so that the primitive vectors of the reciprocal lattice, shown in Fig. 2.2(e), are $\mathbf{b}_1 = [2\pi/(3a), 2\pi\sqrt{3}/(3a)]$ and $\mathbf{b}_2 = [2\pi/(3a), -2\pi\sqrt{3}/(3a)]$. The first Brillouin zone is equal to that of graphene discussed in Subsection 2.6.7 [see Fig. 2.2(e)]. Thus, the Bloch function consisting of A, B and C sites is written as:

$$\Phi_j(\mathbf{r}, \mathbf{k}) = \frac{1}{\sqrt{N}} \sum_{\mathbf{R}_\alpha} e^{i\mathbf{k}\cdot\mathbf{R}_\alpha} \varphi_j(\mathbf{r} - \mathbf{R}_\alpha), \ \alpha = (A, B, C). \tag{2.93}$$

So that the transfer integral and overlap matrices are given by:

$$\mathcal{H} = \begin{pmatrix} \mathcal{H}_{AA} & \mathcal{H}_{AB} & \mathcal{H}_{AC} \\ \mathcal{H}_{BA} & \mathcal{H}_{BB} & \mathcal{H}_{BC} \\ \mathcal{H}_{CA} & \mathcal{H}_{CB} & \mathcal{H}_{CC} \end{pmatrix}, \; \mathcal{S} = \begin{pmatrix} \mathcal{S}_{AA} & \mathcal{S}_{AB} & \mathcal{S}_{AC} \\ \mathcal{S}_{BA} & \mathcal{S}_{BB} & \mathcal{S}_{BC} \\ \mathcal{S}_{CA} & \mathcal{S}_{CB} & \mathcal{S}_{CC} \end{pmatrix}, \tag{2.94}$$

where the transfer integral matrix elements are $\mathcal{H}_{AA} = \epsilon_A$, $\mathcal{H}_{BB} = \epsilon_B$, $\mathcal{H}_{CC} = \epsilon_C$, $\mathcal{H}_{BC} = \mathcal{H}_{AB}$, $\mathcal{H}_{CB} = \mathcal{H}^*_{AB}$, and:

$$\begin{aligned} \mathcal{H}_{AB} &= \frac{1}{N}\left(Nt\sum_{n=1}^{3} e^{i\mathbf{k}\cdot\mathbf{d}_n}\right) \\ &= t\left[e^{ik_x a} + 2e^{-ik_x a/2}\cos(k_y a\sqrt{3}/2)\right] \\ &= \mathcal{H}^*_{BA}, \end{aligned} \tag{2.95}$$

with NN sites being localized by the vectors $\mathbf{d}_1 = (a, 0)$, $\mathbf{d}_2 = (-a/2, a\sqrt{3}/2)$ and $\mathbf{d}_3 = (-a/2, -a\sqrt{3}/2)$. Likewise, the overlap matrix elements are $\mathcal{S}_{AA} = 1$, $\mathcal{S}_{BB} = 1$, $\mathcal{S}_{CC} = 1$, $\mathcal{S}_{BC} = \mathcal{S}_{AB}$, $\mathcal{S}_{CB} = \mathcal{S}^*_{AB}$, and:

$$\begin{aligned} \mathcal{S}_{AB} &= \frac{1}{N}\left(Ns\sum_{n=1}^{3} e^{i\mathbf{k}\cdot\mathbf{d}_n}\right) \\ &= s\left[e^{ik_x a} + 2e^{-ik_x a/2}\cos(k_y a\sqrt{3}/2)\right] \\ &= \mathcal{S}^*_{BA}. \end{aligned} \tag{2.96}$$

For simplicity, let us admit that $\epsilon_A = \epsilon_B = \epsilon_C = \epsilon_0$. Therefore, the secular equation (2.22) with the use of the transfer integral and overlap matrices given by Eqs. (2.95) and (2.96), results in:

$$\det\begin{bmatrix} \epsilon_0 - E_i(\mathbf{k}) & \mathcal{H}_{AB} - E_i(\mathbf{k})\mathcal{S}_{AB} & 0 \\ \mathcal{H}^*_{AB} - E_i(\mathbf{k})\mathcal{S}^*_{AB} & \epsilon_0 - E_i(\mathbf{k}) & \mathcal{H}_{AB} - E_i(\mathbf{k})\mathcal{S}_{AB} \\ 0 & \mathcal{H}^*_{AB} - E_i(\mathbf{k})\mathcal{S}^*_{AB} & \epsilon_0 - E_i(\mathbf{k}) \end{bmatrix} = 0, \tag{2.97}$$

whose solution is given by:

$$E_0 = 0, \tag{2.98}$$

$$E_\pm(\mathbf{k}) = \frac{\epsilon_0 \pm \sqrt{2}|\mathcal{H}_{AB}|}{1 \pm \sqrt{2}|\mathcal{S}_{AB}|}, \tag{2.99}$$

where:

$$\sqrt{3 + 2\cos\left(\sqrt{3}k_y a\right) + 4\cos\left(\frac{\sqrt{3}k_y a}{2}\right)\cos\left(\frac{3k_x a}{2}\right)} = \frac{|\mathcal{H}_{AB}|}{t} = \frac{|\mathcal{S}_{AB}|}{s}. \tag{2.100}$$

Since τ_3-lattice consists of a crystallographic structure with three sites per unit cell, its energy spectrum is composed by three energy bands: $E_+(\mathbf{k})$, E_0 and $E_-(\mathbf{k})$, referring to the bottom, middle and top bands, respectively. Note that the terms $|\mathcal{H}_{AB}|/t$ and $|\mathcal{S}_{AB}|/s$ in Eq. (2.87) for graphene and in Eq. (2.100) for τ_3-lattice are exactly the same, whereas the $E_\pm(\mathbf{k})$ bands for graphene in Eq. (2.86) and for τ_3-lattice in Eq. (2.99) differ by the presence of a $\sqrt{2}$ term multiplying $|\mathcal{H}_{AB}|$ in the numerator and multiplying $|\mathcal{S}_{AB}|$ in the denominator. In additional to the two bands $[E_\pm(\mathbf{k})]$ similar to the graphene ones, the particularity of the τ_3-lattice energy spectrum is the flat band $E_0 = 0$. Fig. 2.4(e) shows the energy spectrum and DOS of τ_3-lattice along the same k-space direction as in the graphene case to a better comparison between them, and as also illustrated by the dashed black line in the inset of the contour plot in the right panel of Fig. 2.4(e). As in graphene, there are six points where the valence and conduction bands touch, which are triply degenerate due to the presence of the flat band. Owing this non-dispersive band, the DOS for τ_3-lattice exhibits an extra peak at $E = 0$ in comparison to graphene that has two peaks associated with the van Hove singularities. Furthermore, again one can realize that the nonzero overlap parameter causes electron-hole symmetry breaking and the energy spectrum seems to be shifted up.

2.6.10 *τ_3-lattice in second quantization*

The Hamiltonian of τ_3-lattice in second quantization can be written as:

$$\begin{aligned}\hat{\mathcal{H}} &= \sum_i \epsilon_A a_i^\dagger a_i + \sum_j \epsilon_B b_j^\dagger b_j + \sum_k \epsilon_C c_k^\dagger c_k \\ &+ \sum_{i,j} t\left(b_j^\dagger a_i + a_i^\dagger b_j\right) + \sum_{j,k} t\left(b_j^\dagger c_k + c_k^\dagger b_j\right), \end{aligned} \tag{2.101}$$

where ϵ_A, ϵ_B, and ϵ_C represent the on-site energies on sites of type A, B and C, respectively. t is defined as the hopping parameter between NN sites $A-B$ and $B-C$. To obtain the energy bands of τ_3-lattice, we repeat the same procedure done for the previous investigated lattices, applying the discrete Fourier transforms (2.32)-(2.33) and taking $\epsilon_A = \epsilon_B = \epsilon_C = \epsilon_0$ to rewrite Eq. (2.101) as:

$$\begin{aligned}\hat{\mathcal{H}} &= \sum_{\mathbf{k}} [a_{\mathbf{k}}^\dagger \epsilon_0 a_{\mathbf{k}} + b_{\mathbf{k}}^\dagger \epsilon_0 b_{\mathbf{k}} + c_{\mathbf{k}}^\dagger \epsilon_0 c_{\mathbf{k}} + a_{\mathbf{k}}^\dagger t f(\mathbf{k}) b_{\mathbf{k}} \\ &+ b_{\mathbf{k}}^\dagger t f(\mathbf{k})^* a_{\mathbf{k}} + b_{\mathbf{k}}^\dagger t f(\mathbf{k}) c_{\mathbf{k}} + c_{\mathbf{k}}^\dagger t f(\mathbf{k})^* b_{\mathbf{k}}], \end{aligned} \tag{2.102}$$

with the geometric structure factor being $f(\mathbf{k}) = \sum_{n=1}^{3} e^{i\mathbf{k}\cdot\mathbf{d}_n}$ or, explicitly:

$$f(\mathbf{k}) = \left[e^{ik_x a} + 2e^{-ik_x a/2}\cos(k_y a\sqrt{3}/2)\right]. \tag{2.103}$$

Rewriting Eq. (2.102) in a matrix form, one gets:

$$\begin{aligned}\hat{\mathcal{H}} &= \sum_{\mathbf{k}} \begin{bmatrix} a_{\mathbf{k}}^\dagger & b_{\mathbf{k}}^\dagger & c_{\mathbf{k}}^\dagger \end{bmatrix} \begin{bmatrix} \epsilon_0 & tf(\mathbf{k}) & 0 \\ tf(\mathbf{k})^* & \epsilon_0 & tf(\mathbf{k}) \\ 0 & tf(\mathbf{k})^* & \epsilon_0 \end{bmatrix} \begin{bmatrix} a_{\mathbf{k}} \\ b_{\mathbf{k}} \\ c_{\mathbf{k}} \end{bmatrix} \\ &= \sum_{\mathbf{k}} \langle \Psi_{\mathbf{k}} | \mathcal{H} | \Psi_{\mathbf{k}} \rangle. \end{aligned} \tag{2.104}$$

The corresponding energy bands of τ_3-lattice are calculated by diagonalizing $\mathcal{H}$ in Eq. (2.104) [see Fig. 2.4(e)], resulting in:

$$E_0 = 0, \tag{2.105}$$

$$E_{\pm}(\mathbf{k}) = \epsilon_0 \pm t\sqrt{3 + 2\cos\left(\sqrt{3}k_y a\right) + 4\cos\left(\frac{\sqrt{3}k_y a}{2}\right)\cos\left(\frac{3k_x a}{2}\right)}. \tag{2.106}$$

2.7 Conclusion

We have shown how the TB model can be applied to the study of the electronic band structure of several periodic structures. The model can be applied to a wide range of systems, such as molecules, polymers, nanotubes and 2D and 3D crystals, and we presented calculations for the energy spectrum for 2D systems with one, two and three bands of energy. A nonzero overlap parameter showed to cause electron-hole symmetry breaking of the energy spectrum and an energetic unbalance in the DOS with respect to zero energy.

Furthermore, the results highlighted the fact that many of the distinct properties of these systems, such as the linear dispersion of electrons close to the Fermi level in graphene and the flat band of τ_3-lattice are mainly a consequence of the geometry of the lattice and the number of non-equivalent sublattices. However, these spectra can be significantly modified by the inclusion of additional effects such as electron-electron interaction, which can be introduced in a first approximation by the addition of a mean-field Hubbard term in the Hamiltonian. Another possible addition to the model is the inclusion of the spin-orbit coupling, which can lead to the formation of a gap in the spectrum. Moreover, the model can be easily modified to deal with the presence of surfaces and edges. In

that case, as the system loses translation symmetry along one direction, and also due to possible on-site energies or hopping modifications due the absence of bonds, the model may give rise to surface or edge localized states. These states have been intensively investigated in connection with topological effects in materials. A further modification is the addition of lattice defects or impurities, which cause the formation of non-propagating localized states. Each addition to the model increases the complexity of the calculations necessary for obtaining the spectra, which can then be tackled by numerical approaches.

3 CURRENT MODULATION IN GRAPHENE P-N JUNCTIONS WITH EXTERNAL FIELDS

In this Chapter, we describe a proposal for a graphene-based nanostructure that modulates electric current even in the absence of a gap in the band structure. The device consists of a graphene p-n junction that acts as a Veselago lens that focuses ballistic electrons on the output lead. Applying external (electric and magnetic) fields changes the position of the output focus, reducing the transmission. Such a device can be applied to low power field effect transistors, which can benefit from graphene's high electronic mobility.

3.1 Introduction

The production of high-quality samples of graphene has allowed the investigation of charge transport in the ballistic regime at length scales much larger than in other materials[11]. This fact has permitted the observation of effects such as Klein tunneling[19, 20, 63] and Fabry-Pérot oscillations[64–66] that point towards a striking similarity between light propagation in waveguides and electronic transport in graphene. Due to Klein tunneling, *i.e.* the perfect transmission through potential barriers, the confinement of charge carriers in graphene can become a challenge. That fact limits the use of graphene on logical device applications, due to the fact that one cannot in general "turn off" the current. Some ways to circumvent that limitation are the use of graphene nanoribbons[30, 67–72], in which the geometry of the sample induces a lateral confinement that can create a gap in the band structure. Other possibilities involve the use of graphene bilayers, or the application of strain which can also give rise to a band gap[1].

It has been recently shown that an additional mechanism for controlling the propagation of electrons in graphene without the creation of a band gap can be developed in analogy with an optical counterpart, namely, phase modulation[73]. Optical phase modulators make use of the electro-optical effect, in which a voltage can change the

refractive index of a given medium. In the case of graphene, a similar effect can be obtained by means of p-n junctions[2, 25, 74, 75]. Another similarity between electronic transport in graphene and optics is the negative refraction of electrons incident on a p-n junction[25, 75]. In photonic systems, a medium with a negative refraction index would allow the development of devices such as superlenses which can focus light beams beyond the diffraction limit[76]. The prospect of an optical superlens was first raised by V. G. Veselago[24], who showed that in conditions where the electric and magnetic responses are negative, the group and phase velocities presented opposite directions. For electrons in graphene, theoretical[2, 63, 75, 77–84] and experimental works[21, 85–88] have shown this effect, which can also be exploited to focus electron beams with high precision.

The ability to focus an electron beam on a small region of a graphene sample suggests that a Veselago lens may allow the development of a current switch that can be operated by properly applying an external (electric or magnetic) field. Thus, in this Chapter we theoretically investigate a graphene-based device in which electrons emitted from an input lead are focused by a p-n junction on an output lead, so that the overall transmission amplitude and therefore the conductance of the device are increased. Applying an in-plane electric field or a perpendicular magnetic field acts to shift the position of the focal point, increasing reflectance and thus significantly decreasing transmission. The device bears some resemblance to the optical technique for imaging fluids known as Schlieren photography[89], in which light from a collimated sourced is focused on a knife edge that blocks half the incoming light, such that small changes in fluid density result in large variations in image contrast.

This Chapter is organized as follows. In Section 3.2, we present the theoretical framework used to describe the transport properties of the graphene-based current modulator as well as its operating characteristics. In Section 3.3, we discuss the numerical results and analyze it within a semiclassical picture. Finally, in Section 3.4, we summarize our main findings.

3.2 Model

Before describing the proposed nanostructure, let us briefly recall the propagation of an electronic plane wave through a potential step in graphene in order to elucidate how a graphene p-n junction acts as focusing lens for electrons[2, 25, 75].

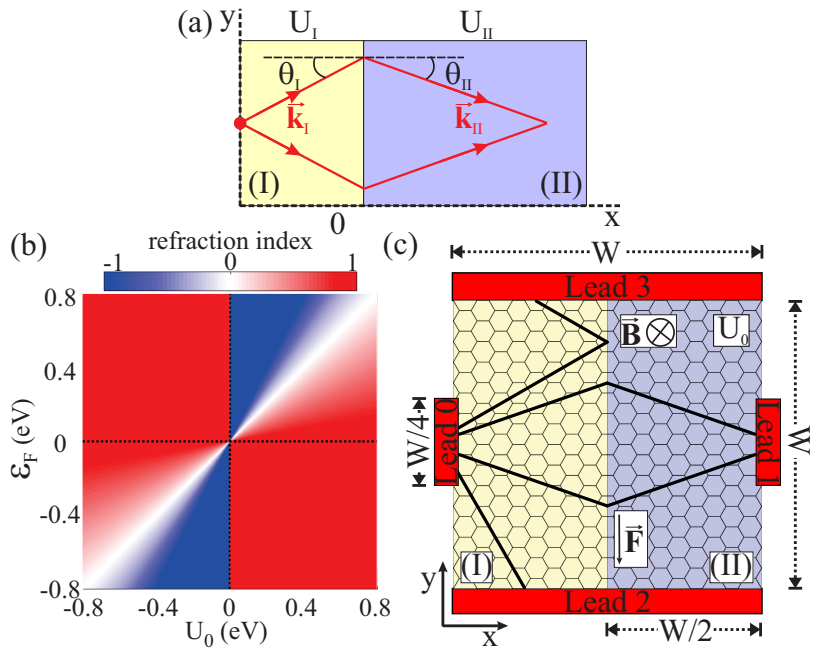

Figure 3.1: (a) Sketch of focusing effect of electrons in graphene across a potential step due to negative refraction index. In region I (II) is applied a bias potential U_I (U_{II}). The incident and transmitted electronic waves have momentum $\mathbf{k}_I$ and $\mathbf{k}_{II}$ and angles θ_I and θ_{II} formed with x-axis, respectively. (b) Refraction index, given by Eq. (3.1), as a function of the electrostatic potential strength U_0 and Fermi energy ε_F, taking $U_I = 0$ and $U_{II} = U_0$ for the bias potential in each junction region. (c) Schematic representation of the proposed current modulator. In the region II at the right-half of the sample, a bias potential with amplitude U_0, an in-plane electric field $\mathbf{F}$ and a perpendicular magnetic field are inserted. The electrons are injected into the scattering region by lead 0 in region I and can be collected by leads 1, 2 or 3. The square system length is W and the lead width is assumed as $W/4$.

Let us consider the system shown in Fig. 3.1(a) with different charge densities on regions I ($x < 0$) and II ($x > 0$) induced by two gates that shift the Dirac cones by U_I and by U_{II}, respectively. An electron approaching the junction from region I reaches the interface with an incident angle θ_I and is transmitted to region II with a transmission angle θ_{II}, where $\mathbf{k}_I$ and $\mathbf{k}_{II}$ are the respective wavevectors. Since the system has translational symmetry along the y-direction, the transverse momentum (k_y) is conserved at the interface, such that $|\mathbf{k}_I| \sin\theta_I = |\mathbf{k}_{II}| \sin\theta_{II}$. From the Dirac equation for biased graphene, we have the shifted dispersion relation $\varepsilon_F(k) = s\hbar v_F k + U_i$, where $s = +/-$ correspond to electrons/holes, respectively, i denotes the region index I and II, and v_F is the Fermi velocity. Connecting both equations, it implies in a similar Snell's law to ray optics where the energies here play the role of the refractive index:

$$n = \frac{\sin\theta_I}{\sin\theta_{II}} = \frac{k_{II}}{k_I} = \frac{\varepsilon_F - U_{II}}{\varepsilon_F - U_I}. \tag{3.1}$$

Note that when $(\varepsilon_F - U_{II})(\varepsilon_F - U_I) < 0$, or equivalently when θ_I and θ_{II} have opposite signs, one obtains a negative refractive index impling that the sign of the tangential momentum component of the propagating electron changes while the normal component remains the same. As a consequence, the incident electrons will converge into a focal point on region II, as it happens in Veselago lens medium[2, 25, 75]. The refractive index is shown in Fig. 3.1(b) as a function of the electrostatic potential strength U_0 and Fermi energy ε_F, for the system parameter ranges investigated along this Chapter and taking $U_I = 0$ and $U_{II} = U_0$ for the bias potential in regions I and II, respectively. It is easy to see from Eq. (3.1) for $U_I = 0$ and $U_{II} = U_0$ that: the negative (positive) refraction index $n < 0$ ($n > 0$) happens when $U_0 > \varepsilon_F$ ($U_0 < \varepsilon_F$) such that the electron semiclassical trajectories are expected to (converge) diverge with the p-n junction interface acting as (convex) concave lens, while for $U_0 = \varepsilon_F$ one gets the $n = 0$ situation where the transmission angle is zero and the electrons are perfect collimated. The blue, red and white colors denote $n < 0$, $n > 0$ and $n = 0$ cases in Fig. 3.1(b). Therefore, there is a direct analogy between propagated charge carriers through graphene p-n junction and the light focusing observed in Veselago lens due to negative refraction index medium.

Motivated by this negative refractive effect on a graphene p-n junction, we propose the nanostructure schematically illustrated in Fig. 3.1(c) as a current modulator, as will be justified by the results discussed in Section 3.3. For this, we investigate the transmission of these electrons through an abrupt biased graphene p-n junction, *i.e.* graphene in the presence of a potential step created by electrostatic gates, and in addition to that we include an in-plane electric field and a perpendicular magnetic field to tune the electron focus and consequently to modulate the conductance. The energy spectrum for this system was analytically studied in detail in Ref. [90], the transmission probability and conductance in the absence of magnetic field for graphene p-n junction has been shown in Refs. [2, 63, 74, 77, 80, 81, 84, 85], and in the presence of magnetic field has been reported in Refs. [21, 77–79, 82, 83, 88]. Although in a more realistic experimental set-up the p-n junction has a finite width, it has been shown[75] that smooth graphene p-n junctions exhibit negative refraction and lensing similar to a sharp junction, as considered in the current Chapter.

The system consists of a square graphene sample with length W. The in-plane electric and magnetic fields are just applied in region II, *i.e.* on the right-half of the

sample ($x > 0$). For the sake of simplicity, we consider only nanoribbons with armchair-type edges, although one expects the results are not qualitatively distinct from the zigzag case, since we are not concerned with edge states for the transport properties. Indeed, it has been shown in Ref. [74] that zigzag interface and armchair interface graphene p-n junction exhibits qualitatively similar results. Moreover, the actual sample studied throughout the Chapter is large enough such that the qualitative behaviors here reported and the proof-of-concept of the proposed system as a current modulator, which are the main goals of this Chapter, would still hold, since they are based on more fundamental physical properties regarding the negative refractive effect of the proposed structure, as we discuss bellow.

Four ballistic leads are added to the scattering region with two of them parallel to the x-axis (leads 2 and 3 that cover the entire top and bottom boundaries), while the other two leads are perpendicular to that direction (leads 0 and 1 that are narrow with respect to the total system size in order to represent a point source and a focal point, respectively). In this configuration, the electrons are injected into the scattering region by lead 0 (left side of the sample) and can be collected by leads 1, 2 or 3, as shown in Fig. 3.1(c). Leads 2 and 3 are included to prevent interference from electrons that do not reach the region II of Fig. 3.1(c) and due to unintended reflections from the edges of the sample.

In order to show that the proposed system works as a current modulator, we shall calculate and discuss the probability current density and conductance as a function of several parameters, such as: Fermi energy, potential step height, magnetic and electric field amplitudes, and different widths of the scattering region. Our theoretical framework is based on the Landauer-Büttiker formalism where the transport properties are computed within the wave function approach[31] and by using the tight-binding model within the nearest-neighbor approximation to describe the charge carriers in graphene. The corresponding Hamiltonian can be written as:

$$H_{TB} = \sum_i (\varepsilon_i + U_i + F_i) c_i^\dagger c_i + \sum_{i \neq j} (\tau_{ij} c_i^\dagger c_j + \text{H.c.}), \tag{3.2}$$

where c_i ($c_i^\dagger$) annihilates (creates) an electron in site i with on-site energy ε_i. $\tau_{ij} = t = -2.8$ eV is the nearest-neighbor hopping parameter between the atoms in the A and B sublattices. U_i and F_i are on-site potentials that are used here to simulate the p-n junction

and to apply the in-plane electric field, respectively. The gate potential U_i consists of a single step at $x = 0$: $U_i = U_0\Theta(x)$, where $\Theta(x)$ is the Heaviside step function and U_0 is the potential height. The in-plane electric field is applied along the y-direction, *i.e.* $\mathbf{F} = (0, -F_y, 0)$, and is perpendicular to the propagation direction between leads 0 and 1. The effect of an external magnetic field is incorporated in the tight-binding model via the Peierls substitution, as:

$$\tau_{ij} \to \tau_{ij} \exp\left(i\frac{e}{\hbar}\int_j^i \mathbf{A}\cdot d\mathbf{l}\right), \tag{3.3}$$

where $\mathbf{A}$ is the vector potential associated with an external magnetic field $\mathbf{B}$, that we assume here to be perpendicular to the graphene flake, $\mathbf{B} = B\hat{z}$.

All the transport calculations presented in this Chapter were performed using the KWANT code, which is a free (open source) Python package for numerical calculations on tight-binding models[31].

3.3 Results

In order to verify that the system works as a Veselago lens, we first calculate the probability current density as shown in Fig. 3.2 for the graphene p-n junction system sketched in Fig. 3.1(c) and show that the focal point moves by applying external fields: perpendicular magnetic field in Figs. 3.2(b)-3.2(c) and in-plane electric field in Figs. 3.2(d)-3.2(e). Without loss of generality, we consider a symmetric junction with respect to the scattering region size such that the injected and collecting leads are placed $W/2$ away from the interface at $x = 0$, and the Fermi energy as $\varepsilon_F = U_0/2 = 0.4$ eV. We assume the injected lead to be narrow enough in order to mimic a source point, whereas the collecting lead here for these results was made larger to avoid backscattering and thus a misleading understanding of the lensing process.

For the non-perturbed case [Fig. 3.2(a) for $F_y = 0$ and $B_z = 0$], the propagated wave is focused symmetrically such that the focus spot is at the same height y as the source lead. By applying a perpendicular magnetic field the current density vectors are seen to be deflected (downwards since $\mathbf{B}$ points into the page) due to the Lorentz force, shifting the focal point position, as depicted in Figs. 3.2(b) and 3.2(c) for magnetic field amplitudes $B_z = 0.2$ T and $B_z = 0.4$ T, respectively. By comparing Figs. 3.2(b) and 3.2(c), one can notice the focal position shift is larger the higher the magnetic field amplitude. This

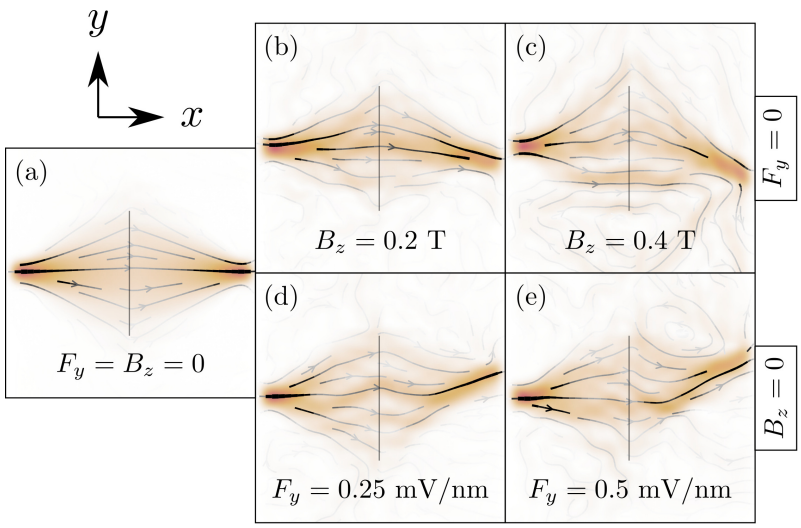

Figure 3.2: Probability current densities for the system shown in Fig. 3.1(c) for (a) the non-perturbed case with $B_z = 0$ and $F_y = 0$, and under the effect of perpendicular magnetic field [with (b) $B_z = 0.2$ T and (c) $B_z = 0.4$ T] and in-plane electric field [with (d) $F_y = 0.25$ mV/nm and (e) $F_y = 0.5$ mV/nm]. Plots are made using a very narrow input and a large output leads in order to mimic a source point and to avoid backscattering when the focus position changes.

can be easily understood by the following semiclassical picture: from Lorentz force $m\mathbf{a} = -e\mathbf{v} \times \mathbf{B}$, where e is the elementary charge, $\mathbf{a}$ and $\mathbf{v}$ are the acceleration and velocity of electron, respectively, and knowing that the cyclotron effective mass depends on the band structure via the derivative of this area in energy[91, 92] such that for an isotropic energy spectrum one has:

$$m = \frac{\hbar^2}{2\pi}\frac{d^2A(\varepsilon)}{d\varepsilon^2}, \tag{3.4}$$

where $A(\varepsilon)$ denotes the k-space area enclosed by a constant energy contour ε, one can find the cyclotron radius as $r_c = |\varepsilon/(ev_F B)|$. This shows that the cyclotron radius is inversely proportional to the magnetic field and therefore the larger $|B|$ the smaller is r_c and consequently the (x,y)-coordinates of the focal point vary more. A similar effect can be achieved when an in-plane electric field is applied in the region II of the system, as shown in Figs. 3.2(d) and 3.2(e) for $\mathbf{F} = (0, -F_y, 0)$ with $F_y = 0.25$ mV/nm and $F_y = 0.5$ mV/nm, respectively, such that the negative charge carriers are pushed upwards and the focal point moved up along y-direction.

In both external electric and magnetic field cases discussed in Fig. 3.2, as high the amplitude of the external field more further away the focal point is from the output lead and consequently a decreasing in the conductance is expected. In order to quantify how the conductance changes due to the external fields, we perform numerical

calculations of the conductance between leads 0 and 1 as a function the electric [Fig. 3.3(a)] and magnetic [Fig. 3.3(b)] field amplitudes by considering the symmetric Veselago lens case that means the focal spot is placed at the same distance from the p-n interface as the injector. It corresponds to $\theta_I = -\theta_{II}$ case, or equivalently the situation where the Fermi energy must be half value of the potential step height, *i.e.* $\varepsilon_F = U_0/2$, that means $n = -1$ in Eq. (3.1). This symmetrical p-n junction implies that the number of electrons injected by lead 0 and captured by lead 1 is the maximum that can be achieved for this setup. The results shown in Fig. 3.3 were obtained for three different sample widths W, viz. 50, 100 and 150 nm, and taking $\varepsilon_F = U_0/2 = 0.4$ eV.

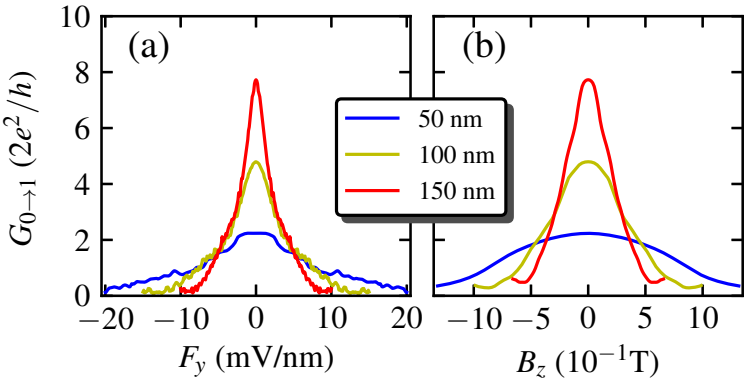

Figure 3.3: Conductance as a function of the electric (a) and magnetic (b) field amplitudes between leads 0 and 1 for sample width (blue curve) $W = 50$ nm, (yellow curve) $W = 100$ nm, and (red curve) $W = 150$ nm. It is taken $\varepsilon_F = U_0/2 = 0.4$ eV, and for panel (a) $B_z = 0$ and for panel (b) $F_y = 0$.

In Fig. 3.3, one can notice that the conductance between leads 0 and 1 is significantly reduced by the application of the external in-plane electric [Fig. 3.3(a)] and perpendicular magnetic [Fig. 3.3(b)] fields, as expected based on the fact that focal spot in region II of the sample is shifted in the y-direction a way from the collector (lead 1). As a consequence, the electron beams are then scattered by the right boundary of the graphene p-n junction and collected by the bottom and top leads 2 and 3, respectively, leading to a current reduction between leads 0 and 1. Furthermore, one can verify from Fig. 3.3 that the external field required to control the conductance depends on the system width W, and the larger the width considered the smaller the external field needed to obtain a significant change on $G_{0\to1}$, as for instance in Fig. 3.3(a) $G_{0\to1} \approx 0$ for $W = 150$ nm with $F_y \approx 10$ mV/mm, for $W = 100$ nm with $F_y \approx 15$ mV/mm, and for $W = 50$ nm with $F_y \approx 20$ mV/mm. Let us now understand this W dependence on the conductance. Note that: (i) for the non-perturbed case with $B_z = 0$ and $F_y = 0$, the conductance is larger the wider the

system, *i.e.* $G_{0\to1}(W = 150\text{ nm}) > G_{0\to1}(W = 100\text{ nm}) > G_{0\to1}(W = 50\text{ nm})$; (ii) due to the finite system along y-direction the sample can be seen as a large armchair nanoribbon with ribbon width W which in turn resembles a potential well in y-direction; and (iii) for graphene nanoribbons[30, 67–70], as the width W increases there are more localized states for a fixed energy range and the energy levels become closer. Therefore in general for larger systems there are more transverse electronic modes available to contribute to transport and thus the conductance is larger the wider the width W. Although the qualitative behavior of conductance as a function of external electric and magnetic fields are similar, in the case of non-zero magnetic field the minimal conductance obtained is larger than the minimal conductance for the electric field case. For instance the minimal conductance in units of $e^2/\hbar$ for $W = 150$ nm and $W = 100$ nm in the presence of electric field [panel (a)] are 0.113 and 0.098, respectively, while for non-zero magnetic field [panel (b)] are 0.483 and 0.284, respectively.

Let us now analyze the influence of the potential step height on the conductance between leads 0 and 1. Fig. 3.4 shows the conductance as function of U_0 for the same three different sample widths described above: [Fig. 3.4(a)] $W = 50$ nm, [Fig. 3.4(b)] $W = 100$ nm, and [Fig. 3.4(c)] $W = 150$ nm, in the absence of any external field (black curve for $B_z = 0$ and $F_y = 0$), and in the presence of an in-plane electric field (magenta curve for $F_y \neq 0$) and an out-of-plane magnetic field (orange curve for $B_z \neq 0$). In particular, for non-zero external field it was assumed the approximated values of the electric and magnetic field amplitudes associated to the minimal conductance shown in Fig. 3.3, such as, *e.g.* for finite electric (magnetic) field and for $W = 50$ nm the value $F_y = 20$ mV/nm ($B_z = 1.5$ T), for $W = 100$ we use $F_y = 15$ mV/nm ($B_z = 1.0$ T) and for $W = 150$ nm, $F_y = 10$ mV/nm ($B_z = 0.5$ T).

One can notice from Fig. 3.4 that the conductance exhibits an asymmetric behavior with respect to ($U_0 = \varepsilon_F$)-axis, *i.e.* there are two different trends: for $U_0 < \varepsilon_F$ and $U_0 > \varepsilon_F$, where it was taken $\varepsilon_F = 0.4$ eV. From Eq. (3.1) and its analysis discussed in Section 3.2, the nature of the two different conductance regimes is related to the different signs of the refraction index, being positive and negative for $U_0 < \varepsilon_F$ and $U_0 > \varepsilon_F$, respectively. In the negative (positive) refraction index regime, one can observe an increase (a decrease) of conductance with the gate potential increase in Fig. 3.4. This, in turn, is related to the fact that the value of the refraction index will dictate the focal spot position,

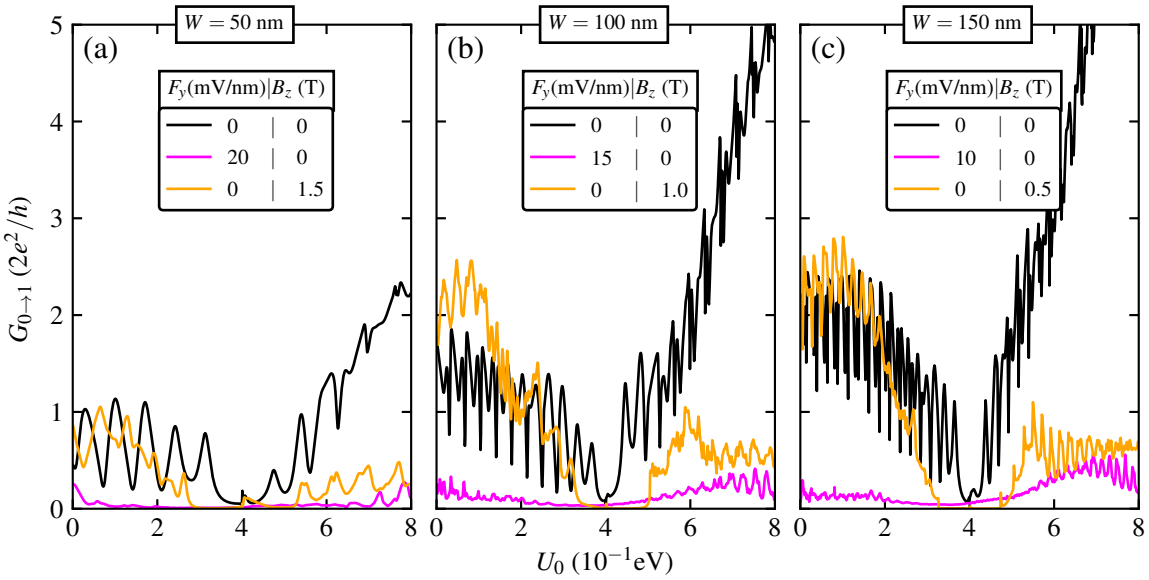

Figure 3.4: Conductance between leads 0 and 1 as a function of the potential step height U_0 in the absence of any external field (black curve for $B_z = 0$ and $F_y = 0$), and in the presence of an in-plane electric field (magenta curve for $F_y \neq 0$) and an out-of-plane magnetic field (orange curve for $B_z \neq 0$). Panels (a), (b) and (c) correspond to sample width $W = 50$ nm, $W = 100$ nm, and $W = 150$ nm, respectively. It is taken $\varepsilon_F = 0.4$ eV.

since depending on its value the electron beams will be perfectly collimated, or converge or diverge after reaching the interface, and therefore a portion of the injected electrons will be captured or not by the output lead and also determinating the conductance amplitude. From Eq. (3.1) and by a simple geometry analisis of electronic trajectory sketched in Fig. 3.1[74], one can predict the x-position of the focal spot, as:

$$x_{focal} = \frac{W}{2}\left|\frac{\tan\theta_I}{\tan\theta_{II}}\right|, \tag{3.5}$$

where the transmitted angle for investigated potential step with $U_I = 0$ and $U_{II} = U_0$ is given by:

$$\theta_{II} = \arcsin\left[\left(\frac{\varepsilon_F}{\varepsilon_F - U_0}\right)\sin\theta_I\right]. \tag{3.6}$$

As expected for the symmetric case, one has $\theta_I = -\theta_{II}$ and thus one can find $x_{focal} = W/2$. From Eqs. (3.5) and (3.6), one can realize that: the position of the focal spot depends on the gate potential value, the Fermi energy and the incident angle; and the transmission increases as x_{focal} approaches the output lead. Moreover, once that we assumed a symmetrical graphene p-n junction, the maximum $G_{0\to1}$ value in the absence of any external field (black curves in Fig. 3.4) is achieved for $U_0 \approx 2\varepsilon_F = 0.8$ eV, *i.e.* for $n = -1$, while for the range $\varepsilon_F < U_0 < 2\varepsilon_F$ one has $-1 < n < 0$ with the focal x-position

not being diametrically opposite to input lead but it will be tending to the symmetric position as n tends to -1, and thus explaining the $G_{0\to1}$ increasing up to its maximum value at $U_0 \approx 2\varepsilon_F$.

In addition, from Fig. 3.4, one can note that although there is a significant reduction in conductance with the application of the in-plane electric field (magenta curves), with the application of the perpendicular magnetic field (orange curves) there is a less significant reduction. Most importantly for our purpose of an efficient device operating on the negative refraction index regime, is that regardless of the sample width or even the kind of the applied external field (electric or magnetic) the conductance $G_{0\to1}$ is reduced. Although not shown, it is easy to see that as the conductance between leads 0 and 1 increases, the conductance between leads 0 and 2 and between leads 0 and 3 decreases proportionally. It is important to emphasize that the interplay between the external magnetic field in region II ($x > 0$) and the bias gate induced by the p-n junction will favor a high conductance for a certain small energy range when $U_0 < \varepsilon_F$ as a consequence of a maximized focusing of the divergent beam due to $n > 0$ and the circular orbit due to $\mathbf{B}$ field, that brings the focal point closer to the output spot[93]. Such behavior can be seen by orange curves in Figs. 3.4(a), 3.4(b) and 3.4(c) for $U_0 \in [0.05, 0.1]$ eV that exhibits conductance peaks higher than those ones for null magnetic field case.

Next, we study the dependence of the conductance on the Fermi energy for a fixed potential step height $U_0 = 0.8$ eV and under the influence of external fields regarding three different sample widths. The results are shown in Fig. 3.5 for the same parameters as in Fig. 3.4.

For $B_z = 0$ and $F_y = 0$ (black curves), a pronounced peak arises in the conductance at the same position $\varepsilon_F = U_0/2 = 0.4$ eV regardless of the sample width [see the same behavior in three panels 3.5(a)-3.5(c)]. This is a direct consequence of the negative refraction induced by the Veselago lens property in graphene p-n junction. Let us examine the symmetric nature of the conductance with respect to the ($\varepsilon_F = U_0/2$)-axis. In the investigated Fermi energy range $0 \leq \varepsilon_F \leq U_0$ in the plots of Fig. 3.5, one has by Eq. (3.1) that $n < 0$. One can split the energy range as follows: for $0 \leq \varepsilon_F \leq U_0/2$, the refractive index is $n \leq -1$, whereas for $U_0/2 < \varepsilon_F \leq U_0$, one has that $-1 < n \leq 0$. It is interesting to mention that for $n < -1$ and $-1 < n \leq 0$ the semiclassical electronic trajectories are caustics, which are the envelope of the classical

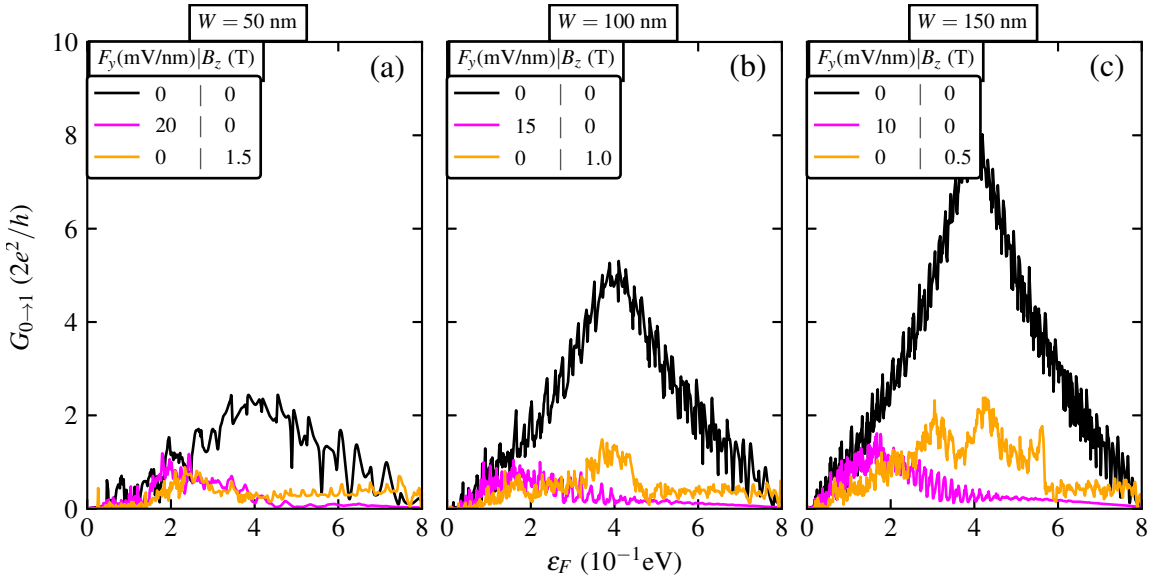

Figure 3.5: Conductance between leads 0 and 1 as a function of the Fermi energy ε_F in the absence of any external field (black curve for $B_z = 0$ and $F_y = 0$), and in the presence of an in-plane electric field (magenta curve for $F_y \neq 0$) and an out-of-plane magnetic field (orange curve for $B_z \neq 0$). Panels (a), (b) and (c) correspond to sample width $W = 50$ nm, $W = 100$ nm, and $W = 150$ nm, respectively. It is taken $U_0 = 0.8$ eV.

trajectories, with cusp points shifted in x-direction for left and the right with respect to the symmetric case where $n = -1$[84]. Thus, based on this classical picture, it is evident that the displacement of the focal spot in x-direction will cause a reduction in the conductance. As discussed previously, the maximum conductance is obtained in the symmetric situation when $\varepsilon_F = U_0/2$ or equivalently when $\theta_I = -\theta_{II}$ and $n = -1$. Thus, for lower or higher Fermi energies than $U_0/2$ the conductance is lower than its maximum value. Other relevant case to analyze is when $\varepsilon_F = U_0$. By replacing $\varepsilon_F = U_0$ in Eq. (3.1), one obtains that $\theta_{II} = 0$, that means the electron beams are perfected collimated in region II. If instead of a finite focal spot, one considers a focal point for the output lead, thus, in this case where $\varepsilon_F = U_0$, just the electrons with normal incidence would be captured by the output lead, explaining the lowest conductance value at $\varepsilon_F = 0.8$ eV in Fig. 3.5. Based on these statements, it suggests that the conductance curve should decrease between the symmetric situation ($\varepsilon_F = U_0/2$) that is a maximum point and the perfected collimation situation ($\varepsilon_F = U_0$) that corresponds to a minimum.

With the application of an in-plane electric field (magenta curves in Fig. 3.5), the conductance is strongly reduced and its maximum is pushed to the energetic range $0 \leq \varepsilon_F \leq U_0/2$, while the conductance is almost zero and unchanged by increasing the Fermi

energy within the range $U_0/2 < \varepsilon_F \leq U_0$. For instance, in Fig. 3.5(c) for $W = 150$ nm, the conductance is reduced of approximately ten times as compared to the zero in-plane electric field case. On the other hand, by applying a perpendicular magnetic field (orange curves in Fig. 3.5) there is a slight reduction in conductance but not so pronounced as for non-zero electric field case. This is in agreement with the discussion made in Fig. 3.4 about the influence and robustness of the electric and magnetic field on the conductance. Moreover, by comparing the orange curves in Figs. 3.5(a), 3.5(b) and 3.5(c), one can see that the region of the pronounced conductance reduction goes to higher energies for larger samples. This is due to the fact that the thinner the nanoribbon, fewer lower energy states will have an orbit that fits in the sample and thus be deflected towards the focus point, since in the presence of a magnetic field the electron beam is bent with a cyclotron radius that is (in)directly proportional to the Fermi energy (the magnitude of the magnetic field $\mathbf{B}$). On the other hand, the electronic orbits for high energy values will be reflected at the edges and interfere themselves, and thus resulting in a reduction of the conductance $G_{0\to1}$.

3.4 Conclusion

We proposed a current modulator-like device model based on the Veselago lensing effect in graphene p-n junction. The operating principle of this device is connected to the fact that Dirac electrons passing through graphene p-n junction at specific energy are transmitted with a negative angle and thus converge on the other sample side at the focal point. This is due to the negative refraction index merged from the energy difference ratio between the Fermi energy and bias potential in the two regions of this junction and therefore the optic-like Dirac electron behavior in a graphene p-n junction is analog of a Veselago lens. We demonstrated that an in-plane electric field or an out-of-plane magnetic field move the electronic focal spot further way from the output lead and consequently tune the current transmission between the input and output leads. For the proof-of-concept that the proposed device can work as a current modulator and for its transport properties quantification, we investigated the behavior of the probability current density and conductance, by using the Landauer-Büttiker formalism within the tight-binding approach, as a function of the electric and magnetic field amplitudes, the Fermi energy, the system size, and the potential step height. Our findings show that the

application of the external fields to this system can reduce significantly its conductance even for low power fields. Finally, we hope that our results and the proposed nanostructure will prove useful for designing graphene-based current modulator like optical devices that works even in the absence of a gap in the graphene band structure and in low power field regime.

4 GATE POTENTIAL-CONTROLLED CURRENT SWITCHING IN GRAPHENE Y-JUNCTIONS

In this Chapter, we investigate the ballistic transport of electrons through three-terminal graphene-based devices. The system consists of a Y-shaped junction formed by three armchair-edged graphene nanoribbons with a rectangular gate potential applied to one of the output branches, whereby current control can be established by the controlling of the refractive index in graphene p-n junctions. Transport properties are obtained by using the Landauer-Büttiker formalism and the tight-binding model within the nearest-neighbor approximation, which allows the calculation of the conductance as function of the Fermi energy, the applied potential, and the system size, as well as the current density. The results demonstrate that the applied electric field can tune the current transmission between the input and two output leads and, consequently, the proposed system acts as a current switch.

4.1 Introduction

Semiconductor materials are widely used in the production of several electronic devices, being the basis of the microelectronics industry. When first introduced, these electronic devices provided advantages in comparison with previous technologies, such as reasonable performance, energy-saving, low cost of manufacturing, compacting electronic components, as well as the possibility of large scale integration. However, the silicon-based semiconductor technology is close to reach its limit in miniaturization[94], which has led many researches to search for alternatives beyond the standard semiconductors to develop novel and more efficient quantum devices.

The past two decades, since the experimental isolation in 2004 by Novoselov *et al.*[8], graphene has been shown to be a promising material due to its exceptional electronic and transport properties and therefore graphene-based structures have been a subject of growing interest of the scientific community. Graphene has peculiar electronic

properties, exhibiting a linear energy dispersion with charge carriers that can be described by the 2D Dirac equation for massless fermions. In particular, unusual behaviors such as: semi-integer quantum Hall effect[61], ballistic electrons propagation[32, 95], and Klein tunneling[19] (a perfect transmission of normally incident electrons through gate potential barriers) are observed in graphene structures. There have been efforts to circumvent the Klein tunneling phenomenon to possibly manufacture a field-effect transistor for logic applications such as manipulation in the energy gap[26] or design new types of circuits[22], that promises to overcome the limitation of the current semiconducting materials. A relevant feature of graphene for technological applications in electronic devices is its ultrahigh electronic mobility that can significantly improve the performance of electronics including various transistors and detectors, providing a performance advantage in comparison to standard semiconductors, as for instance it allows the production of transistors operating in a scale of less than 10 nm, considered the operation limit of silicon-based devices[96, 97].

Quantum transport with phase coherence in low-dimensional multi-terminal structures has been subject of experimental[98–103] and theoretical[43, 104–106] studies. Three-terminals ballistic junctions are well-known examples of ballistic devices[107–112], as for instance, electronic rectifications in Y-shaped carbon nanotubes that have been experimentally[113–115] and theoretically[116] demonstrated, as well as based on graphene junctions[117, 118]. These structures have demonstrated a great potential towards the development of electronic nanodevices with properties such as voltage rectification and frequency multiplication[119], logic gates[120], switches[121], and others[91]. Based on studies that demonstrate the ballistic nature of the electronic transport in graphene nanostructures, we have considered a Y-shaped three-terminal ballistic junction structure made of armchair-edged nanoribbons in order to analyze the electronic transport properties, and to demonstrate its possible application in high-performance switches. The physical system has a rectangular gate potential in the output branch which is applied to obtain steering and collimation of the current. Recently, an experimental study was conducted[122] for a similar three-terminal quantum switch based on tunable Dirac fermion optics and that utilizes explicitly the angle dependence of Klein tunneling to build tunable collimators and reflectors for the quantum wave function of Dirac fermions.

This Chapter is organized as follows. In Section 4.2, we briefly present the theoretical framework used to describe the transport properties as well as the operating

characteristic of the proposed graphene-based electronic device. In Section 4.3, we discuss the numerical results in the context of a semiclassical picture based on the quantum-optic-like analogy of the refractive index. Finally, we summarize our main findings and draw some perspectives in Section 4.4.

4.2 Model

Let us now describe the system and the theoretical framework used to compute the electronic transport properties. Motivated by the possibility of adjusting the refractive index in graphene p-n-p junctions by applying a gate potential, we propose the nanostructure schematically illustrated in Fig. 4.1 as a current switch.

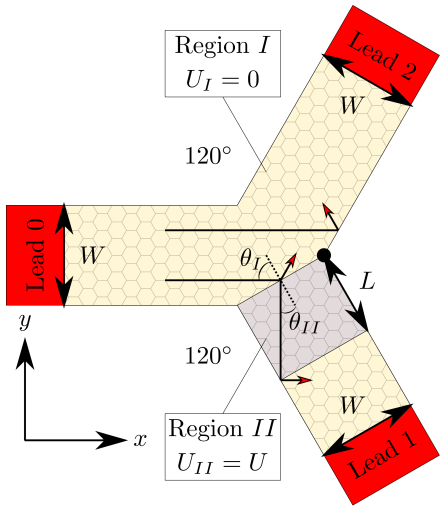

Figure 4.1: Schematic representation of the proposed three terminal graphene-based current switch. The Y-shaped device is formed by three armchair-edged graphene nanoribbons with width W and an electrostatic barrier with length L in one of the output branches. In yellow region I (gray region II) is applied a gate potential $U_I = 0$ ($U_{II} = U$). The electrons are injected into the scattering region by lead 0 and can be collected by leads 1 and 2. The black arrows represent the classical trajectories of electrons with incident and transmitted electronic momenta $\mathbf{k}_I$ and $\mathbf{k}_{II}$ and angles θ_I and θ_{II}, respectively.

To demonstrate it, we investigate the transmission of electrons through the two output branches and verify the current modulation by the application of a potential barrier in one of the output branches. The physical system consists of a three terminal junction in which the three branches are formed by graphene nanoribbons with width W. For the sake of simplicity, most of the results discussed in this work is shown for the system composed by graphene nanoribbons with armchair-type edges. As we shall demonstrate later in the next Section and also already expected, the results here obtained for armchair

edges are not qualitatively distinct from the zigzag case. Similarly, it has been reported in Ref. [74] that zigzag interface and armchair interface graphene p-n junctions exhibit qualitatively similar results for the cases of two-terminal and four-terminal devices. In addition to the setup, a gate potential is applied in the region II with barrier length L (shaded gray box region in Fig. 4.1), in the branch connected to lead 1. As shown in Fig. 4.1, the system has three ballistic leads attached to the scattering region, and the electrons are injected into the scattering region by lead 0 (left side of the sample) and can be collected by leads 1 and 2 (right side of the sample). Since both the leads and the scattering region are made out of graphene and also for the conductance calculations the size of the leads is the same as the sample, thus the contact resistance is null in this case[123]. Due to the recent achieved high experimental engineering control in microscopic scale, which in turn allows to design more and more complicated quantum device such as the three-terminal system reported in Ref. [122] formed by several local gates with predetermined shapes, one expects the simple theoretical scheme investigated here with one gate potential in one of its branches is feasible for experimental realization.

In order to show current switching, we shall calculate the probability current density, the conductance (G) as a function of the following parameters: Fermi energy (ε_F), gate potential height (U), and gate potential length (L), and the drain current (I_D) as a function of the gate voltage (V). The theoretical framework is based on the Landauer-Büttiker's formalism where the transport properties are computed within the wave function approach[31] and by using the tight-binding model with nearest-neighbor approximation to describe the charge carriers in graphene. The corresponding Hamiltonian can be written as:

$$H_{TB} = \sum_i (\varepsilon_i + U_i) c_i^\dagger c_i + \sum_{i \neq j} (\tau_{ij} c_i^\dagger c_j + \text{H.c.}), \tag{4.1}$$

where c_i ($c_i^\dagger$) annihilates (creates) an electron in site i with on-site energy ε_i. $\tau_{ij} = t = -2.8$ eV is the nearest-neighbor hopping parameter between the atoms in the A and B sublattices and U_i is the on-site potential that represents the p-n-p junction, which will be non-zero only for the atomic sites in region II in Fig. 4.1.

It is worth mentioning that the assumed lattice structure is undeformed with the same interatomic distance $a = 0.142$ nm between all the carbon-carbon bonds and no previous molecular dynamics simulations and relaxation analysis were performed be-

fore the transport calculations showed here, *i.e.* the monolayer graphene lattice structure considered here is a periodic unstrained thermalized structure. Some works reported in literature[124–127] show thermomechanical properties and phonon spectrum of monolayer graphene sheet via molecular dynamics simulation. Concerning the proposed system under investigation, it is also important to mention that it is formed by graphene nanoribbons with unpassivated edges. Wang *et al.*[128] in 2007 investigated the effects of chemical edge modification in graphene nanoribbons by a phenomenological hopping parameter for nearest-neighbor hopping to represent various chemical edge modifications and Lu *et al.*[129] in 2009 studied the hydrogen passivation of edges of armchair graphene nanoribbons. Both works analyzed the consequences of the chemical changes of the edges in graphene nanoribbons on their electronic properties using first-principles method. Structural lattice modification induced by chemical passivation results in increments of the carbon-carbon bonds and bonding angles for the atomic sites at the nanoribbon edges and consequently one expects changes in the graphene nanoribbon band structure. They showed that, in fact, the energy spectra and the band gap of graphene nanoribbons are modified and even a metal-to-insulator transition can be observed in armchair graphene nanoribbons.

From the hopping matrix and the eigenfunctions calculated numerically by diagonalizing Eq. (4.1), one can obtain the probability current density within the tight-binding model. It is obtained using the method developed in Refs. [130–133], where one defines the probability current **J** in terms of the continuity equation and, after some calculations, one obtains the current components in x and y directions for each site, which is defined by its line (i) and column (j) position in the lattice, as:

$$J_x(i,j) = \pm\frac{a}{\hbar}[2\mathrm{Im}(\Psi_{i,j}\Psi^*_{i,j\pm1}\tau_{i,j\pm1}) - \mathrm{Im}(\Psi_{i,j}\Psi^*_{i-1,j}\tau_{i-1,j}) - \mathrm{Im}(\Psi_{i,j}\Psi^*_{i+1,j}\tau_{i+1,j})], \quad (4.2)$$

and:

$$J_y(i,j) = \frac{\sqrt{3}a}{\hbar}[\mathrm{Im}(\Psi_{i,j}\Psi^*_{i+1,j}\tau_{i+1,j}) - \mathrm{Im}(\Psi_{i,j}\Psi^*_{i-1,j}\tau_{i-1,j})], \quad (4.3)$$

where the $\pm$ sign in J_x will be positive (negative) if the (i,j)-site belongs to the sublattice A (B).

All the transport calculations presented in this Chapter were performed using the KWANT code, which is a free (open source) Python package for numerical calculations on tight-binding models[31], and in which has the mentioned functions already implemented on its internal code.

The operating principle of the device is connected with the optic-like analogy of Dirac electrons in a graphene p-n junction[2,43,74,75]. Let us briefly recall an electronic plane wave propagation through a potential step in graphene, *i.e.* a graphene p-n junction with different charge densities. For this, let us assume that the regions I and II are induced by two gate potentials that shift the Dirac cones by U_I and U_{II}, respectively, and such that an electron incident at the interface with angle θ_I is transmitted with angle θ_{II}, where $\mathbf{k}_I$ and $\mathbf{k}_{II}$ are the respective wavevectors (see Ref. [43]). Since the system has translational symmetry along the direction parallel to the interface, the transverse momentum is conserved at the interface, such that $k_I \sin\theta_I = k_{II} \sin\theta_{II}$. From Dirac equation for biased graphene, we have the shifted dispersion relation $\varepsilon_F(k) = s\hbar v_F k + U_i$, where $s = +/-$ correspond to electrons/holes, respectively, i denotes the region index I and II, and v_F is the Fermi velocity. Connecting both equations, it implies a relation similar to Snell's law to ray optics where Fermi energies are equivalent to the refractive indices in each region[2, 19]:

$$n = \frac{\sin\theta_I}{\sin\theta_{II}} = \frac{\varepsilon_F - U_{II}}{\varepsilon_F - U_I}. \tag{4.4}$$

Depending on the ratio between the Fermi energy and the applied potentials, one can get configurations in which the p-n junction interface acts as a convex or a concave lens, such that the electron semiclassical trajectories are expected to converge or diverge by passing the gate potential interface, respectively. It happens when the refraction index is negative ($n < 0$) or positive ($n > 0$), that for the case where $U_I = 0$ and $U_{II} = U$ one easily sees from Eq. (4.1) that it corresponds to $U > \varepsilon_F$ and $U < \varepsilon_F$, respectively. On the other hand, for $U = \varepsilon_F$ one gets the $n = 0$ situation where the transmission angle is zero and the electrons are perfect collimated. Moreover, note from Fig. 4.1 that the negative refractive index is obtained when θ_I and θ_{II} have opposite signs, or equivalently when the sign of the tangential momentum component of the propagating electron changes while the normal component remains the same. As a consequence, the incident electrons will converge into a focal point in a similar way as it happens in a Veselago lens for ray optics[2, 75]. This optic-like direct analogy between propagated charge carriers through graphene p-n-p junction and the light trajectory is behind the operating principle of our proposed device that, in turn, is linked to the refractive index medium controlled by a gate potential, as will be discussed more in next Section.

4.3 Results

We start by assuming the symmetric case in which all the branches of the three-terminal device are exactly the same. Later, we shall consider the asymmetric case and demonstrate that the main qualitative features of the results do still hold, as one expects since it is based on the fundamental physical property regarding the negative refractive effect of the proposed structure, as we discuss next. The proposed device acts as a gate potential-controlled current switch, as discussed in Section 4.2. The probability current density of the nanostructure is shown in Fig. 4.2. We use graphene nanoribbons with widths $W = 50$ nm, where lead 0 is the electron injector, with appropriately chosen Fermi energies, and leads 1 and 2 are collectors. For the non-perturbed case, *i.e.*, without external fields, the current is symmetrically divided in both output branches, as seen in Fig. 4.2(a). This is expected because the physical system is symmetrical in relation to x-axis. Three regimes of deflection are observed when we take a rectangular potential barrier (by adjusting the height as $U = 0.5$ eV and length as $L = 44$ nm) in one of the output branches, taking different values for the Fermi energy, as seen in Figs. 4.2(b)-4.2(d). When the refractive index is negative ($\varepsilon_F < U$), it is possible to observe a partial reflection regime, as in Fig. 4.2(b). However, when $\varepsilon_F = U$, a null refractive index is achieved, and we have a total reflection regime [see Fig. 4.2(c)]. A partial reflection regime is also observed when the refractive index is positive ($\varepsilon_F > U$), as shown in Fig. 4.2(d).

As seen in Fig. 4.2, one can control the number of Dirac electrons that pass through the two output branches using a gate potential forming a p-n-p junction. To quantify the switching of electron flow between the two output branches for the same system parameters as in Fig. 4.2, we show in Fig. 4.3 the dependence of the conductance, [panel 4.3(a)] G_{01} between the input lead 0 and output lead 1 and [panel 4.3(b)] G_{02} between the input lead 0 and output lead 2, on the Fermi energy for fixed potential barrier amplitudes. As expected for the symmetric system with $U = 0$, one has $G_{01}(\varepsilon_F) = G_{02}(\varepsilon_F)$, as shown by the blue curves in Figs. 4.3(a) and 4.3(b). For $U \neq 0$, one observes three different conductance regimes for $G_{01}(\varepsilon_F)$ and $G_{02}(\varepsilon F)$ with respect to the energy ranges $0 \leq \varepsilon_F \leq U/2$, $U/2 < \varepsilon_F \leq U$ and $U < \varepsilon_F$, that are linked to the refractive index of the n-p-n junction to be $n \leq -1$, $-1 < n \leq 0$, and $n > 0$, respectively. Such nature of the conductance $G_{01}(\varepsilon_F)$ related to the different signs of the refraction index

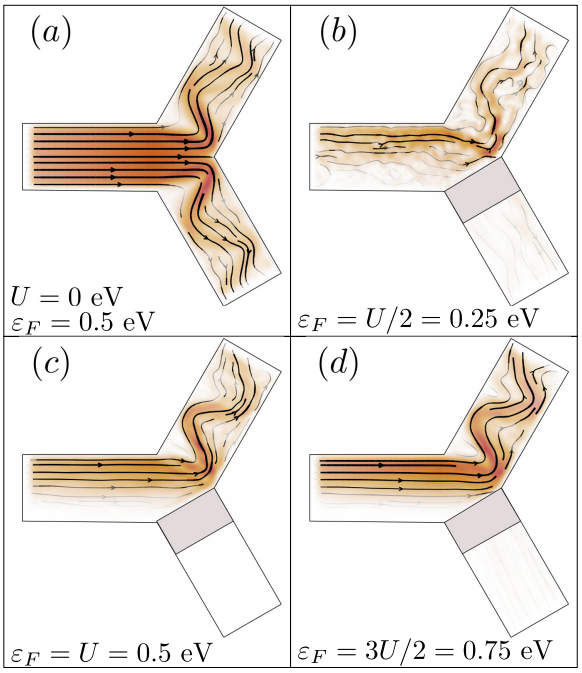

Figure 4.2: Probability current densities for the system shown in Fig. 4.1 for (a) the non-perturbed case ($U = 0$), and under the effect of a gate potential $U = 0.5$ eV for Fermi energy values (b) $\varepsilon_F = 0.25$ eV, (c) $\varepsilon_F = 0.5$ eV, and (d) $\varepsilon_F = 0.75$ eV. It is taken $W = 50$ nm and $L = 44$ nm. The shaded gray region in bottom output lead represents the potential barrier with barrier high U.

will be discussed later in detail in this Section. Note that for $\varepsilon_F = U$ (*i.e.* $n = 0$), regardless the potential value $U > 0$, the conductance G_{01} has a minimum, being in accordance to the fact that this situation represents the maximum deflection as shown in Fig. 4.2(c). As a consequence of these three different regimes with respect to the Fermi energy ranges, the conductance G_{02} displays approximately increasing monotonic curves with three different slopes, being the higher the G_{02} value the lower the conductance G_{01}, as intuitively expected. Therefore, the ratio G_{02}/G_{01} depicted in Fig. 4.3(c) shows peaks at $\varepsilon_F = U$ for each fixed potential configuration.

Hereafter, we shall discuss only the conductance G_{01}, since it can be easily seen that the portion of the injected electrons not collected by lead 1 will be captured by the output lead 2 or back-scattered to the input lead 0. In order to verify the validity and robustness of the finding results with respect to the edge-type, we depict in the bottom panels of Fig. 4.3 the conductance plots for (d) G_{01}, (e) G_{02}, and (f) G_{02}/G_{01} for the same system parameters as in panels (a), (b) and (c), respectively, by considering now the device composed by graphene nanoribbons with zigzag edges, instead of armchair ones as assumed along the entire work. By comparing the results for the armchair (top panels)

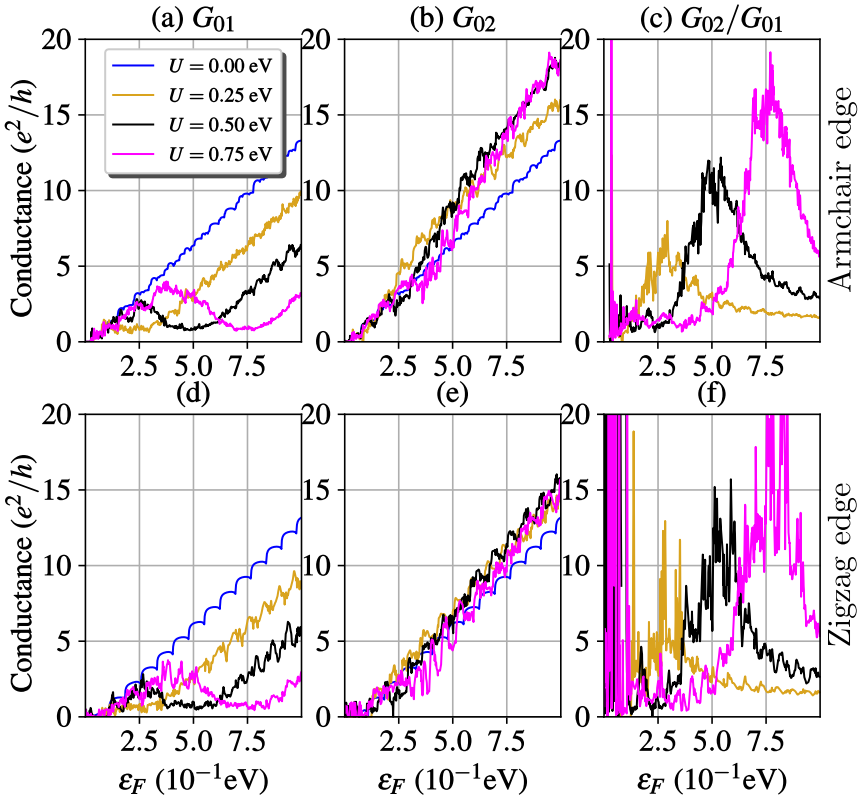

Figure 4.3: Conductance (a, d) G_{01} between leads 0 and 1, (b, e) G_{02} between leads 0 and 2, and (c, f) ratio G_{02}/G_{01}, as a function of the Fermi energy ε_F for the same system parameters as in Fig. 4.2 and taking different gate potential heights: $U = 0$ (blue curve), $U = 0.25$ eV (yellow curve), $U = 0.5$ eV (black curve), and $U = 0.75$ eV (magenta curve). Top and bottom panels correspond to results for the system composed by three (a, b, c) armchair and (d, e, f) zigzag graphene nanoribbons.

and zigzag (bottom panels) cases, one notices that there is a good qualitative agreement between them, showing that the device proposal brought up here is independent of the type of edge chosen for the nanoribbons.

Let us next analyze the conductance G_{01} as a function of the gate potential height to different widths (W) at length (L) fixed, and distinct lengths (L) at width (W) fixed, as shown in Figs. 4.4(a) and 4.4(b), respectively. Taking a fixed Fermi energy $\varepsilon_F = 0.5$ eV and varying the gate potential height from 0.0 to $2\varepsilon_F$, it is possible to observe that the minimum conductance increases to large W [see Fig. 4.4(a)], and decreases to large L [see Fig. 4.4(b)]. This behavior can be understood by a simple quantum confinement picture for a scattering problem of electrons passing through/back a rectangular potential barrier: (i) as the width W increases, *i.e.* for larger systems since here it corresponds to larger Y-junction branches widths, there are more transverse electronic modes available to contribute to transport and thus the conductance is larger the wider the width W;

and (ii) as L increases, it is well-known from basic quantum mechanics that transmission becomes smaller, decaying exponentially as function of the barrier length when the barrier length exceeds the tunneling length that is, in turn, associated with the inverse of the wavelength of the states within the barrier.

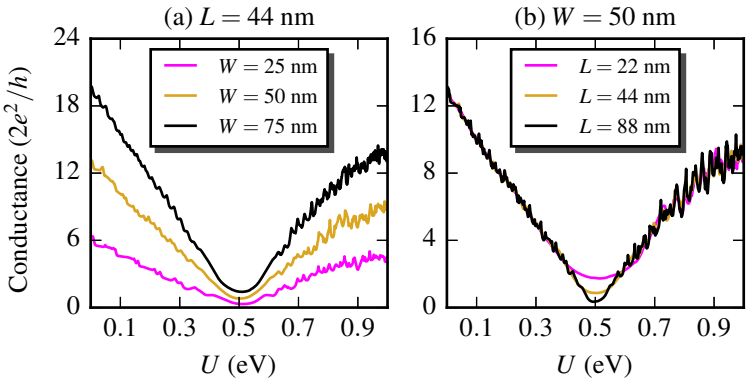

Figure 4.4: Conductance between leads 0 and 1 as a function of the gate potential height for (a) different sample width: $W = 25$ nm (magenta curve), $W = 50$ nm (yellow curve), and $W = 75$ nm (black curve), with a fixed barrier length $L = 44$ nm, and for (b) different potential barrier lengths: $L = 22$ nm (magenta curve), $L = 44$ nm (yellow curve), and $L = 88$ nm (black curve), with a fixed ribbon width $W = 50$ nm. It is taken $\varepsilon_F = 0.5$ eV.

This understanding of the minimum conductance G_{01} behavior as a function of W and L is relevant in order to achieve a maximum efficiency of the proposed device operating as a current switch, such that the ideal situation is $G_{01}(U = \varepsilon_F) \to 0$ that happens when L is large and W is small. In addition, one could also associate its increasing and decreasing with the W and L increasing, respectively, with the standard Landauer conductance relation for large ballistic conductors that recovers the familiar Ohm's law that says that $G \propto W$ and $G \propto 1/L$[123]. Far from the $(\varepsilon_F = U)$-value, one can notice from Fig. 4.4 that the conductance G_{01} increases, and consequently more and more electrons pass through the barrier and are collected by the lead 1. Such conductance presents an asymmetric behavior in relation to $(U = \varepsilon_F)$-axis (see Ref. [43]), where two different trends are observed for $U < \varepsilon_F$ and $U > \varepsilon_F$. From Eq. (4.4), the nature of those two different conductance regimes is related to the different signs of the refractive index, being positive and negative for $U < \varepsilon_F$ and $U > \varepsilon_F$, respectively. In the negative (positive) refractive index regime, a decreasing (an increasing) tendency of the conductance G_{01} with the gate potential height is observed, and consequently an opposite regime is expected to occur for the conductance G_{02}. For a positive refractive index regime $(U < \varepsilon_F)$,

it is possible to see a smoother shape of the conductance, in contrast with the large oscillations that occur in the negative refractive index regime ($U > \varepsilon_F$). The amplitude of these oscillations (see $U > 0.6$ eV) is greater the larger as L increases. This can be explained by simple geometry analysis of the semiclassical electronic trajectories, since as L increases there are more reflections by the boundaries into the barrier region, leading to more interference, and thus oscillations similar to Fabry-Pérot resonances are seen (see more details in Ref. [134]).

Let us now consider the conductance G_{01} as a function of Fermi energy (ε_F) for three different gate potential widths (W) at a fixed length $L = 44$ nm [being the same parameter assumed in Figs. 4.1, 4.3 and 4.2(a)], as well as a function of the potential barrier length (L) for three distinct Fermi energies at a fixed width $W = 50$ nm, as depicted in Figs. 4.5(a) and 4.5(b), respectively. As already discussed for Fig. 4.3(a), the results of Fig. 4.5(a) for the conductance as a function of ε_F show: (i) three different regimes for $G_{01}(\varepsilon_F)$ with respect to the energy ranges $0 \leq \varepsilon_F \leq U/2$, $U/2 < \varepsilon_F \leq U$ and $U < \varepsilon_F$, corresponding to the refractive index regimes $n \leq -1$, $-1 < n \leq 0$, and $n > 0$, respectively; (ii) a pronounced peak in the conductance at the same position $\varepsilon_F = U/2 = 0.25$ eV, or equivalently when $\theta_I = -\theta_{II}$ and thus $n = -1$, regardless of the sample width, being a consequence of the negative refraction induced by Veselago lens property in a graphene p-n-p junction[43] that makes the electronic trajectories to be convergent in the electrostatic junction and thus reducing the reflection at branch boundary; (iii) a minimum in the conductance G_{01} at $\varepsilon_F = U = 0.5$ eV, regardless of the sample width. Notice that, by replacing $\varepsilon_F = U$ in Eq. (4.1), we obtain $\theta_{II} = 0$ and $n = 0$, which means that the electron beams have almost completely deviated to the branch connected to lead 2; (iv) an almost monotonic increasing behavior of the conductance with Fermi energy for ε_F greater than the minimum conductance.

For the analysis of the conductance dependence on the gate potential length shown in Fig. 4.5(b), we assumed a gate potential height $U = 0.5$ eV and width $W = 50$ nm. One observes a pronounced reduction in the conductance already for small values of L with its minimum being dependent on the chosen Fermi energy. For $\varepsilon_F = U = 0.5$ eV [yellow curve in Fig. 4.5(b)] that corresponds to the $n = 0$ case, the conductance in units of e^2/h scales as $\approx A/(L + B)$, with the fitting constants being $A \approx 0.9912$ and $B \approx -0.9293$, and it tends to zero the larger the potential barrier length L. As

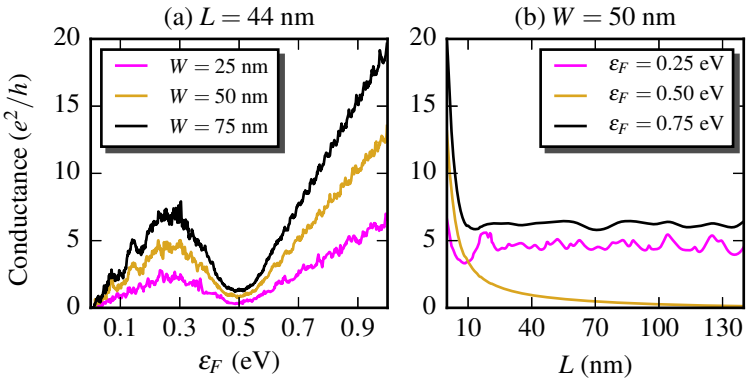

Figure 4.5: Conductance between leads 0 and 1 as a function of (a) Fermi energy and (b) potential barrier length. In panel (a) it is assumed three different system widths: $W = 25$ nm (magenta curve), $W = 50$ nm (yellow curve), and $W = 75$ nm (black curve), with a fixed potential barrier length $L = 44$ nm. In panel (b) it is considered three different Fermi energies: $\varepsilon_F = 0.25$ eV (magenta curve), $\varepsilon_F = 0.50$ eV (yellow curve), and $\varepsilon_F = 0.75$ eV (black curve), with a fixed system width $W = 50$ nm. It is taken $U = 0.5$ eV.

previously discussed for Fig. 4.4(b), the larger L the more efficient the device, since it will be able to completely turn off the current between the leads 0 and 1. Therefore, Fig. 4.5(b) emphasizes that the most favorable configuration of the device is for large potential barrier length L. This decaying tendency for $G(\varepsilon_F = U) \to 0$ does not occur for $\varepsilon_F > U$ or $\varepsilon_F < U$. Note, by the black (magenta) curve for $\varepsilon_F = 0.75$ eV $> U$ ($\varepsilon_F = 0.25$ eV $< U$) corresponding to the positive (negative) regime in the refractive index, that for $L > 10$ nm the conductance reaches an approximately constant non-zero average value, being this threshold greater for $\varepsilon_F > U$ (see black curve) case than for $\varepsilon_F < U$ (see magenta curve). As shown in Figs. 4.1(b) and 4.1(d) for $\varepsilon_F = 0.25$ eV $< U$ and $\varepsilon_F = 0.75$ eV $> U$, respectively, both situations for $n < 0$ and $n > 0$ lead to a partial reflection regime and thus the conductance G_{01} is larger than for the case $n = 0$.

In order to determine the change between drain current regimes, that is, to estimate how fast the physical system changes from one regime to another related to $U < \varepsilon_F$, $U = \varepsilon_F$ and $U > \varepsilon_F$ energy ranges, we calculate the logarithm of the drain current as a function of gate voltage for different potential barrier widths and lengths, as shown in Figs. 4.6(a) and 4.6(b), respectively, by taking the same system parameters as in Fig. 4.4. The calculation is performed by taking the linear response formula limit that allows to write $\log(I_D/I_0) = \log(V) + \log(G)$, where $I_0 = 2e^2/h$[22].

Figs. 4.6(a) and 4.6(b) exhibit a distinct approximate linear slope of the drain

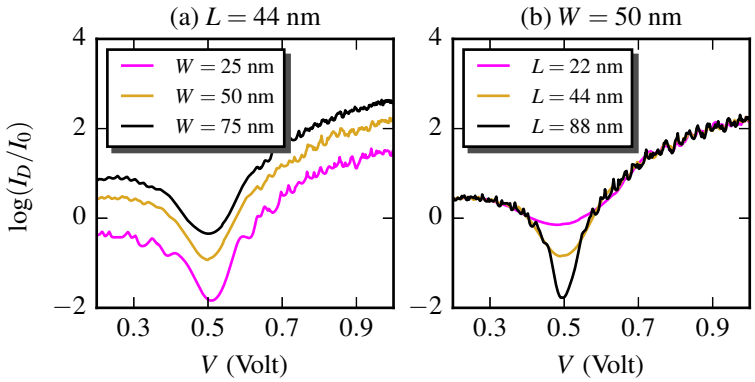

Figure 4.6: Logarithm of the drain current (in units of $I_0 = 2e^2/h$) as a function of the gate voltage for (a) different system widths: $W = 25$ nm (magenta curve), $W = 50$ nm (yellow curve), and $W = 75$ nm (black curve), with a fixed potential barrier length $L = 44$ nm, and (b) different potential barrier lengths: $L = 22$ nm (magenta curve), $L = 44$ nm (yellow curve), and $L = 88$ nm (black curve), with a fixed system width $W = 50$ nm. It is taken $\varepsilon_F = 0.5$ eV.

current for $V < \varepsilon_F/e$ and $V > \varepsilon_F/e$. By comparing Fig. 4.6 with Fig. 4.4, one can notice that the slope for $U < \varepsilon_F$ and $U > \varepsilon_F$ energy regimes switches places in Fig. 4.4 related to Fig. 4.6, and moreover, the minimum conductance dependence (*i.e.*, at $V = \varepsilon_F/e = 0.5$ V) on W and L is more evident in Fig. 4.6.

Next, we study the robustness of conductance modulation on the symmetry of the proposed setup. For this, we assume asymmetric situations in which the output branches widths are different. It is done in a systematic way by moving the bifurcation point on the corner of the two output graphene nanoribbons, but keeping the angle between two adjacent terminals fixed by 120°, such that the type of the edge termination is preserved as armchair ones. The asymmetric three-terminal junction is displayed in Fig. 4.7. As seen, the bifurcation point (indicated by a black dot) is located away from the dashed black line which denotes the axis of the injector lead. By moving the bifurcation point up (down) with respect to the symmetric position, one increases (decreases) the nanoribbon width of the bottom output lead. For the system size parameters adopted in Fig. 4.7, one has that $W_1^i > W_1^{ii} > W_1^{iii} > W_1^{iv}$. For a better analysis of the asymmetry effect on the conductance, one should compare the conductance dependence on the gate potential height (left panel in Fig. 4.7) with the symmetric case shown in Fig. 4.4(a). One can notice similarly to the symmetric case, the conductance amplitude decreases the larger is W_1^j. However, in contrast to Fig. 4.4(a) here the conductance exhibits more pronounced modulations by varying the potential barrier height. Such noise in the con-

ductance is due to the interplay effect of the changes on the potential barrier width and length, as well as the incident angles of the injected electrons. Note that as W_1^j decreases, the p-n junction interface between the central scattering region and the bottom branch becomes more and more aligned with the boundary of terminal 0 which, in turn, implies to injected electrons almost parallel to the p-n interface and, consequently, increasing the reflectance and thus significantly decreasing transmission.

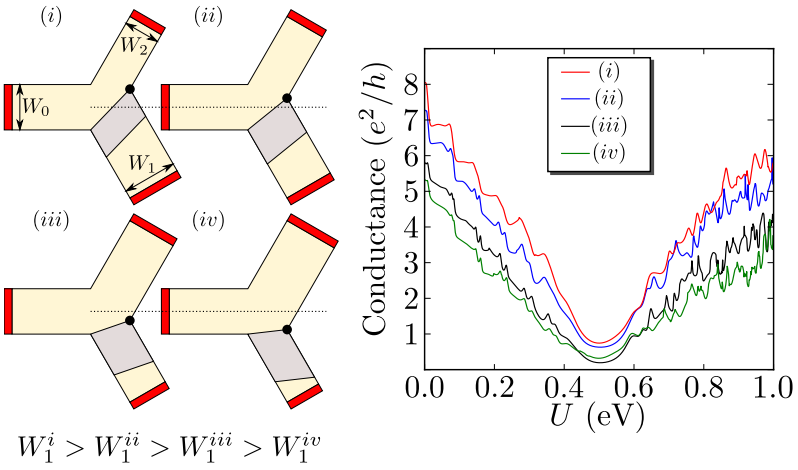

Figure 4.7: Conductance between leads 0 and 1 as a function of the gate potential height similarly to Fig. 4.4, but now for asymmetric setups composed by three graphene nanoribbons with different widths. Red, blue, black and green curves correspond to the system setup (i), (ii), (iii), and (iv), respectively. The width of the output branch with the potential barrier increases (decreases) as the connection spot (denotes by the black dot) moves up (down) away from the symmetric position, such that $W_1^i > W_1^{ii} > W_1^{iii} > W_1^{iv}$. It is taken $\varepsilon_F = 0.5$ eV.

Therefore, the conductance variation here is a combination of geometric and quantum effects, being the former owing to the increasing of backscattering electronic modes by the walls of the system and the latter related to the decreases in the number of accessible electronic states for a fixed energy range when one decreases the output nanoribbon width. Moreover, our results show that the calculated conductance is qualitatively the same regardless the symmetry of the system, *i.e.* the proposed system seems to be robust against different geometrical parameters of the terminals.

4.4 Conclusion

We proposed a current switch-like electronic device model based on a graphene p-n-p junction with three terminals in Y-shape. Using Landauer-Büttiker's formalism within the tight-binding approach to describe the electronic transport, we explained the

operating principle of the nanostructure. In the absence of a gate potential, the electron beam is equally divided between the two output branches. On the other hand, when a gate potential is applied in the branch connected to one of leads, it is possible to deviate the current to the other. As a proof-of-concept that the proposed device can act as a current switch, we initially investigated the behavior of the probability current density. Next, we calculated the conductance as a function of three parameters (Fermi energy, potential barrier height, and potential barrier length), and finally, we investigated the drain current as a function of the gate voltage. The results showed that the device efficiency as a switch increases for narrower the Y-junction branches and for larger potential barrier lengths L. Moreover, we demonstrated that these results are robust in regard to the asymmetry that may arise in the construction of the connections of the system. We expect these results will prove useful for designing of graphene-based current switches that work even in the absence of a gap in the graphene band structure. Moreover, due to the absence of the contact resistance in the investigated system here, since both the leads and the scattering region are made out of graphene and the size of the leads is the same as the sample, our theoretical findings can be viewed as a scenario of an optimum experimental device performance.

5 MODULATION OF PERSISTENT CURRENT IN GRAPHENE QUANTUM RINGS

In this Chapter, we investigate the effect of long-range impurity potentials on the persistent current of graphene quantum rings in the presence of an uniform perpendicular magnetic field. The impurity potentials are modeled as finite regions of the ring with a definite length. We show that, due to the relativistic and massless character of the charge carriers in graphene, the effect of such non-uniform potentials on the energy spectrum and on the persistent current of the rings can be reliably modeled by assuming a non-perturbed ring and including an additional phase due to the interaction of the charge carriers with the potential. In addition, the results show the presence of localized states in the impurity regions. Moreover, we show that for the case of a potential created by a p-n-p junction, the persistent current can be modulated by controlling the voltage at the junction.

5.1 Introduction

Persistent currents in conducting rings are electric currents found in normal metals even in the absence of external bias[135, 136]. The existence of such currents is an example of a mesoscopic-scale quantum phenomenon, and is related to the Aharonov-Bohm phase induced in the eigenstates of electrons of a ring-shaped conductor in the presence of a magnetic field[137]. They have been observed experimentally at low temperatures and for ring sizes that are small compared to the phase relaxation length of the sample[138–140]. It was found that the sign and magnitude of the persistent currents are influenced by the external magnetic field, as well as by scattering from impurities and vacancies[141, 142].

Recent studies have obtained the energy spectra and persistent currents for graphene quantum rings[131, 142–153]. These are found to be strongly influenced by the ring geometry and by the microscopic details of the edges. On the other hand, for some

ring geometries, the energy spectra can be obtained by a simple one-dimensional model within the continuum approximation by solving the Dirac equation for a zero width ring geometry by freezing out the carrier radial motion[131, 143]. The comparatively large phase coherence length of electrons in graphene is expected to allow the observation of persistent currents at larger scales than in normal metals. One important point that must be taken into account in the analysis of these structures is the effect of impurities. In the case of graphene, the presence of impurities can lead to unexpected results due to the massless Dirac fermion character of its charge carriers. Among the unusual properties of graphene, one can mention the perfect transmission of electrons and holes through potential barriers, also known as Klein tunneling, which is a consequence of its gapless electronic spectrum and the chiral nature of carriers in the system[11, 20]. That property leads to the absence of backscattering caused by long-range potentials, as well as to an analogy between the transport of Dirac fermions in graphene p-n junctions and the propagation of light in media with negative refraction indices[2, 25, 43, 44, 88].

Apart from the perfect transmission through a potential barrier, the linearity of the dispersion of carriers in graphene causes the wavefunction of an incident charge carrier to undergo a phase shift that is energy-independent, being simply a function of the geometry of the potential. In the case of the square potential created by a gate voltage, the phase shift is a function of the product of the potential height and the length of the barrier. That effect has been previously investigated for time-dependent barriers[154] and as a way to obtain a graphene-based electron interferometer[22]. In this Chapter, we consider the effect of the gate-induced phase shift on the persistent current in a graphene quantum ring and how that, in turn, depends on the parameters of the potential barrier.

This Chapter is organized as follows. We describe a theoretical approach for quantum rings in single-layer graphene using a simplified continuum model in Subsection 5.2.1 and present the numerical method based on the tight-binding model in Subsection 5.2.2. The analytical and numerical results are presented and compared in Section 5.3. Section 5.4 contains a summary of the main results and the conclusions.

5.2 Theoretical framework

The nanostructure investigated here consists of a hexagonal ring made of graphene nanoribbons, as shown in Fig. 5.1. The ring is defined by the side lengths

L_1 and L_2, properly chosen so that the corners of the external and internal hexagons are both armchair, respectively. We define the average radius R in terms of L_1 and L_2 as $R = [(3\sqrt{3})/(8\pi)]^{1/2}(L_1 + L_2)$. We assumed $L_1 \approx 50$ nm and $L_2 \approx 33$ nm (resulting an average radius of $R \approx 38$ nm), corresponding to $N_1 = 176$ and $N_2 = 115$ carbon hexagons at the outer and inner edges, respectively, in all figures from here onwards, unless otherwise stated. A uniform magnetic field $\mathbf{B}$ is applied perpendicularly to the ring plane, and a potential barrier of height V and length W is inserted in the lower arm of the ring. Results for charge persistent currents in graphene quantum rings have been reported in the literature by considering circular geometry[131, 143, 153] and hexagonal shape with armchair[142, 144] and zigzag[148] edges. da Costa *et al.* demonstrated that a simplified model describing an infinitely thin circular Dirac ring show good agreement with those obtained for hexagonal and rhombus armchair graphene rings within the tight-binding model[131]. Based on that and owning to avoid the influence of edge states, the boundaries of the system are assumed to be terminated by armchair-type edges. It allows us to directly compare the tight-binding results with the analytical simplified solution for an one-dimensional circular Dirac quantum ring. The theoretical framework used in each of the two aforementioned models are shown below: the continuum model in Subsection 5.2.1 and the tight-binding model in Subsection 5.2.2.

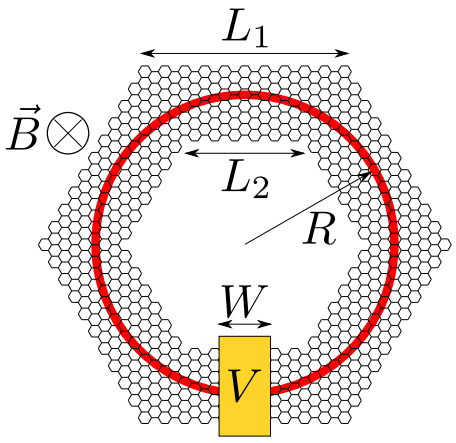

Figure 5.1: Schematic illustration of the nanostructure investigated in this Chapter. The hexagonal-shaped ring is characterized by the inner L_1 and outer L_2 ring lengths, and is subjected to a perpendicular magnetic field $\mathbf{B}$. A potential barrier of height V and length W is applied in one of the ring arms, as highlighted in yellow region. The black polygon figure and the one-dimensional ring represented by the red circle with average radius $R = [(3\sqrt{3})/(8\pi)]^{1/2}(L_1 + L_2)$ are, respectively, the configurations considered in the tight-binding model and the simplified continuum model.

5.2.1 *Continuum model*

Graphene consists of carbon atoms arranged in a honeycomb crystal structure. Its energy spectrum in the absence of external fields can be easily obtained through the diagonalization of the Hamiltonian within the tight-binding model[1,37,155] and exhibits no bandgap at two non-equivalent points in reciprocal space (**K** and **K′**). Within a first-order Taylor series expansion in the vicinity of **K** and **K′**, the energy is found to depend linearly on the wavevector, and the electron is seen to behave like a massless Dirac fermion described by the following Dirac Hamiltonian:

$$H_D = v_F \boldsymbol{\sigma} \cdot (\mathbf{p} + e\mathbf{A}) + V\mathbf{I}, \tag{5.1}$$

for **K** valley states and when considering states in the **K′** valley one should replace $\boldsymbol{\sigma}$ by its complex conjugate $\boldsymbol{\sigma}^*$. $v_F = (3at)/(2\hbar)$ is the Fermi velocity, $\boldsymbol{\sigma} = (\sigma_x, \sigma_y, \sigma_z)$ denotes the Pauli vector, $\mathbf{p}$ is the in-plane momentum operator, $-e$ is the electron charge, $\mathbf{A}$ is the magnetic vector potential, V is the electric scalar potential, and $\mathbf{I}$ is the identity matrix. The eigenstates of the Hamiltonian (5.1) are the two-component pseudospinor wavefunction $\Psi = [\psi_A \quad \psi_B]^T$, where ψ_A and ψ_B are the envelope functions referring to the probability amplitudes at A and B Bravais sublattices, respectively.

Within the continuum approach, we consider a simplified circular graphene quantum ring that is obtained by freezing the radial motion. It results in an effective Dirac Hamiltonian describing electrons confined in an one-dimensional graphene quantum ring, such that this angular confinement problem can be solved analytically. Following the approximation reported in Refs. [131,143], it is convenient to write the Hamiltonian (5.1) in polar coordinates. To do this, firstly, we write the Pauli matrices σ_x and σ_y as:

$$\sigma_r = \begin{bmatrix} 0 & e^{-i\varphi} \\ e^{i\varphi} & 0 \end{bmatrix}, \quad \sigma_\varphi = i \begin{bmatrix} 0 & -e^{-i\varphi} \\ e^{i\varphi} & 0 \end{bmatrix}, \tag{5.2}$$

where φ is the polar angle associated with the momentum vector. Thus, the Hamiltonian (5.1) in the absence of external potential ($V = 0$), in the presence of an perpendicular magnetic field ($\mathbf{B} = B\hat{z}$), and around the **K** Dirac point is given by:

$$H_D = -i\hbar v_F \begin{bmatrix} 0 & \left(\Pi_r^* + e^{-i\varphi \frac{\pi r B}{\Phi_0}}\right) \\ \left(\Pi_r - e^{i\varphi \frac{\pi r B}{\Phi_0}}\right) & 0 \end{bmatrix}, \tag{5.3}$$

where it was assumed the symmetric gauge $\mathbf{A} = \mathbf{r} \times \mathbf{B}/2 = (1/2)rB\hat{\varphi}$, $\Pi_r = e^{i\varphi}[(\partial/\partial r) + (i/r)(\partial/\partial\varphi)]$ is the radial momentum operator, and $\Phi_0 = h/e$ is the magnetic quantum

flux. By assuming that the ring width approaches zero, the momentum operator must be frozen in the radial direction[131], so that there will be no explicit radial dependence in our model and the persistent current will flow only in the angular direction[143]. The radial momentum operator in cylindrical coordinates arises through quantization of the classical radial momentum[156]:

$$\mathbf{p}_r = \frac{1}{2}(\mathbf{p}\cdot\hat{r} + \hat{r}\cdot\mathbf{p}), \tag{5.4}$$

and it has the following form:

$$\mathbf{p}_r = -i\hbar\Big(\frac{\partial}{\partial r} + \frac{1}{2r}\Big). \tag{5.5}$$

Taking $\mathbf{p}_r \to 0$ and $r \to R$, we obtain:

$$\frac{\partial}{\partial r} \to -\frac{1}{2R}, \tag{5.6}$$

being R the one-dimensional ring radius. Thus, the simplified Hamiltonian becomes:

$$H_D = \frac{\hbar v_F}{R}\begin{bmatrix} 0 & e^{-i\varphi}\left(\frac{i}{2} - \Theta\right) \\ e^{i\varphi}\left(\frac{i}{2} + \Theta\right) & 0 \end{bmatrix}, \tag{5.7}$$

where $\Theta = d/d\varphi + i\Phi_R/\Phi_0$ and $\Phi_R = \pi R^2 B$ is the magnetic flux through the graphene quantum ring.

The eigenstates of the simplified Hamiltonian (5.7) are two-component pseudospinors which, in plane polar coordinates, are given by:

$$\Psi(\varphi) = \frac{1}{\sqrt{2}}\begin{bmatrix} e^{im\varphi} \\ \pm i e^{i(m+1)\varphi} \end{bmatrix}, \tag{5.8}$$

where $m \in \mathcal{Z}$ is the angular momentum index and radial parts of the spinors are constant where the $+$ $(-)$ sign refers to electrons (holes). The eigenenergies, in turn, are given by:

$$E_{0,\pm} = \pm\frac{\hbar v_F}{R}\left(m + \frac{\Phi_R}{\Phi_0} + \frac{1}{2}\right). \tag{5.9}$$

Considering the system described in Fig. 5.1, the phase acquired by the electrons as they propagate along the nanostructure can be written in terms of the total magnetic flux Φ_R enclosed by the graphene quantum ring as:

$$e^{i\frac{e}{\hbar}\oint_P \mathbf{A}\cdot d\mathbf{l}} = e^{i\frac{e}{\hbar}\int_S \mathbf{B}\cdot d\mathbf{a}} = e^{2\pi i\frac{\Phi_R}{\Phi_0}}. \tag{5.10}$$

However, if a potential barrier is introduced across one of the arms of the ring, although it will not cause reflections, due to Klein tunneling, it will nevertheless add an extra phase ϕ to the wavefunction, which is proportional to the height V and length W of the potential barrier[22, 154]:

$$\phi = \frac{VW}{\hbar v_F}, \tag{5.11}$$

thus, the phase term becomes:

$$e^{i\frac{e}{\hbar}\oint_P \mathbf{A}\cdot d\mathbf{l} \pm i\phi} = e^{2\pi i \frac{\Phi_R}{\Phi_0} \pm i\phi}. \tag{5.12}$$

Therefore, it can be seen that the presence of the potential barrier acts as an extra magnetic flux:

$$\Phi' = \Phi_R \pm \frac{\Phi_0 \phi}{2\pi}, \tag{5.13}$$

and, consequently, the resulting energy spectrum for one-dimensional graphene quantum ring can be obtained by replacing this new magnetic flux into Eq. (5.9), that reads:

$$E = E_{0,\pm} + \frac{W}{2\pi R} V. \tag{5.14}$$

Note that the energy spectrum (5.14) is composed by two terms, being the first one, $E_{0,\pm}$, related to the energy spectrum in the absence of the potential barrier and the other one is the bias energy contribution. Moreover, one notices that the energy spectrum shows a linear dependence on the potential barrier height and width, with slopes equal to $W/(2\pi R)$ and $V/(2\pi R)$, respectively.

If we now assume the existence of N potential barriers, with possibly different lengths and heights, the energy spectrum of the graphene ring can be easily obtained by taking the phase substitution $\phi \to \sum_i^N \phi_i$ into Eq. (5.13), resulting in a sum of terms in Eq. (5.14) given by the products of the heights and lengths of each potential barrier, such as:

$$E = E_{0,\pm} + \frac{1}{2\pi R} \sum_{n=1}^{N} V_n W_n, \tag{5.15}$$

and the corresponding wavefunctions of the eigenstates can be obtained by a piece-wise function using Eq. (5.8) with coefficients obtained through matching the wavefunctions.

5.2.2 *Tight-binding model*

Our analytical results obtained via the effective one-dimensional Dirac approach, described in Subsection 5.2.1, are validated by comparison with energy levels cal-

culated with the nearest-neighbor tight-binding Hamiltonian for π electrons in graphene, which reads:

$$H_{TB} = \sum_i (\varepsilon_i + V_i) c_i^\dagger c_i + \sum_{i \neq j} (\tau_{ij} c_i^\dagger c_j + \text{H.c.}), \tag{5.16}$$

where c_i ($c_i^\dagger$) annihilates (creates) an electron in site i with on-site energy ε_i, $\tau_{ij} = -2.7$ eV is the nearest-neighbor hopping parameter between the carbon atoms in the A and B Bravais sublattices, and V_i is the on-site potential used here to modeled impurity potentials in a finite region with a definite length, that can be similarly simulated by top/bottom gates influence creating a p-n-p junction in one of the ring arms. As depicted in Fig. 5.1, the gate potential is defined in the lower arm of the graphene quantum ring, being characterized by its barrier height V and width W. The effect of an external magnetic field is introduced in this model by using the Peierls substitution for the hopping energies with the phase transformation given by Eq. (5.10), *i.e.* by taking $\tau_{ij} \rightarrow \tau_{ij} \exp\left[ie/\hbar \int_j^i \mathbf{A} \cdot d\mathbf{l}\right]$[157,158]. Here we choose the Landau gauge $\mathbf{A} = -By\hat{x}$, so that the hopping parameter becomes:

$$\tau_{ij} \;\rightarrow\; \tau_{ij} e^{i \frac{2\pi\sqrt{3}}{9a^2} \frac{\Phi}{\Phi_0} (y_2 + y_1)(x_2 - x_1)}, \tag{5.17}$$

where $a = 0.142$ nm is the lattice parameter of graphene and $\Phi = 3\sqrt{3}Ba^2/2$ is the magnetic flux through a hexagon of carbon atoms.

Once we have the hopping matrix and tight-binding eigenfunctions already computed, it is possible to obtain the probability current density from the method developed in Refs. [131–133,159]. It is based on the finite difference scheme for the probability density that, in turn, obeys the continuity relation. The discretized continuity relation reads as:

$$J_n - J_{n+1} = a \frac{\partial \rho_{n,n}}{\partial t}, \tag{5.18}$$

where $\rho_{n,n} = \langle n|\rho|n\rangle$ are the matrix elements of the density matrix operator $\rho = |\Psi\rangle\langle\Psi|$ and the time derivative in Eq. (5.18) is determined by the equation of motion for ρ:

$$\frac{\partial \rho_n}{\partial t} = \frac{i}{\hbar} \langle \Psi_n | [\rho, H_{TB}] | \Psi_n \rangle, \tag{5.19}$$

where $|\Psi_n\rangle = \langle n|\Psi\rangle$, resulting, for the case of nearest-neighbor hopping approach, in:

$$J_n = \frac{2a}{\hbar} \text{Im}(\Psi_n^* \Psi_{n-1} H_{n,n-1}^{TB}). \tag{5.20}$$

The components of the probability current density in the x and y directions for each lattice site of graphene, which is defined by its line (i) and column (j) positions in the lattice, are:

$$J_x(i,j) = \pm\frac{a}{\hbar}[2\mathrm{Im}(\Psi_{i,j}\Psi^{\dagger}_{i,j\pm1}\tau_{i,j\pm1}) - \mathrm{Im}(\Psi_{i,j}\Psi^{\dagger}_{i-1,j}\tau_{i-1,j}) - \mathrm{Im}(\Psi_{i,j}\Psi^{\dagger}_{i+1,j}\tau_{i+1,j})], \quad (5.21)$$

and:

$$J_y(i,j) = \frac{\sqrt{3}a}{\hbar}[\mathrm{Im}(\Psi_{i,j}\Psi^{\dagger}_{i+1,j}\tau_{i+1,j}) - \mathrm{Im}(\Psi_{i,j}\Psi^{\dagger}_{i-1,j}\tau_{i-1,j})], \quad (5.22)$$

where the $-$ $(+)$ sign in J_x will be positive (negative) if the (i,j)-site belongs to the sublattice A (B) and the presence of a magnetic field, in turn, is included by the Peierls substitution in the hopping parameters[160]. $\Psi_{i,j}$ in Eqs. (5.21) and (5.22) represents the wave function amplitude in the (i,j) lattice index position within the finite difference scheme.

The numerical calculations presented in this Chapter were performed using the KWANT code[31], which is a open source Python package for numerical calculations on tight-binding models and in which has the mentioned functions already implemented on its internal code.

5.3 Results

Previous studies reported that energy levels in graphene quantum rings in the presence of a uniform magnetic field are strongly affected by their geometry and the types of their edges[131, 142–153]. In addition, it has been shown[131] that the analytical results of a simplified continuum model agree with the tight-binding results only for specific combinations of geometry and edge types. Specifically, the analytical results of an infinitely thin circular ring show good agreement with the numerical results of hexagonal and rhombus-like rings with armchair edges[131]. In this sense, we use this combination of analytical and numerical methods to investigate the effect of long-range impurity potentials on the persistent current of graphene quantum rings in the presence of a uniform magnetic field. The impurity potentials are modeled as finite regions of the ring with a defined length, simulated here by a p-n-p junction in one of the ring arms. For this, we compare the analytical results from the simplified continuum model described in Subsection 5.2.1 with the numerical results from the tight-binding model presented in Subsection 5.2.2. As seen in Subsection 5.2.1, the effect of such non-uniform potentials

on the energy spectrum and on the persistent current of the rings can be modeled by assuming a non-perturbed ring and including an additional phase due to the interaction of charge carriers with the potential.

First, we investigate the dependence of energy levels on the magnetic flux through a single carbon hexagon in the absence [Fig. 5.2(a)] and in the presence [Figs. 5.2(b)-5.2(e)] of a gate potential in one of the arms of the ring. Tight-binding and simplified Dirac results are depicted in red dashed and black solid lines, respectively. In Figs. 5.2(b) and 5.2(d) [5.2(c) and 5.2(e)], the gate potential was taken as $V = 0.1$ eV [$V = 0.2$ eV], and the gate potential length was assumed as $W \approx 30$ nm [$W \approx 15$ nm] in Figs. 5.2(b) and 5.2(c) [5.2(d) and 5.2(e)]. Fig. 5.2 shows that the results from the continuum and tight-binding models exhibit better agreement for lower energy values and lower magnetic flux values, due to the effects of the energy band curvature at high energy and the finite width of the tight-binding sample to be less relevant in low-energy range.

In Subsection 5.2.1 we determined the expression (5.14) for the effect of the potential barrier in the energy spectrum, which consists of increasing the value of the energies by $WV/(2\pi R)$. For the assumed values of $L_1 \approx 50$ nm, $L_2 \approx 33$ nm, the average radius is $R \approx 38$ nm, and then the Fermi energy increment in Fig. 5.2(b) [5.2(c)] for $W \approx 30$ nm and $V = 0.1$ eV [$V = 0.2$ eV] is 0.0125 eV [0.0251 eV], and in Fig. 5.2(d) [5.2(e)] for $W \approx 15$ nm and $V = 0.1$ eV [$V = 0.2$ eV] is 0.0064 eV [0.0128 eV]. This effect is particularly important because the persistent current of the lower-energy states can be modulated by adjusting the potential barrier height, as it will become clearer with the discussions of Figs. 5.4 and 5.5. This is due to the Fermi energy shift and, consequently, the breaking of the electron-hole symmetry with respect to $E = 0$. It is also evident to note that, for a given energy value, states are available only for specific values of magnetic flux (almost equally spaced). This is reminiscent of the energy spectrum of the electrons, described by Schrödinger equation, confined in semiconductor quantum rings in the presence of perpendicular magnetic fields, where the energies oscillate periodically with the magnetic flux due to the Aharonov-Bohm effect[131, 161]. For a finite potential, we can also see the presence of localized states, due to confinement inside the barrier region. Those states are beyond the simplified continuum model [Eq. (5.7)] and will be discussed in detail later.

Similar to the Aharonov-Bohm effect in semiconductor quantum rings, oscil-

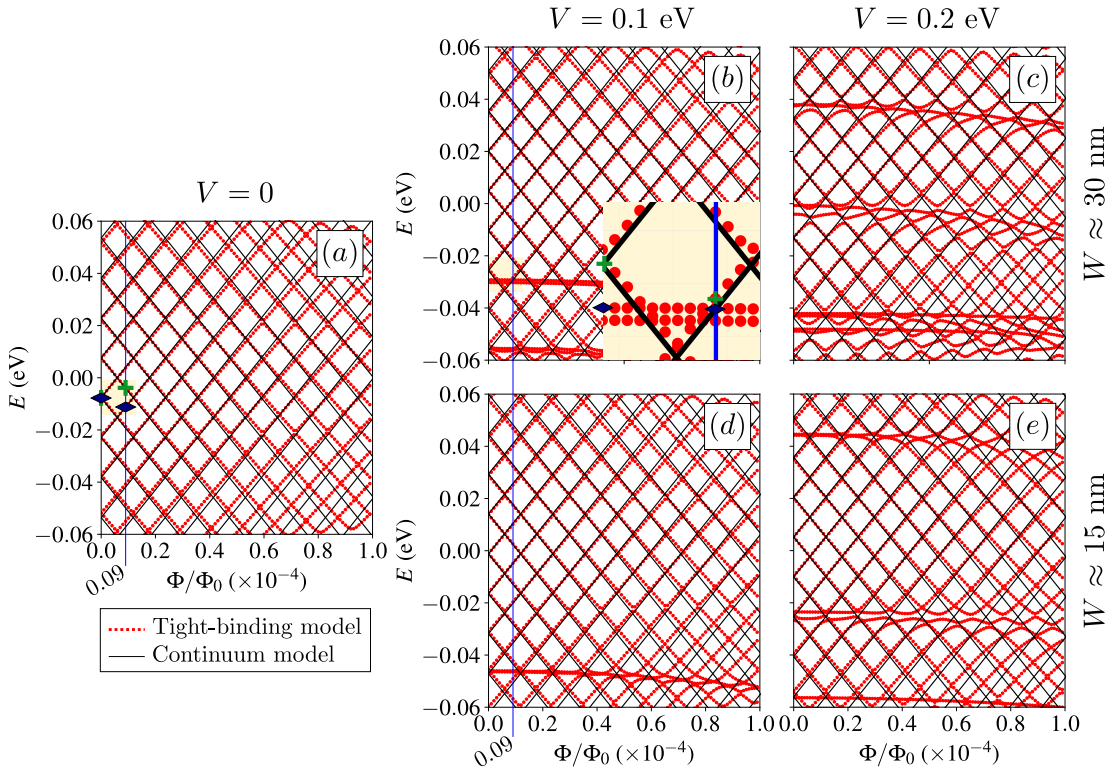

Figure 5.2: Energy levels of the hexagonal rings investigated in this Chapter, obtained from tight-binding (red dashed lines) and simplified continuum (black solid lines) models, as a function of the magnetic flux through a hexagon of carbon atoms in the absence [panel (a)] and in the presence [panels (b)-(e)] of electrical bias applied in one of the arms of the ring, as sketched in Fig. 5.1. The gate potential was taken in panels (b) and (d) as $V = 0.1$ eV and in panels (c) and (e) as $V = 0.2$ eV. Panels (b) and (c) [(d) and (e)] correspond to gate potential length $W \approx 30$ nm [$W \approx 15$ nm]. An enlargement of the yellow region in panel (b) is shown to emphasize the behavior almost non-dispersive of the states around $E \approx -0.03$ eV.

lations of energy eigenvalues can also be associated with transitions between states with persistent currents in clockwise and counterclockwise directions, as seen in the probability current densities of Fig. 5.3. At $\Phi/\Phi_0 = 0$, the persistent current of the lower energy state represented in Fig. 5.2(a) by the blue rhombus symbol has increasing energy trend with the increase of the magnetic flux and is clockwise, as shown in Fig. 5.3(d). Likewise, the persistent current of the state represented in Fig. 5.2(a) by the green cross symbol, also at $\Phi/\Phi_0 = 0$, has decreasing energy trend with the increase of the magnetic flux and, as shown in Fig. 5.3(a), is counterclockwise. In addition, even for non-null magnetic flux and in the absence of a potential barrier the persistent currents for the lower energy states exhibit the same enclosing current density profile, as shown for $\Phi/\Phi_0 = 0$ and $\Phi/\Phi_0 = 0.09\times10^{-4}$ and discussed in Ref. [131]. This is due to the derivative of the energy

in relation to the magnetic flux, and therefore the persistent current, for the same states, is the same for the magnetic flux values considered. At high energies and high magnetic flux ranges, anti-crossings are observed in the energy spectrum and, consequently, the current flow pattern for these states are altered, seeming to mix different enclosing currents[133].

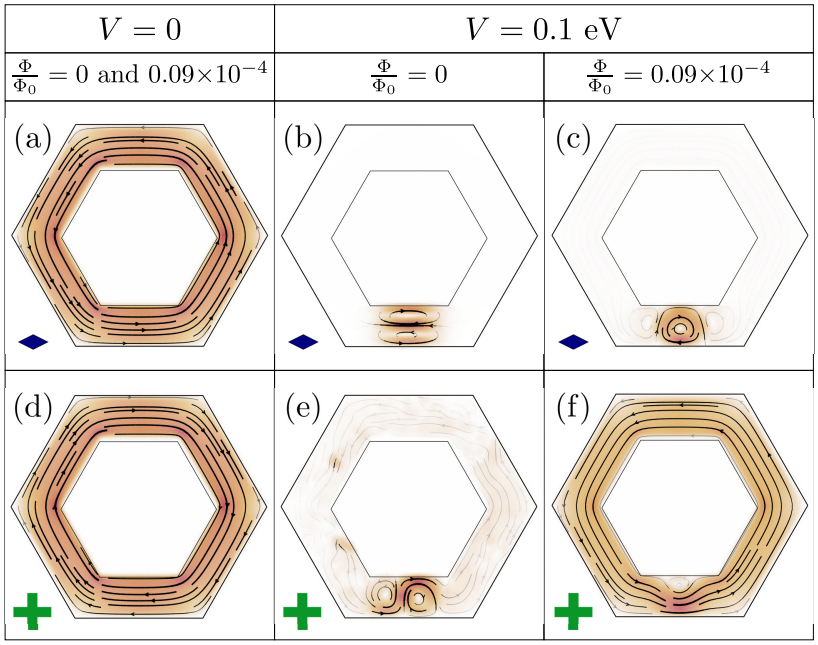

Figure 5.3: Probability current densities of the system shown in Fig. 5.1 for (a, d) null electrical bias ($V = 0$), and (b, c, e, f) under the effect of a gate potential $V = 0.1$ eV, taking (b, e) $\Phi/\Phi_0 = 0$ and (c, f) $\Phi/\Phi_0 = 0.09\times10^{-4}$. Top panels (a, b, c) [bottom panels (d, e, f)] correspond to the states labeled by a rhombus-like symbol [cross-like symbol] in Figs. 5.2(a) and 5.2(b).

An interesting feature present in the tight-binding results and not captured by the simplified continuum model is the appearance of quasi-localized states within the potential barrier region. Such states have been studied for both graphene[19, 162] and its nanoribbons with armchair-like edges[163]. In these nanostructures, the localized states depend on barrier parameters, such as its height, length, and width. Since we keep the potential barrier width constant, that in turn is the same ring width, the number of quasi-localized states for a fixed energy range depends directly on the potential height and length, as shown in Fig. 5.2 and discussed next for Fig. 5.4. As observed in Figs. 5.2(b)-5.2(e), such quasi-localized states are weakly magnetic field dependent. Fixing the potential barrier length at $W \approx 30$ nm [$W \approx 15$ nm], more quasi-localized states appear for a fixed energy range as the potential barrier height increases, as shown in Figs. 5.2(b) and 5.2(c) for $V = 0.1$ eV and $V = 0.2$ eV [Figs. 5.2(d) and 5.2(e)], respectively. Likewise, fixing the potential barrier height at $V = 0.1$ eV [$V = 0.2$ eV] and increasing the potential

barrier length from $W \approx 15$ nm to $W \approx 30$ nm, more quasi-localized states also occur, as verified by comparing Fig. 5.2(b) with Fig. 5.2(d) [Fig. 5.2(c) with Fig. 5.2(e)]. These quasi-non-dispersive states imply a vanishing of the persistent current.

To investigate this in more detail, we enlarged the yellow shaded region of the states around $E \approx -0.03$ eV (at low magnetic fluxes) in Fig. 5.2(b). We can notice that two successive states [the same ones considered in Fig. 5.2(a)] have completely different behavior. The one with the highest energy, at $\Phi/\Phi_0 = 0$ or $\Phi/\Phi_0 = 0.09\times10^{-4}$, represented by green cross-like symbols, is dispersive, as shown in Figs. 5.3(e) and 5.3(f). On the other hand, the one with the lowest energy, also at $\Phi/\Phi_0 = 0$ or $\Phi/\Phi_0 = 0.09\times10^{-4}$, represented by blue rhombus-like symbols, has a quasi-localized character, implying a vanishing of the persistent current, as shown in Figs. 5.3(b) and 5.3(c). As discussed in Ref. [163], these localized states are a consequence of the mixing of $\mathbf{K}$ and $\mathbf{K}'$ states due to the armchair edges, reason why it is not captured in the continuum model of a single $\mathbf{K}$ Dirac valley as presented here. Therefore, such non-dispersive states are linked to the finite width of the hexagonal ring composed by armchair nanoribbons.

Next, we investigate the dependence of energy levels on the potential barrier height V for $B = 0$ [Figs. 5.4(a) and 5.4(c)] and $B \neq 0$ [Figs. 5.4(b) and 5.4(d)]. In Figs. 5.4(a) and 5.4(b) [5.4(c) and 5.4(d)], the potential barrier length was taken as $W \approx 30$ nm [$W \approx 15$ nm].

Similarly to Fig. 5.2, the results obtained in Fig. 5.4 show that the simplified continuum model (solid black lines) satisfactorily describes the tight-binding results (dashed red lines). From Eq. (5.14) and for $R \approx 38$ nm, one obtains an energy level spacing of $\Delta E = 0.0152$ eV that is independent of the magnetic flux and the potential barrier length, as seen in Fig. 5.4. Additionally, the partial derivative of E with respect to V gives us the energy slope of $0.0042W$. For Figs. 5.4(a) and 5.4(b) [Figs. 5.4(c) and 5.4(d)] its value is ≈ 0.1246 [≈ 0.0638]. Note that the quasi-localized states manifest in the energy versus V plot as additional states with a greater slope than the dispersive states. Another uncaptured feature by the simplified Dirac model is the existence of a mix of crossing and anti-crossing states, as depicted in Figs. 5.2 and 5.4. As can be seen by comparing Figs. 5.4(a) and 5.4(c) with Figs. 5.4(b) and 5.4(d), respectively, and also discussed before, that the quasi-localized states are practically unaffected by the magnetic flux, and the number of the quasi-non-dispersive states depends only on the

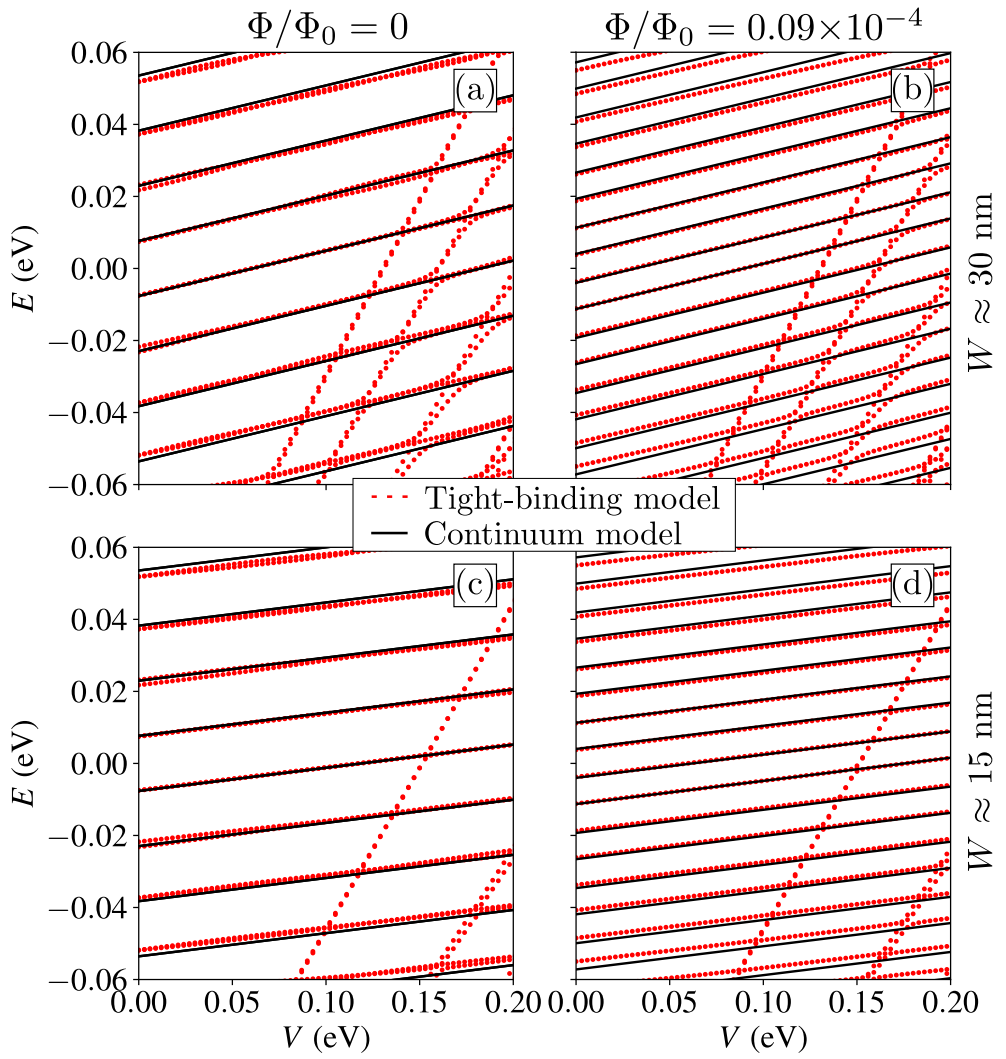

Figure 5.4: Energy levels of the hexagonal rings, obtained from tight-binding (red dashed lines) and simplified continuum (black solid lines) models, as a function of the electrical bias applied in one of the arms of the ring in the absence [$\Phi/\Phi_0 = 0$, panels (a) and (c)] and in the presence [$\Phi/\Phi_0 = 0.09\times10^{-4}$, panels (b) and (d)] of an external magnetic field. Panels (a) and (b) [(c) and (d)] correspond to gate potential length $W \approx 30$ nm [$W \approx 15$ nm].

potential barrier length.

Lastly, we analyze the dependence of the energy levels on the potential barrier length W in the absence [$\Phi/\Phi_0 = 0$, Fig. 5.5(a)] and in the presence [$\Phi/\Phi_0 = 0.09\times10^{-4}$, Fig. 5.5(b)] of a uniform perpendicularly applied magnetic field. As predicted by Eq. (5.14) and easily realized by Fig. 5.5, the dispersive energy levels have a linear dependence on W, *i.e.* $E \propto W$, with slope $\approx 0.0042V$. For the assumed value of the gate potential height as $V = 0.15$ eV, one gets $E \approx 6.3\times10^{-4}W$. From Fig. 5.5 it is explicit noticed that the non-dispersive states within the potential barrier arise as the potential barrier length W increases. In accordance with what was previously discussed, these quasi-localized

states seem qualitatively to be only weakly affected by the magnetic flux, as verified by comparison between Fig. 5.5(a) and Fig. 5.5(b).

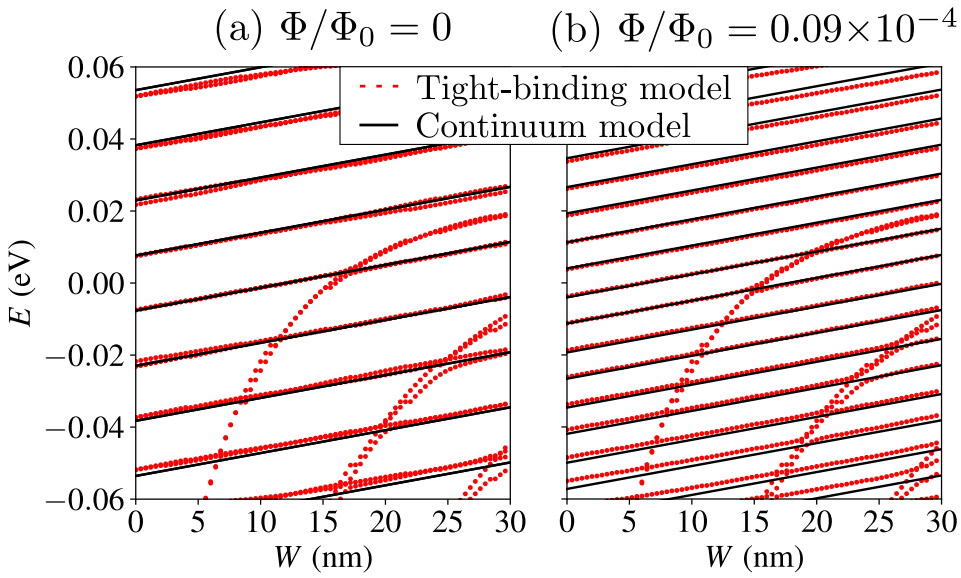

Figure 5.5: Energy levels of the hexagonal rings, obtained from tight-binding (red dashed lines) and simplified continuum (black solid lines) models, as a function of the length of the gate potential applied in one of the arms of the ring in (a) the absence ($\Phi/\Phi_0 = 0$) and in (b) the presence ($\Phi/\Phi_0 = 0.09\times10^{-4}$) of a uniform magnetic field. The gate potential height was taken as $V = 0.15$ eV.

Therefore, the persistent current modulation can be achieved by adjusting V at fixed Φ/Φ_0 and W, or by adjusting Φ/Φ_0 at fixed V and W.

5.4 Conclusion

We have presented results for the electronic spectrum of graphene-based quantum rings in the presence of a localized potential in one of the ring arms. We employed the tight-binding model to take into account the microscopic aspect of the structure, and showed that these results can display qualitative as well as quantitative agreement with a simplified one-dimensional Dirac model that includes the effect of the localized potential as a phase shift of the electronic states of the otherwise unperturbed ring. The tight-binding spectra also show the presence of quasi-localized states in the perturbed region that are weakly dependent on the magnetic field. The gapless nature of the electronic spectrum in graphene allows for an overlap between these quasi-localized and the extended ring states, which can be tuned by varying the barrier height or by the magnetic field.

6 FINAL CONSIDERATIONS

Due to the lack of scientific papers presenting in a didactic way the tight-binding model in first and second quantization formalisms and theirs equivalence to calculate the electronic properties of one and two-dimensional (2D) lattice crystals, in Chapter 2 we reviewed the basic concepts of the aforementioned framework in the solid state physics for a generic Hamiltonian and then we applied both methodologies to some examples: a linear chain and a square lattice with one and two sites per unit cell, brick lattice, graphene (honeycomb) lattice, and τ_3-lattice. With that, we present the obtaining development of the dispersion relation for lattices with different number of sites in the unit cell: one, two, and three, and consequently, energy spectra with different number of bands: one, two, and three, respectively. In addition, we discussed the role of the overlap parameter on the electronic spectrum and density of states, showing that a nonzero overlap parameter leads to an electron-hole symmetry breaking and, consequently, to an energetic unbalance in the DOS with respect to the Fermi energy. Since the tight-binding method is a well-known atomistic technique with enormous computational advantageous due to its simplicity and large scalability with reasonable computational cost in comparison to first-principle methods, it has been widely used in the semiconductor scientific community, especially nowadays for researchers and students that are investigating the 2D nano-world composed by hundreds of 2D materials, such as graphene and the broad family of the transition metal dichalcogenides. Moreover, this method allows to include additional effects, such as electron-electron interaction, defects, impurities, and deformations. Motivated by these facts, we believe that Chapter 2 will prove useful for those who seek a didactic explanation of the method with the discussion of relevant examples of 2D crystals that are currently being investigated for the development of future 2D material-based technologies.

The fact that charge carriers propagating through a graphene p-n junction at a specific energy exhibit a lensing effect which focus the transmitted electron beams, due to

the negative refraction index created by the p-n junction, suggests that the Dirac electron behavior in a graphene p-n junction is analog of light beams in a Veselago lens. Based on that it may be possible to exploit this lensing effect in quantum optic-like systems. In Chapter 3, we propose a graphene-based current modulator-like system. We show that an in-plane electric field or an out-of-plane magnetic field changes the electronic focal spot away from the output lead and consequently tune the current transmission between the input and output leads. By using the Landauer-Büttiker formalism within the tight-binding approach, we present the proof-of-concept that such proposed device model allows the modulation of the current by the proper application of a weak in-plane electric field or a perpendicular magnetic field, investigating the external field effects on the probability current density and conductance of the system for different system parameters, such as the Fermi energy, the system size, and the potential step height. Motivated by the fact that graphene p-n junctions are one of the most basic building blocks of the variety proposed device models in the recent literature, being therefore relevant to the development of future graphene-based technology, and, in addition to that, once Chapter 3 brings up a simple way to manipulate the transport properties of graphene p-n junction, showing significant results by applying electric and/or magnetic fields, with no need to induce a band gap in the sample, we believe that the graphene-based nanostructured device model proposed in Chapter 3 contributes to a basic understanding of the transport physics in graphene p-n junctions.

Charge carriers propagating through a graphene p-n junction display behavior analogous to light rays across an optical boundary. Such optic-like propagation of 2D Dirac fermions is due to the interplay between the effective negative refraction of p-n junctions in graphene together with the angle dependence of the Klein tunneling. Based on that analogy, different theoretical and experimental proposals for manipulating electron beams in graphene have emerged, such as beams splitters, wave guides, collimators, reflectors, rectifiers, modulators and switches. In Chapter 4, we propose a three-terminal Y-shaped graphene-based switch. The operating principle of the system consists of current controlling by tuning the refractive index established by a gate potential applied in one of the output branches. By means of the Landauer-Büttiker formalism within the tight-binding approach, we initially show the proof-of-concept that the system act as a gate potential-controlled current switch. Next we present transport results to analyze

the conductance as a function of the system parameters (Fermi energy, system size, and the potential height and length) and thus to characterize the best setup configuration to achieve a maximum efficiency. Motivated by the fact that graphene p-n junctions are one of the most basic building blocks of the device models in the literature, being therefore relevant to the development of future graphene-based technology, and, in addition Chapter 4 brings up a simple way to control the current in a three-terminal graphene device, we expect that our findings will prove useful for the designing of graphene-based current switches despite in the absence of a gap in the graphene band structure.

The comparatively large phase coherence length of electrons in graphene is expected to allow the observation of persistent currents at larger scales than in normal metals. One important point that must be taken into account in the analysis of these structures is the effect of impurities. In the case of graphene, the presence of impurities can lead to unexpected results due to the massless Dirac fermion character of its charge carriers. In addition to the aforementioned property, it is known that charge carriers traveling through a potential barrier in graphene undergo a phase shift that is energy-independent, being simply a function of the geometry of the potential, due to the linearity of its dispersion relation. For the square potential case created by a gate voltage, for instance, the phase shift is a function of the product of the potential height and the length of the barrier. Based on these features, in Chapter 5, we investigate the effect of gate-induced phase shift on the persistent current in a graphene quantum ring and how that, in turn, depends on the parameters of the potential barrier. Our analysis is analytically developed for a simplified model describing an infinitely thin circular Dirac ring, in which it is assumed that the ring width approaches zero so that there will be no explicit radial dependence in our model and the persistent current will flow only in the angular direction. By including the additional phase, raising from potential barrier interaction with the charge carriers, into the obtained energy spectrum we show the existence of localized states in the non-null potential regions and that the persistent current can be modulated by controlling the gate voltage. Moreover, our simplified continuum results are compared with the tight-binding ones exhibiting a good agreement and capturing the main physics of the gate-current-control in the graphene quantum ring. Motivated by the fact that graphene has been shown to be a relevant 2D material and widely promising candidate to the development of future technological applications, and, in addition, Chapter 5 brings

up a simple way to control the persistent current in graphene-based quantum ring device, we expect that our findings will prove useful for the designing of graphene-based current interferometer.

The theoretical proposals of graphene-based electronic devices presented in this Thesis can be extended to anisotropic two-dimensional materials such as phosphorene. In a phosphorene p-n junction, electrons behave in the armchair direction as massive Dirac fermions and in the zigzag direction as Schrödinger electrons[164, 165]. Due to the anisotropy in the phosphorene band structure, electron optics strongly depends on the orientation of the p-n junction in relation to the sublattice. Negative and anomalous reflection are observed for tilted junctions, and omni-directional total reflection, called anti-super-Klein tunneling, is verified if the p-n junction is parallel to the armchair edge[166]. Therefore, as a perspective to proceed with the ideas of this Thesis, we intend to investigate the electronic transport in phosphorene-based nanostructures with different number of layers subjected to external fields.

REFERENCES

[1] A. H. Castro Neto et al. The electronic properties of graphene. *Reviews of Modern Physics*, 81:109, 2009.

[2] V. V. Cheianov, V. Fal'ko, and B. L. Altshuler. The focusing of electron flow and a Veselago lens in graphene p-n junctions. *Science*, 315:1252–1255, 2007.

[3] R. Kundu. Tight-binding parameters for graphene. *Modern Physics Letters B*, 25:163–173, 2011.

[4] G. Moore. Nanotecnologia em ambalagens. *Editora Blucher*, 2009.

[5] I. S. Oliveira and C. L. Vieira. Física hoje, uma aventura pela natureza: dos átomos ao universo. *Instituto Ciência Hoje - Centro Brasileiro de Pesquisas Físicas*, 2007.

[6] Editorials. Gate insulators at the limit. *Nature Electronics*, 4:91, 2021.

[7] A. K. Geim and K. S. Novoselov. The rise of graphene. *Nature Materials*, 6:183–191, 2007.

[8] K. S. Novoselov et al. Electric field effect in atomically thin carbon films. *Science*, 306:666–669, 2004.

[9] K. S. Novoselov. Nobel lecture: graphene: materials in the flatland. *Reviews of Modern Physics*, 83:837, 2011.

[10] R. C. Sinclair, J. L. Suter, and P. V. Coveney. Micromechanical exfoliation of graphene on the atomistic scale. *Physical Chemistry Chemical Physics*, 21:5716–5722, 2019.

[11] M. I. Katsnelson. Graphene: carbon in two dimensions. *Materials Today*, 10:20–27, 2007.

[12] X. Chen, L. Zhang, and S. Chen. Large area CVD growth of graphene. *Synthetic Metals*, 210:95–108, 2015.

[13] H. W. Kroto et al. C_{60}: buckminsterfullerene. *Nature*, 318:162–163, 1985.

[14] S. Iijima. Helical microtubules of graphitic carbon. *Nature*, 354:56–58, 1991.

[15] S. Zhang et al. Penta-graphene: a new carbon allotrope. *Proceedings of the National Academy of Sciences of the United States of America*, 112:2372–2377, 2015.

[16] H. Lu and S.-D. Li. Two-dimensional carbon allotropes from graphene to graphyne. *Journal of Materials Chemistry C*, 1:3677–3680, 2013.

[17] M. Barbier et al. Dirac and Klein-Gordon particles in one-dimensional periodic potentials. *Physical Review B*, 77:115446, 2008.

[18] O. Klein. Die reflexion von elektronen an einem potentialsprung nach der relativistischen dynamik von Dirac. *Zeitschrift für Physik*, 53:157–165, 1929.

[19] M. I. Katsnelson, K. S. Novoselov, and A. K. Geim. Chiral tunnelling and the Klein paradox in graphene. *Nature Physics*, 2:620–625, 2006.

[20] J. M. PereiraJunior et al. Klein tunneling in single and multiple barriers in graphene. *Semiconductor Science and Technology*, 25:033002, 2010.

[21] N. Stander, B. Huard, and D. Goldhaber-Gordon. Evidence for Klein tunneling in graphene p-n junctions. *Physical Review Letters*, 102:026807, 2009.

[22] D. J. P. de Sousa et al. Interferometry of Klein tunnelling electrons in graphene quantum rings. *Journal of Applied Physics*, 121:024302, 2017.

[23] J. B. Pendry. Negative refraction makes a perfect lens. *Physical Review Letters*, 85:3966, 2000.

[24] V. G. Veselago. The electrodynamics of substances with simultaneously negative values of ϵ and μ. *Soviet Physics Uspekhi*, 10:509, 1968.

[25] J. B. Pendry. Negative refraction for electrons? *Science*, 315:1226–1227, 2007.

[26] M. Y. Han et al. Energy band-gap engineering of graphene nanoribbons. *Physical Review Letters*, 98:206805, 2007.

[27] X. Li et al. Chemically derived, ultrasmooth graphene nanoribbon semiconductors. *Science*, 319:1229–1232, 2008.

[28] D. V. Kosynkin et al. Longitudinal unzipping of carbon nanotubes to form graphene nanoribbons. *Nature*, 458:872–876, 2009.

[29] X. Yang et al. Two-dimensional graphene nanoribbons. *Journal of the American Chemical Society*, 130:4216–4217, 2008.

[30] K. Wakabayashi et al. Electronic states of graphene nanoribbons and analytical solutions. *Science and Technology of Advanced Materials*, 11:054504, 2010.

[31] C. W. Groth et al. Kwant: a software package for quantum transport. *New Journal of Physics*, 16:063065, 2014.

[32] J. Baringhaus et al. Exceptional ballistic transport in epitaxial graphene nanoribbons. *Nature*, 506:349–354, 2014.

[33] P. Hohenberg and W. Kohn. Inhomogeneous electron gas. *Physical Review*, 136:B864, 1964.

[34] F. Bloch. über die quantenmechanik der elektronen in kristallgittern. *Zeitschrift für Physik*, 52:555–600, 1929.

[35] J. C. Slater and G. F. Koster. Simplified LCAO method for the periodic potential problem. *Physical Review*, 94:1498, 1954.

[36] A. N. Rudenko, S. Yuan, and M. I. Katsnelson. Toward a realistic description of multilayer black phosphorus: from GW approximation to large-scale tight-binding simulations. *Physical Review B*, 92:085419, 2015.

[37] S. Reich et al. Tight-binding description of graphene. *Physical Review B*, 66:035412, 2002.

[38] A. V. Gert, M. O. Nestoklon, and I. N. Yassievich. Band structure of silicene in the tight binding approximation. *Journal of Experimental and Theoretical Physics*, 121:115–121, 2015.

[39] R. M. Ribeiro and N. M. R. Peres. Stability of boron nitride bilayers: ground-state energies, interlayer distances, and tight-binding description. *Physical Review B*, 83:235312, 2011.

[40] K. Tagami et al. Electronic transport properties of free-base tape-porphyrin molecular wires studied by self-consistent tight-binding calculations. *Physical Review B*, 67:245324, 2003.

[41] Y. Liu and P. M. Hui. Electronic-transport properties of tight-binding multiring systems. *Physical Review B*, 57:12994, 1998.

[42] J. A. Fürst et al. Electronic transport properties of fullerene functionalized carbon nanotubes: ab initio and tight-binding calculations. *Physical Review B*, 80:035427, 2009.

[43] F. R. V. Araújo et al. Current modulation in graphene p-n junctions with external fields. *Journal of Physics: Condensed Matter*, 32:425501, 2020.

[44] F. R. V. Araújo et al. Gate potential-controlled current switching in graphene Y-junctions. *Journal of Physics: Condensed Matter*, 33:375501, 2021.

[45] K.-H. Ding et al. Quantum Hall effect in ac driven graphene: from the half-integer to the integer case. *Physical Review B*, 97:035123, 2018.

[46] N. W. Ashcroft and N. D. Mermin. Solid state physics. *Cengage Learnign, Inc*, 1976.

[47] R. Saito, G. Dresselhaus, and M. S. Dresselhaus. Physical properties of carbon nanotubes. *Imperial College Press*, 1998.

[48] P. Markos and C. M. Soukoulis. Wave propagation: from electrons to photonic crystals and left-handed materials. *Princeton University Press*, 2008.

[49] M. P. Marder. Condensed matter physics. *John Wiley & Sons*, 2010.

[50] K. F. Garrity and K. Choudhary. Database of Wannier tight-binding Hamiltonians using high-throughput density functional theory. *Scientific Data*, 8:1–10, 2021.

[51] A. L. Fetter and J. D. Walecka. Quantum theory of many-particle systems. *Dover Publications, Inc*, 2003.

[52] I. S. Oliveira and V. L. B. de Jesus. Introdução à física do estado sólido. *Editora Livraria da Física*, 2005.

[53] C. Kittel and P. McEuen. Introduction to solid state physics. *John Wiley & Sons*, 2005.

[54] D. R. da Costa et al. Energy levels of bilayer graphene quantum dots. *Physical Review B*, 92:115437, 2015.

[55] B. A. McKinnon and T. C. Choy. Significance of nonorthogonality in tight-binding models. *Physical Review B*, 52:14531, 1995.

[56] K. Wakabayashi et al. Electronic and magnetic properties of nanographite ribbons. *Physical Review B*, 59:8271, 1999.

[57] G. Montambaux. Artificial graphenes: Dirac matter beyond condensed matter. *Comptes Rendus Physique*, 19:285–305, 2018.

[58] J.-M. Hou and W. Chen. Hidden symmetry and protection of Dirac points on the honeycomb lattice. *Scientific Reports*, 5:1–11, 2015.

[59] D. A. Abanin et al. Interferometric approach to measuring band topology in 2D optical lattices. *Physical Review Letters*, 110:165304, 2013.

[60] E. T. Sisakht, M. H. Zare, and F. Fazileh. Scaling laws of band gaps of phosphorene nanoribbons: a tight-binding calculation. *Physical Review B*, 91:085409, 2015.

[61] K. S. Novoselov et al. Two-dimensional gas of massless Dirac fermions in graphene. *Nature*, 438:197–200, 2005.

[62] F. Piéchon et al. Tunable orbital susceptibility in $\alpha - t_3$ tight-binding models. *Journal of Physics: Conference Series*, 603:012001, 2015.

[63] Q. Wilmart et al. A Klein-tunneling transistor with ballistic graphene. *2D Materials*, 1:011006, 2014.

[64] J. M. Pereira Junior, P. Vasilopoulos, and F. M. Peeters. Graphene-based resonant-tunneling structures. *Applied Physics Letters*, 90:132122, 2007.

[65] M. R. Masir, P. Vasilopoulos, and F. M. Peeters. Fabry-Pérot resonances in graphene microstructures: Influence of a magnetic field. *Physical Review B*, 82:115417, 2010.

[66] A. V. Shytov, M. S. Rudner, and L. S. Levitov. Klein backscattering and Fabry-Pérot interference in graphene heterojunctions. *Physical Review Letters*, 101:156804, 2008.

[67] L. Brey and H. A. Fertig. Electronic states of graphene nanoribbons studied with the Dirac equation. *Physical Review B*, 73:235411, 2006.

[68] K. Wakabayashi et al. Electronic transport properties of graphene nanoribbons. *New Journal of Physics*, 11:095016, 2009.

[69] A. V. Rozhkov et al. Electronic properties of mesoscopic graphene structures: Charge confinement and control of spin and charge transport. *Physics Reports*, 503:77–114, 2011.

[70] C. Stampfer et al. Transport in graphene nanostructures. *Frontiers of Physics*, 6:271–293, 2011.

[71] A. C. S. Nascimento et al. Electronic transport on graphene armchair-edge nanoribbons with Fermi velocity and potential barriers. *Physics Letters A*, 383:2416–2423, 2019.

[72] Y.-W. Son, M. L. Cohen, and S. G. Louie. Energy gaps in graphene nanoribbons. *Physical Review Letters*, 97:216803, 2006.

[73] H. Shu et al. Significantly high modulation efficiency of compact graphene modulator based on silicon waveguide. *Scientific Reports*, 8:1–8, 2018.

[74] S. P. Milovanović, D. Moldovan, and F. M. Peeters. Veselago lensing in graphene with a p-n junction: Classical versus quantum effects. *Journal of Applied Physics*, 118:154308, 2015.

[75] V. T. Phong and J. F. Kong. Fermionic lensing in smooth graphene p-n junctions. 2016.

[76] W. J. Padilla, D. N. Basov, and D. R. Smith. Negative refractive index metamaterials. *Materials Today*, 9:28–35, 2006.

[77] V. V. Cheianov and V. I. Fal'ko. Selective transmission of Dirac electrons and ballistic magnetoresistance of n-p junctions in graphene. *Physical Review B*, 74:041403, 2006.

[78] D. A. Abanin and L. S. Levitov. Quantized transport in graphene p-n junctions in a magnetic field. *Science*, 317:641–643, 2007.

[79] A. Shytov et al. Atomic collapse, Lorentz boosts, Klein scattering, and other quantum-relativistic phenomena in graphene. *Solid State Communications*, 149:1087–1093, 2009.

[80] T. Low. Ballistic-ohmic quantum Hall plateau transition in a graphene p-n junction. *Physical Review B*, 80:205423, 2009.

[81] T. Low and J. Appenzeller. Electronic transport properties of a tilted graphene p-n junction. *Physical Review B*, 80:155406, 2009.

[82] S. P. Milovanović, M. R. Masir, and F. M. Peeters. Graphene Hall bar with an asymmetric pn-junction. *Journal of Applied Physics*, 113:193701, 2013.

[83] S. P. Milovanović, M. R. Masir, and F. M. Peeters. Magnetic electron focusing and tuning of the electron current with a pn-junction. *Journal of Applied Physics*, 115:043719, 2014.

[84] K. J. A. Reijnders and M. I. Katsnelson. Symmetry breaking and (pseudo)spin polarization in Veselago lenses for massless Dirac fermions. *Physical Review B*, 95:115310, 2017.

[85] G.-H. Lee, G.-H. Park, and H.-J. Lee. Observation of negative refraction of Dirac fermions in graphene. *Nature Physics*, 11:925–929, 2015.

[86] B. Huard et al. Transport measurements across a tunable potential barrier in graphene. *Physical Review Letters*, 98:236803, 2007.

[87] L. Lin et al. Building graphene p-n junctions for next-generation photodetection. *Nano Today*, 10:701–716, 2015.

[88] S. Chen et al. Electron optics with p-n junctions in ballistic graphene. *Science*, 353:1522–1525, 2016.

[89] G. S. Settles. High-speed imaging of shock waves, explosions and gunshots: New digital video technology, combined with some classic imaging techniques, reveals shock waves as never before. *American Scientist*, 94:22–31, 2006.

[90] N. M. R. Peres and E. V. Castro. Algebraic solution of a graphene layer in transverse electric and perpendicular magnetic fields. *Journal of Physics: Condensed Matter*, 19:406231, 2007.

[91] H. M. Abdullah et al. Electron collimation at van der Waals domain walls in bilayer graphene. *Physical Review B*, 100:045137, 2019.

[92] V. Ariel and A. Natan. Electron effective mass in graphene. *2013 International Conference on Electromagnetics in Advanced Applications (ICEAA)*, pages 696–698, 2013.

[93] S. Prabhakar et al. Valley-dependent Lorentz force and Aharonov-Bohm phase in strained graphene p-n junction. *Physical Review B*, 99:094111, 2019.

[94] J. D. Meindl, Q. Chen, and J. A. Davis. Limits on silicon nanoelectronics for terascale integration. *Science*, 293:2044–2049, 2001.

[95] L. M. Zhang and M. M. Fogler. Nonlinear screening and ballistic transport in a graphene p-n junction. *Physical Review Letters*, 100:116804, 2008.

[96] J. Yang, P. Hu, and G. Yu. Perspective of graphene-based electronic devices: graphene synthesis and diverse applications. *APL Materials*, 7:020901, 2019.

[97] K. Kim et al. A role for graphene in silicon-based semiconductor devices. *Nature*, 479:338–344, 2011.

[98] K. L. Shepard, M. L. Roukes, and B. P. van der Gaag. Experimental measurement of scattering coefficients in mesoscopic conductors. *Physical Review B*, 46:9648, 1992.

[99] R. de Picciotto et al. Four-terminal resistance of a ballistic quantum wire. *Nature*, 411:51–54, 2001.

[100] R. Leturcq et al. Multi-terminal transport through a quantum dot in the Coulomb-blockade regime. *EPL (Europhysics Letters)*, 67:439, 2004.

[101] P. R. Bandaru et al. Novel electrical switching behaviour and logic in carbon nanotube Y-junctions. *Nature Materials*, 4:663–666, 2005.

[102] D. Wallin and H. Q. Xu. Electrical properties and logic function of multibranch junction structures. *Applied Physics Letters*, 86:253510, 2005.

[103] J. Sun et al. Frequency mixing and phase detection functionalities of three-terminal ballistic junctions. *Nanotechnology*, 18:195205, 2007.

[104] D. G. Ravenhall, H. W. Wyld, and R. L. Schult. Quantum Hall effect at a four-terminal junction. *Physical Review Letters*, 62:1780, 1989.

[105] H. U. Baranger and A. D. Stone. Quenching of the Hall resistance in ballistic microstructures: a collimation effect. *Physical Review Letters*, 63:414, 1989.

[106] H. Q. Xu. Method of calculations for electron transport in multiterminal quantum systems based on real-space lattice models. *Physical Review B*, 66:165305, 2002.

[107] H. Q. Xu. Electrical properties of three-terminal ballistic junctions. *Applied Physics Letters*, 78:2064–2066, 2001.

[108] L. Worschech et al. Bias-voltage-induced asymmetry in nanoelectronic Y-branches. *Applied Physics Letters*, 79:3287, 2001.

[109] A. N. Jordan and M. Büttiker. Gap theory of rectification in ballistic three-terminal conductors. *Physical Review B*, 77:075334, 2008.

[110] T. Palm and L. Thylén. Analysis of an electron-wave Y-branch switch. *Applied Physics Letters*, 60:237, 1992.

[111] T. Palm and L. Thylén. Designing logic functions using an electron waveguide Y-branch switch. *Journal of Applied Physics*, 79:8076, 1996.

[112] T. Itoh. Scattering matrix of a three-terminal junction in one dimension. *Physical Review B*, 52:1508, 1995.

[113] B. C. Satishkumar et al. Y-junction carbon nanotubes. *Applied Physics Letters*, 77:2530, 2000.

[114] J. Li, C. Papadopoulos, and J. Xu. Growing Y-junction carbon nanotubes. *Nature*, 402:253–254, 1999.

[115] C. Papadopoulos et al. Electronic transport in Y-junction carbon nanotubes. *Physical Review Letters*, 85:3476, 2000.

[116] A. N. Andriotis et al. Rectification properties of carbon nanotube "Y-junctions". *Physical Review Letters*, 87:066802, 2001.

[117] A. Jacobsen et al. Rectification in three-terminal graphene junctions. *Applied Physics Letters*, 97:032110, 2010.

[118] X. Yin and S. Kasai. Graphene-based three-branch nano-junction (TBJ) logic inverter. *Physica Status Solidi (C)*, 10:1485–1488, 2013.

[119] R. Göckeritz, J. Pezoldt, and F. Schwierz. Epitaxial graphene three-terminal junctions. *Applied Physics Letters*, 99:173111, 2011.

[120] H. Q. Xu et al. Novel nanoelectronic triodes and logic devices with TBJs. *IEEE Electron Device Letters*, 25:164–166, 2004.

[121] K. Hieke and M. Ulfward. Nonlinear operation of the Y-branch switch: ballistic switching mode at room temperature. *Physical Review B*, 62:16727, 2000.

[122] K. Wang et al. Graphene transistor based on tunable Dirac fermion optics. *Proceedings of the National Academy of Sciences of the United States of America*, 116:6575–6579, 2019.

[123] S. Datta. Electronic transport in mesoscopic systems. *Cambridge University Press*, 1997.

[124] S. Thomas and K. M. Ajith. Molecular dynamics simulation of the thermomechanical properties of monolayer graphene sheet. *Procedia Materials Science*, 5:489–498, 2014.

[125] F. Gao and S. Gao. Thermodynamic stability of magnetic states of monovacancy in graphene revealed by ab initio molecular dynamics simulations. *Scientific Reports*, 9:1–5, 2019.

[126] E. N. Koukaras et al. Phonon properties of graphene derived from molecular dynamics simulations. *Scientific Reports*, 5:1–9, 2015.

[127] J. Zhou and R. Huang. Internal lattice relaxation of single-layer graphene under in-plane deformation. *Journal of the Mechanics and Physics of Solids*, 56:1609–1623, 2008.

[128] Z. F. Wang et al. Tuning the electronic structure of graphene nanoribbons through chemical edge modification: a theoretical study. *Physical Review B*, 75:113406, 2007.

[129] Y. H. Lu et al. Effects of edge passivation by hydrogen on electronic structure of armchair graphene nanoribbon and band gap engineering. *Applied Physics Letters*, 94:122111, 2009.

[130] E. A. A. e Silva. Probability current in the tight-binding model. *American Journal of Physics*, 60:753, 1992.

[131] D. R. da Costa et al. Geometry and edge effects on the energy levels of graphene quantum rings: a comparison between tight-binding and simplified Dirac models. *Physical Review B*, 89:075418, 2014.

[132] D. R. da Costa et al. Wave-packet scattering on graphene edges in the presence of a pseudomagnetic field. *Physical Review B*, 86:115434, 2012.

[133] I. R. Lavor et al. Magnetic field induced vortices in graphene quantum dots. *Journal of Physics: Condensed Matter*, 32:155501, 2020.

[134] P. E. Allain and J. N. Fuchs. Klein tunneling in graphene: optics with massless electrons. *The European Physical Journal B*, 83:301, 2011.

[135] M. Büttiker, Y. Imry, and R. Landauer. Josephson behavior in small normal one-dimensional rings. *Physics Letters A*, 96:365–367, 1983.

[136] H.-F. Cheung et al. Persistent currents in small one-dimensional metal rings. *Physical Review B*, 37:6050, 1988.

[137] S. Viefers et al. Quantum rings for beginners: energy spectra and persistent currents. *Physica E: Low-dimensional Systems and Nanostructures*, 21:1, 2004.

[138] L. P. Lévy et al. Magnetization of mesoscopic copper rings: evidence for persistent currents. *Physical Review Letters*, 64:2074, 1990.

[139] V. Chandrasekhar et al. Magnetic response of a single, isolated gold loop. *Physical Review Letters*, 67:3578, 1991.

[140] A. C. Bleszynski-Jayich et al. Persistent currents in normal metal rings. *Science*, 326:272–275, 2009.

[141] D. R. da Costa et al. Electronic properties of superlattices on quantum rings. *Journal of Physics: Condensed Matter*, 29:165501, 2017.

[142] M. Omidi and E. Faizabadi. Energy spectrum and persistent current in an armchair hexagonal graphene ring in the presence of vacancies, Rashba and Zeeman interactions. *The European Physical Journal B*, 88:1–6, 2015.

[143] M. Zarenia et al. Simplified model for the energy levels of quantum rings in single layer and bilayer graphene. *Physical Review B*, 81:045431, 2010.

[144] B.-L. Huang, M.-C. Chang, and C.-Y. Mou. Persistent currents in a graphene ring with armchair edges. *Journal of Physics: Condensed Matter*, 24:245304, 2012.

[145] D. Faria et al. Currents and pseudomagnetic fields in strained graphene rings. *Physical Review B*, 87:241403, 2013.

[146] P. Recher et al. Aharonov-Bohm effect and broken valley degeneracy in graphene rings. *Physical Review B*, 76:235404, 2007.

[147] D. S. L. Abergel, V. M. Apalkov, and T. Chakraborty. Interplay between valley polarization and electron-electron interaction in a graphene ring. *Physical Review B*, 78:193405, 2008.

[148] M. M. Ma, J. W. Ding, and N. Xu. Odd-even width effect on persistent current in zigzag hexagonal graphene rings. *Nanoscale*, 1:387–390, 2009.

[149] D. A. Bahamon, A. L. C. Pereira, and P. A. Schulz. Inner and outer edge states in graphene rings: a numerical investigation. *Physical Review B*, 79:125414, 2009.

[150] C.-H. Yan and L.-F. Wei. Size effects in Aharonov-Bohm graphene rings. *Journal of Physics: Condensed Matter*, 22:295503, 2010.

[151] H. A. Fertig and L. Brey. Nanophysics in graphene: neutrino physics in quantum rings and superlattices. *Philosophical Transactions of the Royal Society A: Mathematical, Physical and Engineering Sciences*, 368:5483–5497, 2010.

[152] L. J. P. Xavier et al. Electronic confinement in graphene quantum rings due to substrate-induced mass radial kink. *Journal of Physics: Condensed Matter*, 28:505501, 2016.

[153] N. Bolívar, E. Medina, and B. Berche. Persistent charge and spin currents in the long-wavelength regime for graphene rings. *Physical Review B*, 89:125413, 2014.

[154] A. Chaves et al. Energy shift and conduction-to-valence band transition mediated by a time-dependent potential barrier in graphene. *Physical Review B*, 92:125441, 2015.

[155] P. R. Wallace. The band theory of graphite. *Physical Review*, 71:622, 1947.

[156] G. Paz. On the connection between the radial momentum operator and the Hamiltonian in n dimensions. *European Journal of Physics*, 22:337, 2001.

[157] R. Peierls. Zur theorie des diamagnetismus von leitungselektronen. *Zeitschrift für Physik*, 80:763–791, 1933.

[158] J. M. Luttinger. The effect of a magnetic field on electrons in a periodic potential. *Physical Review*, 84:814, 1951.

[159] E. A. A. Silva. Probability current in the tight-binding model. *American Journal of Physics*, 60:753, 1992.

[160] M. Governale and C. Ungarelli. Gauge-invariant grid discretization of the Schrödinger equation. *Physical Review B*, 58:7816, 1998.

[161] G. A. Farias et al. Impurities and geometrical effects on the electron energy spectrum of quantum rings. *Physical Review B*, 77:085316, 2008.

[162] V. A. Yampol'skii, S. Savel'ev, and F. Nori. Voltage-driven quantum oscillations in graphene. *New Journal of Physics*, 10:053024, 2008.

[163] B. Trauzettel et al. Spin qubits in graphene quantum dots. *Nature Physics*, 3:192–196, 2007.

[164] V. Tran and L. Yang. Scaling laws for the band gap and optical response of phosphorene nanoribbons. *Physical Review B*, 89:245407, 2014.

[165] M. Ezawa. Topological origin of quasi-flat edge band in phosphorene. *New Journal of Physics*, 16:115004, 2014.

[166] Y. Betancur-Ocampo, F. Leyvraz, and T. Stegmann. Electron optics in phosphorene pn junctions: negative reflection and anti-super-Klein tunneling. *Nano Letters*, 19:7760–7769, 2019.